UCSF
UC San Francisco Electronic Theses and Dissertations

Title
Monitoring Response of Prostate Cancer to Ultrasound Thermal Therapy by Multi-Agent Hyperpolarized 13C Magnetic Resonance Imaging

Permalink
https://escholarship.org/uc/item/3jz903mz

Author
Lee, Jessie

Publication Date
2018

Peer reviewed|Thesis/dissertation

eScholarship.org Powered by the California Digital Library
University of California

Monitoring Response of Prostate Cancer to Ultrasound Thermal Therapy by Multi-Agent Hyperpolarized 13C Magnetic Resonance Imaging

by

Jessie Eileen Lee

DISSERTATION

Submitted in partial satisfaction of the requirements for the degree of

DOCTOR OF PHILOSOPHY

in

Bioengineering

in the

GRADUATE DIVISION

of the

UNIVERSITY OF CALIFORNIA, SAN FRANCISCO

[redacted]

To my grandma
Your spirit forever motivates me.

To my parents
Without you, I wouldn't have today.

To Cade Fox
For years, I searched for the reason of my existence.
When you entered my life, I found the answer.

Acknowledgements

I was certainly not alone during my pursuit of the PhD degree. I wouldn't be where I am today without the help of so many individuals!

First and foremost, I would like to express my deepest gratitude to my advisors, John Kurhanewicz and Chris Diederich. John and Chris are the most respectable advisors I could ever ask for, on both academic and personal levels. Since day one, John and Chris have provided me with all the guidance and resources I need—never at one point in my graduate school life was I left high and dry. Whenever I needed to meet with them, whether it was for experiment results or personal struggles, their doors were always open. Their patience and understanding allowed me to learn and grow at my own pace, embrace failures, and achieve quality research while maintaining my personal wellbeing.

I would also like to thank Bob Bok, who has been an inspiring mentor all these years. Performing animal experiments is emotionally difficult for me. Through him I saw that conducting murine research does not contradict with being a genuinely gentle, caring, and animal-loving person. The combination of his professionalism and kindness sets the standards for all animal researchers.

None of the experiments and data analyses could have gone smoothly without the technical support of Sukumar Subramaniam, Mark Van Criekinge, Renuka Sriram, and Romelyn Delos Santos from John's lab, Matthew Adams, Vasant Salgaonkar, Peter Jones, and Dong Liu from

Chris's lab, as well as Viola Rieke, Eugene Ozhinsky, and Sue Noworolski. I also thank Andrew Taylor and Steve Conolly for the guidance during the qualifying exam. Having the opportunity to work with and learn from some of the most brilliant people is truly a privilege.

My years in graduate school were greatly enhanced by friends who helped me de-stress and explore excitements in life. Specifically, members of the Kurhanewicz lab (Dave Korenchan, Jinny Sun, Justin Delos Santos, Hecong Qin, Jeremy Bancroft-Brown, Natalie Korn, and Shubhangi Agarwal) and the UCSF/UC Berkeley bioengineering cohorts (way too many to list!) have given me so much laughter and good times. While this dissertation marks the end of the graduate school, friendships never end! It's lucky to have a few lifelong friends, and it's even luckier to have so many!

Of all the friends, there are two that I couldn't have survived without—Matthew Adams and Dave Korenchan. We were in the same year, same cohort, trying to figure out the future together. From lab rotations to dissertation writing, they provided me an immense amount of support, both scientifically and emotionally. None of the hyperthermia experiments would have been possible without Matt's help. His rather uplifting sarcasm made failures amusing and successes rewarding. Dave's naturally comical personality made lab life so much more hilarious. If laughter is the best medicine, Dave probably has seriously overdosed me. His encouragements and timely warm hugs brightened many of my days.

As I look back at all the choices I've made along the way that paved ways to a PhD in bioengineering, I can see my grandmother's reflection in every step. Losing her to cancer is the first real pain in life that I've ever experienced. Transforming the pain into action, I went into the field of bioengineering, hoping that one day the research I do can prevent other families from going through what I have been through. My grandmother will forever be my motivation, my lighthouse in life.

While many people aided me through different parts of my life, I owe so much to the ones that have been there since the second I was born—my parents, Gary Lee and Shelley Juan, and my sister, Judy Lee. God never promised us a smooth sailing life, but He gave us each other so we could fight through the storms hand in hand. Together, we've encountered many rocky roads, but together, we've been through all of them. The unconditional love brought us the closest when time was the toughest. Even though we're on the opposite side of the planet, there is never any distance between our hearts.

There is one more person that I have to thank, but I don't even know where to start—Cade Fox, my first and only love in life. I'm so grateful that our paths crossed and our lives touched. He believes in me when I have doubts in myself, keeping me going when quitting seems like the easier route to take. He knows me better than I know myself, making me laugh from the bottom of my heart even when the time is tough. Every morning when I open my eyes, he tells me that I'm beautiful inside and out. Every night before I close my eyes, he lets me know how proud he is of me being my perfect self. Facing all the unknowns

in the future, he is my only certainty—I know I'll be spending the rest of my life with my best friend. What more could I possibly I ask for?

Chapter 4 of this dissertation is shows submitted work by Jessie E. Lee, Chris Diederich, Robert Bok, Renuka Sriram, Romelyn Delos Santos, Susan M. Noworolski, Vasant Salgaonkar, Matthew S. Adams, Daniel Vigneron, and John Kurhanewicz. Chapter 5 shows work done by Jessie E. Lee, Matthew S. Adams, Robert Bok, Eugene Ozhinsky, Viola Rieke, John Kurhanewicz, and Chris Diederich.

Abstract

Monitoring Response of Prostate Cancer to Thermal Therapy by Multi-Agent Hyperpolarized ^{13}C Magnetic Resonance Imaging

by

Jessie Eileen Lee

Prostate cancer is the most frequently diagnosed invasive cancer and the third leading cause of cancer death in men. Traditionally, patients with localized low- or intermediate-risk prostate cancer were forced to decide between the passive but psychologically burdensome active surveillance and the aggressive treatment options, such as surgery or radiation. In recent years, ultrasound thermal therapy has become an alternative for such cases since it is minimally invasive and causes fewer side effects. During the two main types of thermal therapy (thermal ablation and hyperthermia), the targeted tissue is exposed to heat, which either causes immediate cell death or alters the metabolism and perfusion of the tissue, making it more susceptible to adjuvant therapies such as radiation and chemotherapy.

This dissertation focuses on monitoring the response of prostate cancer to thermal ablation and hyperthermia using the technique of hyperpolarized ^{13}C MRI, which allows for non-invasive assessment of both tissue metabolism and perfusion with a single injection of the co-polarized ^{13}C-labeled pyruvate and urea. These biomarkers successfully delineated the ablated regions of the tissues while providing insight into the changes in metabolism and perfusion in the tissues receiving sub-lethal heat dose. To further explore the effects of

hyperthermia on prostate cancer, a compact MR-compatible ultrasound hyperthermia device was fabricated to perform hyperthermia on murine prostate tumors in a 14T preclinical MRI scanner (bore diameter = 4cm) with concurrent MR thermometry. The feasibility of monitoring the metabolic and perfusion changes in prostate cancer *in vivo* shortly after hyperthermia has been demonstrated. Ongoing murine studies will examine the significance of the treatment response. Noninvasive monitoring of the changes in metabolism and perfusion of prostate cancer upon thermal therapy is invaluable for determining the timing and dose of adjuvant therapies.

Table of Contents

Chapter 1: Introduction 1

Chapter 2: Thermal Therapy 4

2.1 Thermal Therapy and Effects on Tissues 4
2.1.1 Thermal Ablation 5
2.1.2 Hyperthermia 7
2.2 Ultrasound-based Thermal Therapy 10
2.3 Image-Guided Thermal Therapy 12
2.4 Small Animal Heating Systems 13

Chapter 3: MRI Basics 15

3.1 Fundamentals of Magnetic Resonance Imaging (MRI) 15
3.1.1 Nuclear Spins and Precession 15
3.1.2 Relaxation 16
3.1.3 MR Signal and Contrast 17
3.1.4 Chemical Shift 19
3.2 Multiparametric Imaging of Prostate Cancer 19
3.2.1 T_2-weighted Imaging 20
3.2.2 Diffusion-weighted Imaging (DWI) 21
3.2.3 Dynamic Contrast-Enhanced Imaging (DCE) 22
3.2.4 Proton MR Spectroscopic Imaging (^{1}H MRSI) 26
3.3 Hyperpolarized ^{13}C MRI 28
3.3.1 Dynamic Nuclear Polarization 28
3.3.2 ^{13}C-labeled Metabolites 30
3.3.3 ^{13}C MRI 3D GRASE Sequence 31
3.4 MR Thermometry 33
3.4.1 Temperature-Sensitive MR Parameters 34
3.4.2 Proton Resonance Frequency (PRF) MR Thermometry 35

Chapter 4: Assessing High-Intensity Focused Ultrasound Treatment of Prostate Cancer with Hyperpolarized ^{13}C Dual-Agent Imaging of Metabolism and Perfusion 38

4.1 Introduction 38
4.2 Material and Methods 42
4.2.1 Murine Tumor Model 42
4.2.2 Small Animal FUS Device—Fabrication and Characterization 43
4.2.3 FUS Tumor Ablation 44

4.2.4 MR Imaging 47
4.2.5 Histopathology 48
4.2.6 Data Analysis 49
4.3 Results 50
4.3.1 Small Animal FUS—Acoustic Characterization 50
4.3.2 Pathologic and Imaging Effects of HIFU 52
4.4 Discussion 59
4.5 Summary 64

Chapter 5: Compact Ultrasound Applicator for Hyperthermia Treatment of the Transgenic Adenocarcinoma Mouse Prostate Model (TRAMP) with MR Thermometry in a 14T MRI Scanner 65

5.1 Introduction 65
5.2 Material and Methods 68
5.2.1 Ultrasound Hyperthermia Device Fabrication and Characterization 68
5.2.2 MR Imaging and Thermometry 70
5.2.3 MR Temperature Verification in Phantom 72
5.2.4 Murine Tumor Model 73
5.2.6 Initial Hyperthermia Treatment Study with Hyperpolarized ^{13}C MRI Monitoring 77
5.2.7 Data Analysis 78
5.3 Results 79
5.3.1 Ultrasound Hyperthermia Applicator 79
5.3.2 MR Temperature Verification in Phantom 80
5.3.3 Murine Hyperthermia Studies 81
5.3.4 Results: Hyperpolarized ^{13}C MR Monitoring of Hyperthermia Treatment 86
5.4 Discussion 88
5.5 Summary 91

Reference 92

List of Tables

Table 3.1 Gyromagnetic ratio of common isotopes used in MRI……..……15

Table 3.2 T_2 and relative spin density of some normal tissue types……..……18

Table 4.1 Summary of the tumor volumes, baseline tumor lactate-to-pyruvate ratio, treatment parameters, and ablated volumes in the five mice studied……41

Table 4.2 The histology readings of H&E, Ki-67, and PIM of the partially treated zones of all five mice after the 5-day imaging time point……..……56

Table 5.1 Summary of the tumor volumes, mouse basal temperatures before treatments, and treatment parameters of the six mice treated with hyperthermia……..77

List of Figures

Figure 2.1 H&E staining of canine prostate 45 minutes after thermal treatment……..7

Figure 3.1 Approximate T_1values as a function of B_0……..18

Figure 3.2 Multiparametric ^{1}H MRI exam for a prostate cancer patient……20

Figure 3.3 Schematic illustration of the Toft and Kermode model……24

Figure 3.4 Example of a patient with DCE MRI and concordance for cancer……..26

Figure 3.5 A representative patient prostate MRSI dataset comparing normal and cancerous prostate tissues……..27

Figure 3.6 Polarization versus temperature of ^{13}C, ^{1}H, and electrons……..30

Figure 3.7 The 3D GRASE sequence designed for imaging HP ^{13}C metabolites at a 14T preclinical MRI scanner……..32

Figure 3.8 The slab-selective dynamic HP ^{13}C experiment in a TRAMP tumor……33

Figure 4.1 The fabricated HIFU applicator for ablating murine tumors……..44

Figure 4.2 The setup used for HIFU treatment of TRAMP tumors……46

Figure 4.3 The transverse and axial cross-sections of the ultrasound beam mapped out with a hydrophone in degassed water……..51

Figure 4.4 Representative stained pathologic sections and the corresponding ^{1}H and HP ^{13}C MR images of a large aggressive TRAMP tumor treated with HIFU……..54

Figure 4.5 Representative stained pathologic sections the corresponding ^{1}H and HP ^{13}C MR images of a smaller, less aggressive TRAMP tumor treated with HIFU……..55

Figure 4.6 The representative DCE MRI curves from a mouse at baseline, 3-4 hours after treatment, 1 and 5 days after HIFU treatment……..57

Figure 4.7 A graphical summary of the means ± stand errors change of baseline of HP ^{13}C urea, [1-^{13}C] lactate, DCE MRI AUC, and K^{trans} in the ablated and margin zones of the TRAMP tumor after HIFU treatment……..58

Figure 5.1 The compact ultrasound hyperthermia applicator design……69

Figure 5.2 The setup of the phantom experiment for MR thermometry and phase drift correction verification……73

Figure 5.3 The setup used for hyperthermia treatment of a TRAMP tumor……76

Figure 5.4 The transverse cross section of the intensity beam plot of the ultrasound hyperthermia device……80

Figure 5.5 Average phase drift and real-time phase drift correction verification in phantom……81

Figure 5.6 Temperature maps overlaid on the anatomical images and temperature profiles during the hyperthermia treatment in a mouse bearing a 1.95cm^3 solid prostate tumor……83

Figure 5.7 Temperature maps overlaid on the anatomical images temperature profiles during the hyperthermia treatment in a mouse bearing a 0.58cm^3 solid prostate tumor……85

Figure 5.8 The preliminary ^{13}C MRI data of a mouse treated with 30 minutes of hyperthermia……87

Chapter 1: Introduction

Prostate cancer is the most frequently diagnosed cancer and the second leading cause of cancer death in men.[1] However, effective treatment for low- or intermediate-risk tumor is lacking. These patients either have to deal with the morbidity risks of more aggressive treatments or bear with the pressure of being under surveillance without active treatment.[2]

Currently, thermal therapy is being investigated as an effective treatment option for such cases.[3-8] There are two main types of thermal therapy: thermal ablation and hyperthermia. For ablation, as in high-intensity focused ultrasound (HIFU), the high power and high temperature (~55-90°C, lethal thermal dose) result in immediate cell death and tissue destruction.[9] For hyperthermia, the temperature is maintained between 39°C and 45°C, typically for 30-60 minutes duration.[10] The tissue is sensitized and has elevated perfusion and metabolism, which improves the treatment effectiveness when combined with adjuvant therapies such as radiation therapy and chemotherapy.[10-14] In order to improve treatment delivery and control, MRI can be used in conjunction with thermal therapy to aid in not only targeting tissue but also providing real-time feedback on tissue heating.[3, 15, 16]

In addition to the traditional multiparametric ^{1}H MRI guidance, HP ^{13}C MRS can improve treatment delivery strategies, provide treatment verification, and thus reduce the additional need for more radical therapies. HP ^{13}C MRS imaging has been used to

successfully characterize the aggressiveness (pathologic grade) of prostate tumors[17], and to monitor radiation therapy.[18] HP ^{13}C-labeled compounds are incorporated into metabolic pathways in both physiologic and pathologic processes, and behave chemically in an identical manner to unlabeled, naturally-occurring metabolites. Compared to ^{1}H, the polarization of ^{13}C is low due to the lower natural abundance, gyromagnetic ratio, and concentration.[19] With the technique of dynamic nuclear polarization, the signal-to-noise ratio can be increased by 10,000 fold, allowing the ability to noninvasively monitor real-time metabolism.[19-21] The ability to track not only the injected molecules but also their metabolites is significant.[19] In addition, the rapid acquisition of signal produces images within a clinically useful timeframe such as a breath-hold.[19] Several ^{13}C biomarkers have been proven useful. Specifically, HP ^{13}C-pyruvate has successfully been used to evaluate the stage and aggressiveness of tumors, and the metabolically inactive HP ^{13}C urea has been used to image blood perfusion.[21] Since traditional markers lack sufficient evidence regarding the correlation between histologic specimens and currently available imaging, better imaging biomarkers of successful ablation and reliable correlation with subsequent pathology are important yet unmet needs.[22]

The goal of this thesis project is to understand how murine prostate tumor tissues respond to thermal therapy, including both thermal ablation (HIFU) and hyperthermia. A HIFU applicator was designed and fabricated to generate ablations in murine prostate tumors. HP ^{13}C-pyruvate and HP ^{13}C-urea were used to evaluate the metabolism and perfusion of tumor tissues, as knowing these key metabolic changes paves ways to better treatment planning for adjuvant therapies in terms of the timing and dosage. To examine the effects of

hyperthermia, a compact ultrasound hyperthermia applicator was developed to perform hyperthermia treatments on mice in a 14T MRI scanner (bore diameter = 4cm) with concurrent MR thermometry. *In vivo* heating has been successfully performed in six mice, and the feasibility of applying the technique of HP ^{13}C MRI to monitor metabolic and perfusion changes was demonstrated in one mouse.

The dissertation chapters are organized in the following manner:

Chapter 2 gives an overview of the two main types of thermal therapy, thermal ablation and hyperthermia, and their thermal effects on tissues and clinical applications. Different heating modalities with image guidance as well as platforms for performing thermal therapies on small animals are discussed.

Chapter 3 provides the understanding of MRI basics, dynamic contrast-enhanced (DCE) imaging, and HP ^{13}C imaging. In addition to the current multi-parametric ^{1}H MRI used for evaluating prostate cancer, the technique of hyperpolarized ^{13}C imaging and its biomarkers and advantages are also explained. The chapter ends with the background on MR thermometry imaging, focusing on proton resonance frequency thermometry.

Chapter 4 examines how murine prostate tumors respond to thermal ablation. The metabolic and physiologic changes in the ablated region and the margin region directly adjacent to the ablated region were studied using HP ^{13}C-pyruvate and ^{13}C-urea in addition to the clinical standard DCE area-under-curve (AUC) and K^{trans}.

Chapter 5 describes the compact MR-compatible ultrasound hyperthermia device that's capable of heating small volume murine prostate tumor in a 14T MRI scanner with concurrent MR thermometry. The temperature maps were correlated to the tissue's metabolic and physiologic changes measured with the HP ^{13}C biomarkers.

Chapter 2: Thermal Therapy

2.1 Thermal Therapy and Effects on Tissues

Thermal therapy is the application of heat or cold to the targeted tissue to achieve therapeutic effects. It has played an increasingly important role in cancer treatment as it is minimally invasive and has fewer side effects compared to the traditional more aggressive options, such as surgery and radiation.[9, 23] The two main types of thermal therapy involving the delivery of heat to tissues are thermal ablation and hyperthermia.

2.1.1 Thermal Ablation

Thermal ablation exposes tissues to ablative temperatures above 50°C and lethal accumulation of thermal dose, causing immediate cell death.[24] Since the treated tissue experiences a gradient of temperatures from the heat source, four main zones of tissue response have been identified (Figure 2.1). Closest to the heat source, the highest temperatures result in a thermally fixed zone, where the tissue is not viable but appears to be similar to living untreated tissue on the histology H&E stain with cellular structures preserved.[25] The heat denatures the proteins and desiccates the tissue, preventing enzymatic tissue autolysis and healing pathways from taking place.[26] Reperfusion is typically absent to minimal in thermally fixed tissues, and these tissues resist the breakdown or re-absorption by the body.[26, 27]

Next to the thermally-fixed zone away from the heat source is the coagulative necrosis zone. The temperature isn't high enough to achieve thermal fixing, but the tissue still receives a lethal temperature dose. With complete acute cellular destruction, the tissue is no longer viable, and this damage is irreversible.[28] The diminished cellular and nuclear H&E staining of the coagulative necrosis tissue is described as "pale pink cellular ghost

outlines" by James E. Coad.[26] The coagulative necrosis zone undergoes the classical wound-healing pathway, including inflammation, fibroblast activation, collagen deposition, and wound remodeling.[26]

In between the coagulative necrosis zone and the apparently untreated zone is the margin zone, which consists of a mixture of viable and damaged cells. In the course of the few days after ablation, some cells continue to die due to secondary injury mechanisms (inflammation, apoptosis, ischemia, etc.), while other cells may survive and regrow.[26] Identifying and differentiating this margin zone from the completely ablated regions, and further treating this region is crucial in order to prevent cancer recurrence.[26]

The minimal or non-invasiveness of thermal ablation makes it a desirable alternative to the more aggressive surgeries. Since the energy of the heat source is non-ionizing, and since the ablation is highly localized, thermal ablation causes fewer side effects compared to radiation and chemotherapy, improving the quality of life of the patients. Thermal ablation has been used as a primary treatment option for localized tumors, as well as salvage therapy to recurrence after radiation therapy.[29-33] The benefits of combining thermal ablation with adjuvant therapies such as radiation and chemotherapy have been demonstrated, as these adjuvant therapies effectively address incomplete or heterogeneous destruction of thermal ablation.[23] Radiofrequency ablation combined with radiation increased ablation size and improved the survival of rat tumor models.[34, 35] In the recent years, the use of high-intensity focused ultrasound (HIFU) with

nanoparticles or temperature-sensitive liposomes showed promising results in improving drug delivery and chemotherapeutic effects.[36-40]

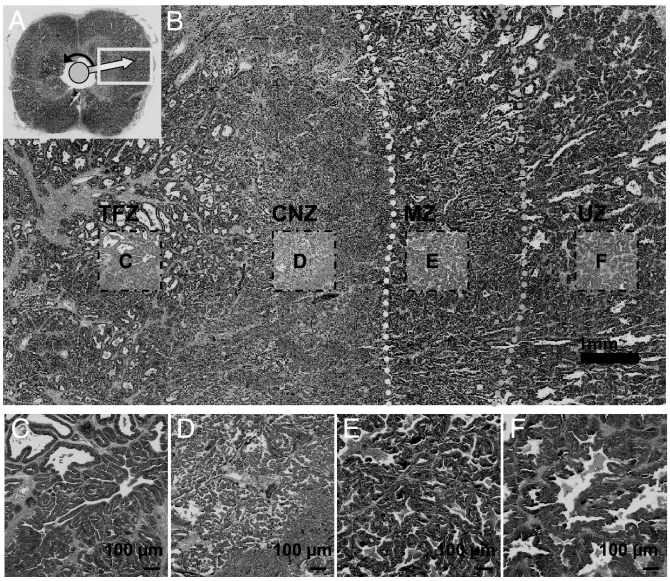

Figure 2.1 A. 5µm section of canine prostate stained with H&E 45 minutes after thermal treatment. The heating applicator was inserted in the urethra. The H&E histology of the tissue in the rectangle in A is shown in B. C: thermally fixed zone. D: coagulative necrosis zone. E: margin zone. F: apparently untreated zone. Adapted from [25].

2.1.2 Hyperthermia

During hyperthermia treatments, tissues are exposed to moderately elevated temperatures for a prolonged period of time, usually at least an hour.[41] Although the exact temperature range hasn't been agreed upon, the general consensus falls between 39°C and 45°C.[42-46] This mild elevation in temperature causes changes at both the cellular and physiological levels.

The main cellular changes are protein denaturation and aggregation.[45] In particular, nuclear protein is especially prone to aggregation when exposed to heat, leading to DNA damage.[46] Reversible changes in cellular membrane permeability towards various compounds, including anticancer drugs, have also been reported.[45] The increased rates of biochemical reactions in response to the change in the temperature result in higher cell metabolism, causing elevated oxidative stress as well as acidosis of tumor tissue.[47, 48]

On the physiological level, hyperthermia affects blood flow, pH, and oxygen pressure. Depending on the tissue/cell type and sensitivity, 42°C to 44°C have been reported as the threshold temperatures leading to opposite changes in these physiologic parameters.[45, 48, 49] Hyperthermia (between the threshold and 45°C) can destroy the vasculature in the tissue, leading to a lower interstitial pH and a decrease in oxygenation.[45, 48, 49] On the other hand, milder hyperthermia (between 39°C and the threshold) promotes perfusion, resulting in a higher oxygen concentration and a lower hypoxia fraction.[43, 45, 48, 49] This increase in perfusion and reoxygenation after hyperthermia can improve the efficacy of adjuvant therapies, including radiation, chemotherpy, and drug delivery.[43, 45]

Hyperthermia is one of the most effective radiation sensitizers, as it is capable of eliminating tumor cells that are resistant to radiation or affecting physiologic conditions so that the tissues become more prone to radiation treatment. By exposing the radiation-resistant cells to temperatures above 43°C or the threshold temperature, DNA repair mechanisms are inhibited due to protein aggregation.[50] An increased amount of radiation-induced chromosomal aberrations was observed in the tissue sensitized with

hyperthermia immediately after radiation treatment.[51] Mild hyperthermia, on the contrary, increases oxygenation and decreases hypoxia of the tumor tissues, which improves the efficacy of radiation treatment.[52] Radiation combined with hyperthermia has been used in the clinic for breast, cervix, rectum, urinary bladder, and other cancer sites, and all demonstrated a significant benefit with the addition of hyperthermia.[13, 53-56]

The synergy between hyperthermia and chemotherapy/drug delivery also is actively under study. Regions that are poorly-vascularized are more resistant to systematic chemotherapy due to the limited delivery of the anticancer drug.[45] Coincidentally, these regions are more susceptible to thermal therapy since no effective cooling can be achieved with limited blood circulation.[45] Hyperthermia (threshold to 45°C) eradicates cells in the poorly-perfused tissues (usually in the center of the tumors) while mild hyperthermia (39°C to threshold) increases perfusion and vascular permeability in the rest of the tumor tissues, facilitating the delivery of the chemotherapy delivery, thereby increasing the drug concentration and uptake in the area.[45, 57] In addition, hyperthermia can also increase the cytotoxic effects of certain anticancer drugs, enhancing the effectiveness of chemotherapy.[45, 58, 59] Improved outcomes when combining chemotherapy with hyperthermia have been demonstrated in clinical trials for high-risk soft-tissue sarcoma, bladder cancer, non-small cell lung cancer, oesophageal cancer, and more.[13, 60-63] When used with temperature-sensitive liposomes or nanoparticles, hyperthermia also allows for targeted drug delivery to tumor sites.[64-66]

In addition to radiation and chemotherapy, immunotherapy has gained more attention over the years since it has the potential to effectively eradicate metastatic cancers.[67] Hyperthermia is known to induce anti-tumor immune response through several different mechanisms. Other than the direct activation of immune cells with hyperthermia, the increased expression of MICA and MHC class I on the surface of the heated tumor cells makes them more susceptible to lysis.[67] The up-regulation of heat shock proteins and increased amounts of exosomes released by tumor cells under thermal stress can both stimulate the anti-tumor immune response.[67, 68] Improved perfusion and modifications in the vasculature adhesion molecules due to hyperthermia further enhance trafficking of immune cells into the tumor.[67, 68] Combined hyperthermia and immunotherapy (specifically, cytokine-activated T cells and dendritic cells) have enhanced the treatment outcomes in clinical trials of many different cancer cases with metastases.[69]

2.2 Ultrasound-based Thermal Therapy

Ultrasound refers to sound waves with frequencies above the upper audible limit of human hearing, approximately 20kHz. The frequencies of therapeutic ultrasound usually fall within the 0.5-12MHz range.[70] Ultrasound waves are typically generated by piezoelectric materials, which are materials that generate an electric charge in response to applied mechanical stress and vice versa.[71] Reflection occurs as the ultrasound beam crosses the boundary between two media. As the non-reflected waves move through and interact with tissues, the ultrasound energy gradually diminishes due to the attenuation in tissues. The rate of attenuation depends on two main factors: (1) the type of tissue, and (2) the frequency of the ultrasound.[72] The depth of penetration decreases as the ultrasound

frequency increases.[72] There are several sources of attenuation, including refraction and scattering, but the main cause of the energy loss is absorption of the ultrasound by the tissues, which generates heat.[72] While the heat production is undesirable for diagnostic purposes, it is the basis for therapeutic ultrasound applications. Depending on the temperature gradients, mild heating, coagulative necrosis, and/or tissue vaporization are all possible biological effects on tissues from the ultrasound exposure.[70]

Ultrasound focusing can be accomplished based on the geometry of the transducer, or by having a phased array. Single-element spherical or curvilinear focused transducers focus the ultrasound energy to a specific region or a focal zone. With more sophisticated 1D or 2D phased arrays where the phase of each element can be controlled independently, electronic focusing and steering can be achieved by adjusting the phase delay of the elements in phased arrays, generating the most optimal heating patterns suitable for each specific treatment goal.[73]

There are several clinically relevant modalities for generating heat in tissues, including ultrasound, radiofrequency (RF), microwave (MW), and laser ablation. While they all are capable of inducing a central coagulative necrosis zone surrounded by a transitional margin zone, ultrasound has its advantages. Compared to the electromagnetic-based modalities (RF and MW), ultrasound provides greater tissue targeting as a result of the fundamentally smaller wavelength, which permits tighter focusing for more precise energy deposition.[74] In addition, while MW antenna may produce more heterogeneous energy deposition, ultrasound applicator allows for more precise spatial control with the

homogeneous heat distribution within the active transducer length.[75] The lesion shapes generated by RF and MW appear to be significantly distorted by tissue irregularities (vessels, sinuses, etc.), whereas similar distortions in lesion shapes were not observed with the ultrasound applicator.[75, 76] Moreover, ultrasound energy is less attenuated at therapeutic frequencies than laser and the electromagnetic-based modalities are, and thus is able to achieve deeper penetration for deep-tissue thermal therapies.[75, 77] However, ultrasound applicators are relatively complex in design and fabrication compared to other modalities such as laser and RF.[77] The high reflection and/or absorption of ultrasound energy at soft tissue-bone and soft tissue-air interfaces also makes treatment planning and delivery more challenging when targeting tissues near or within bones, ribs, spine, bowels, and lungs.[78, 79]

2.3 Image-Guided Thermal Therapy

Image guidance is crucial for improving treatment planning, optimizing treatment delivery, and monitoring treatment outcome. Of all the imaging modalities, magnetic resonance imaging (MRI) offers the best soft tissue contrast as well as the capability of non-invasively monitoring the temperature during the thermal therapy.[80] The superior spatial resolution allows for precise visualization of the targeted tissue, and the high temporal resolution provides temperature feedback for treatment control. Magnetic resonance-guided high-intensity focused ultrasound (MRgHIFU) and magnetic resonance-guided focused ultrasound (MRgFUS) have been used in many clinical applications, including treatment of uterine fibroids, head and neck cancer, prostate cancer, brain tumors,

essential tremor, Parkinson's disease, liver tumors, breast cancer, pancreatic cancer, and bone metastasis.[80-90]

2.4 Small Animal Heating Systems

Various modalities for thermal therapy have been applied to small rodent preclinical experiments. Many early and some recent studies induced whole-body and/or local hyperthermia by immersing the animal body or only the site of tumor, commonly on a limb, in a water bath at a constant temperature (40°C to 45.5°C) for at least 30 minutes.[91-96] Radiofrequency (RF) is another common energy source for performing thermal ablation or hyperthermia in small animals. The RF applicators are low-cost and simple in design, but they require a percutaneous step, making RF thermal therapy not completely non-invasive. Commonly guided by ultrasound (US), computer tomography (CT), or MR, an RF needle electrode is inserted into the tumor (in many cases, the tumors are subcutaneously implanted into the animals) or the targeted tissue. The temperature during the treatment can be verified using thermocouple probes, or MR or CT thermometry imaging.[97-107]

Similar to RF, Microwave is another electromagnetic modality where a needle-like applicator is inserted into the tumor under image guidance.[101, 108, 109] Unlike electric currents as in RF, microwave radiates through all biological tissues and thus achieves more efficient heating, generating more homogeneous and larger volumes of heated tissues with a shorter amount of time.[110] In small animal models, microwave thermal ablation has been demonstrated in rat livers, mouse bladders, and several subcutaneous tumors, including lung cancer and breast cancer.[111-116] For better spatial control, a dual slot

microwave antenna has been developed to produce small spherical ablations tumors in mice.[117] To improve control over temperature during treatments, small animal microwave hyperthermia platform under ultra-high-field MRI guidance with real-time MR thermometry has been applied to heating subcutaneous tumors in mice.[118]

Compared to radiofrequency and microwave, ultrasound is more prevalently used in combination with MR-guidance. There are several commercially available small-animal MRgHIFU or MRgFUS hyperthermia systems compatible with clinical 3T MRI scanners or preclinical 7T MRI systems.[8, 119-122] The positioning motor system is capable of adjusting the location of the focal point to achieve a larger, more uniform heated area of the desired patterns.[8, 121, 122] More advanced platforms integrate real-time closed loop feedback control on the power based on the MR thermometry to better maintain a steady temperature during treatment.[119] However, currently there is no available MR-guided ultrasound system for heating small animals at ultra-high-field MRI scanner with a narrow bore diameter (4cm). Under an ultra-high magnetic field, the sensitivity of MR thermometry is greatly improved, and high-resolution hyperpolarized ^{13}C MR metabolic imaging can be achieved as described in the next chapter of this dissertation.[123-125] Therefore, part of the goal of this thesis project is to design and fabricate a compact MR-compatible ultrasound hyperthermia applicator for murine tumor model with real-time MR thermometry at a 14T MRI scanner.

Chapter 3: MRI Basics

3.1 Fundamentals of Magnetic Resonance Imaging (MRI)

3.1.1 Nuclear Spins and Precession

Atoms with an odd mass number possess nuclear spin angular momentum. As these nucleons spin about its axis, magnetic dipole moment **μ** will be generated. In a static magnetic field B_0, the spins align in the same direction as B_0. The net magnetization moment **M** is

$$\boldsymbol{M} = \sum \boldsymbol{\mu}$$

Precession occurs when **M** points in a different direction than magnetic field **B**. The torque summed over a unit volume is

$$\frac{d\boldsymbol{M}}{dt} = \boldsymbol{M} \times \gamma \boldsymbol{B}$$

where γB is known as the Larmor frequency ω, the frequency that **M** precesses about **B** at. Each nucleus has a unique Larmor frequency it resonates at since each nucleus has a unique gyromagnetic ratio, γ. Table 3.1 lists the gyromagnetic ratio of some common nuclei used in MRI.

Nucleus	$\frac{\gamma}{2\pi}$ MHz/T
^{1}H	42.575
^{13}C	10.705
^{19}F	40.054
^{23}Na	11.262
^{31}P	17.235

Table 3.1 Gyromagnetic ratio of common isotopes used in MRI.[126]

3.1.2 Relaxation

The direction of B_0 is commonly referred to as the z-direction, or the longitudinal direction. If a different magnetic field B_1 is applied in the xy-direction, or the transverse direction, the spins will be "excited" and rotate away from the z-axis at a frequency $\omega_1 = \gamma B_1$. Two types of relaxation occur following the excitation: longitudinal relaxation and transverse relaxation.

Longitudinal Relaxation

The longitudinal component of the magnetization will return to its thermal equilibrium state at a rate described by the following equation:

$$\frac{dM_z}{dt} = -\frac{M_z - M_0}{T_1}$$

Therefore, M_z at any given time after an excitation can be calculated:

$$M_z(t) = M_0 + (M_z(0) - M_0)e^{-t/T_1}$$

The time constant T_1 is known as the spin-lattice time constant. It describes the exchange of energy between the nuclei and the surrounding lattice and therefore characterizes the return of the magnetization to equilibrium along the B_0 field. T_1 is field-dependent since a higher frequency needs more energy exchange.

Transverse Relaxation

The magnetization in the transverse direction diminishes over time after the excitation, and the rate is

$$\frac{dM_{xy}}{dt} = -\frac{M_{xy}}{T_2}$$

At time t after the excitation, M_{xy} is

$$M_{xy}(t) = M_0 e^{-t/T_2}$$

T_2, known as the spin-spin time constant, is related to the broadening of the spins' resonance frequencies as their dipoles in the z-axis interact and causes dephasing of the xy-magnetization. T_2 is independent of field strength.

3.1.3 MR Signal and Contrast

MR image contrast is mainly affected by the spin density ρ, and the tissue-dependent T_1 and T_2. MR imaging acquisition parameters can further accentuate different types of contrast. The sequence repetition time (TR) between excitations controls T_1 weighting, while the gradient echo time (TE) controls T_2 weighting. These parameters affect the signal S in the following way:

$$S = \rho(1 - e^{-TR/T_1})e^{-TE/T_2}$$

Adjusting these parameters changes the types of contrast in the resulting image. A T_1-weighted image is acquired with a sequence that has a short TR and a short TE, while a T_2-weighted image is acquired with a sequence that has a long TR and a long TE. A sequence that has a long TR and a short TE will result in z a spin density-weighted image. The fact that different tissues have different T_1's and T_2's, along with the flexibility of these MR parameters, make MR the best modality for imaging soft tissues. Figure 3.1 and Table 3.2 show various T_1 and T_2 values in different tissues.

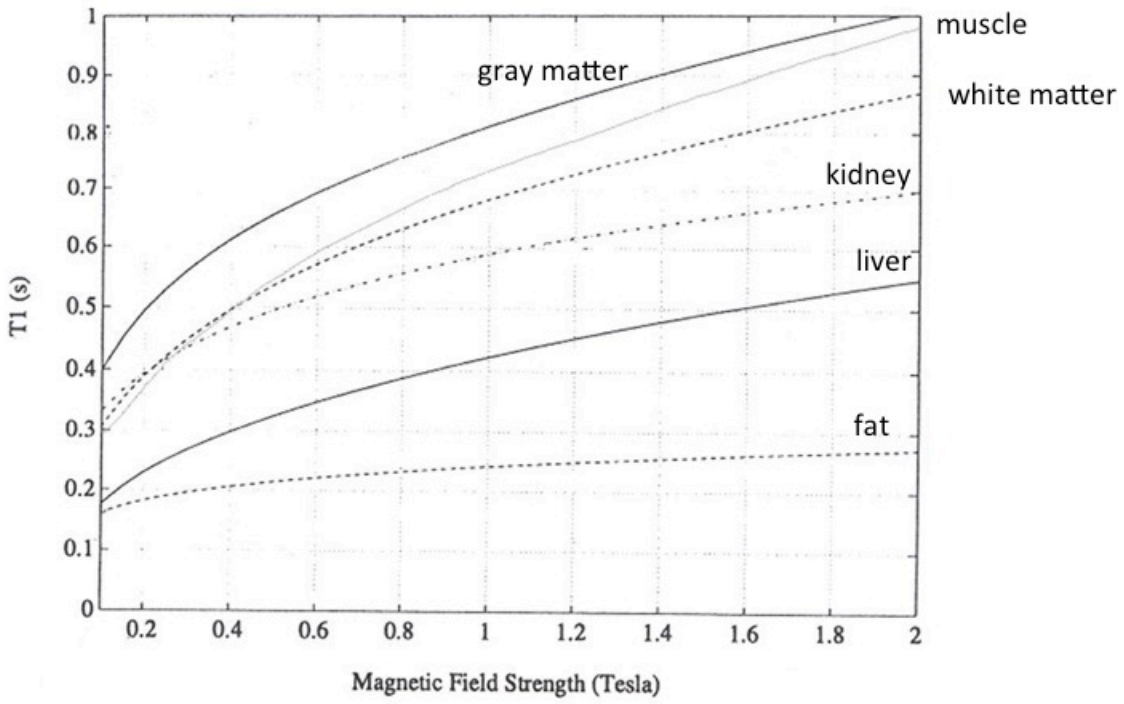

Figure 3.1 Approximate T_1values as a function of B_0. Adapted from [126].

Tissue	T_2 (ms)	Relative spin density
gray matter	100	0.75
white matter	92	0.65
muscle	47	0.61
fat	85	0.90
kidney	58	0.60
liver	43	0.60

Table 3.2 T_2 and relative spin density (water spin density = 1) of some normal tissue types. Adapted from [126].

3.1.4 Chemical Shift

Each nucleus experiences a different local magnetic field due to the orbiting electrons inducing a field that either opposes or reinforces the applied field. The nucleus can be shielded or unshielded, resulting in a different resonance frequency. This phenomenon is the basis for MR spectroscopy, a powerful tool for probing molecular structures, studying chemical exchange rate, and following metabolic processes.[126]

3.2 Multiparametric Imaging of Prostate Cancer

The clinical multiparametric ^{1}H MRI prostate exam has become widely used for the improved staging and risk assessment of prostate cancer for more individualized therapeutic selection and monitoring.[127-129] A multiparametric MRI exam includes T_2-weighted imaging (Figure 3.2(a)), diffusion-weighted imaging (DWI) (Figure 3.2(d) and (e)), dynamic contrast-enhanced (DCE) imaging (Figure 3.2(f) and (g)), and, particularly at UCSF, proton MR spectroscopy imaging (MRSI) (Figure 3.2(b) and (c)).

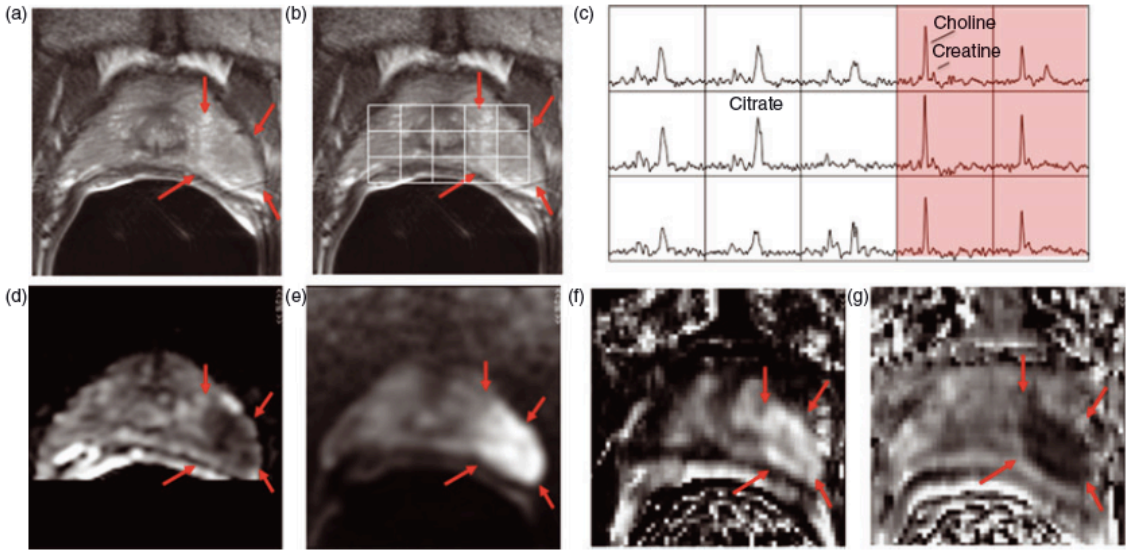

Figure 3.2 Multiparametric ^{1}H MRI exam for a prostate cancer patient. (a) T_2-weighted anatomical image shows a decrease in signal intensity in the left prostate apex (red arrows) associated with prostate cancer. (b) T_2-weighted image overlaid with MRSI spatial grid (resolution = 5.5 x 5.5 x 5.5 mm^3). (c) MRSI spectra show elevated choline and decreased citrate and polyamines in the left prostate apex. (d) Calculated water diffusion coefficient (ADC) image demonstrates reduced ADC in the cancerous region. (e) High b value (b = 1350 s mm^{-2}) DWI image shows increased signal intensity in the region of reduced ADC. (f) Calculated DCE contrast uptake and (g) washout images demonstrate increased uptake and washout in the cancer region. Adapted from [130].

3.2.1 T_2-weighted Imaging

T_2-weighted images provide high resolution, multi-planar anatomical reference. The superior tissue contrast allows for the delineation of the prostate glands. Prostate tumor typically has low signal intensity in T_2-weighted images compared to the surrounding prostate peripheral zone. This hypo-intensity is most likely due to the loss of the ductal structures of the normal prostate gland. The central zone of the prostate usually is more

heterogeneous, making cancer detection more challenging. Benign prostatic hyperplasia, foci of stromal hyperplasia, granulomatous reaction following topical instillations of BCG after resection of bladder cancer, periprostatic venous plexus and neurovascular bundle, and hypertrophic anterior fibromuscular stroma are few of the several factors resulting in hypointensity in a T_2-weighted image, leading to false positive diagnoses.

3.2.2 Diffusion-weighted Imaging (DWI)

Diffusion is the random movements of water and other small molecules in tissue due to thermal processes. This random motion is also know as Brownian motion. In MR imaging, diffusion-sensitized images can be achieved by adding two strong gradients: the first pulse results in an irreversible signal loss through intravoxel dephasing. The second gradient rephrases the spins if no net movement occurs. If movements do occur, the signal will be attenuated. This attenuation depends on the magnitude of the molecular movement, as well as the diffusion weighting, but it is generally characterized by an exponential decay

$$e^{-kDG^2TE^3}$$

where k is a constant, D is the diffusion coefficient, and G is the nonuniform magnetic gradient.[131] Apparent diffusion coefficient (ADC) maps of water are calculated from diffusion-weighted images. A lower ADC value indicates restricted diffusion. In a healthy prostate, ADC values vary depending on the anatomy and structures of the prostate zone. 70% - 75% of the healthy prostate peripheral and transition zones is glandular tissue, allowing for greater diffusion and hence a higher ADC value.[132] The healthy central zone consists of more smooth muscles and potentially a varying degree of benign prostatic hyperplasia. As a result, ADC values in the central zone can be more heterogeneous than

that in the peripheral zone. It's been reported that prostate carcinoma has lower ADC values, which can be explained by the increase in cellular density and the alterations in the prostate glandular structures.[133, 134] A negative correlation has been shown between ADC values and the aggressiveness of prostate cancers.[133, 135, 136]

3.2.3 Dynamic Contrast-Enhanced Imaging (DCE)

DCE MRI is a powerful tool for visualizing the vasculature and studying tissue perfusion. A gadolinium-based contrast agent is injected intravenously. The signal intensity observed during DCE MRI does not directly correlate to the gadolinium concentration. Gadolinium shortens the T_1 of water, and the increase in the relaxation rate is linearly related to the gadolinium concentration in tissue:

$$\frac{1}{T_1} = \frac{1}{T_{10}} + R_1 C$$

where T_1 is relaxation times of water during the dynamic sequence during and after gadolinium injection, T_{10} is the relaxation time without the presence of any contrast agent, R_1 is a relaxation rate constant determined for each contrast agent, and C is the gadolinium concentration during the dynamic sequence. Knowing T_{10} is crucial in estimating C. A T_{10} map can be obtained by acquiring T_1-weighted images with different flip angles prior to the injection of contrast agent.[137] The concentration of gadolinium can be approximated as a function of signal intensity, gadolinium relaxivity, and T_{10}: [138]

$$\frac{S_{Gd} - S_0}{S_0} = R_1 T_{10} C$$

where S_0 and S_{Gd} are the signal intensities before and after the administration of gadolinium.

Semi-quantitative Analysis

Semi-quantitative, model-free analysis is based on signal intensity instead of the concentration of the contrast agent. Properties such as uptake slope, time-to-peak enhancement, magnitude of peak enhancement, area-under-time curve, and wash-out slope are commonly used to interpret DCE MRI results. Several papers have demonstrated the usefulness in detecting cancer, classifying malignant mass, and monitoring changes in tumor post-treatment.[139-142] While the semi-quantitative approach is widely used, generalization across protocols, sequences, and all other factors contributing to the MR signal intensity is its biggest limitation.[143] In addition, these parameters provide no insight into the physiologic behavior of the tumor vasculature and tissue properties.[143]

Quantitative Analysis

Based on the two-compartment pharmacokinetics of the contrast agent, a range of physiological parameters characterizing the functional status of the vascular system within tumors and adjacent tissues can be quantified.[144] Two-compartment Toft and Kermode model (Figure 3.3) assumes equilibrium of the contrast agent between the plasma and the extravascular-extracellular space (EES) and the isodirectional permeability.[145] The equilibrium is

$$\frac{dC_t}{dt} = K^{trans}\,(C_p - \frac{C_t}{v_e})$$

where t is the time, C_t is the contrast agent concentration in tissue, C_p is the contrast agent concentration in plasma, K^{trans} is the influx forward volume transfer constant, and v_e is the fractional volume of EES per unit volume of tissue.

45-60 seconds after the injection of the contrast agent, gadolinium is predominantly intravascular, allowing evaluation of perfusion, relative blood volume, and mean transit time. After the first-pass of the contrast agent, the passage of gadolinium into the extravascular space during the subsequent minutes can be used to characterize the vascular permeability and relative extravascular volume.[144]

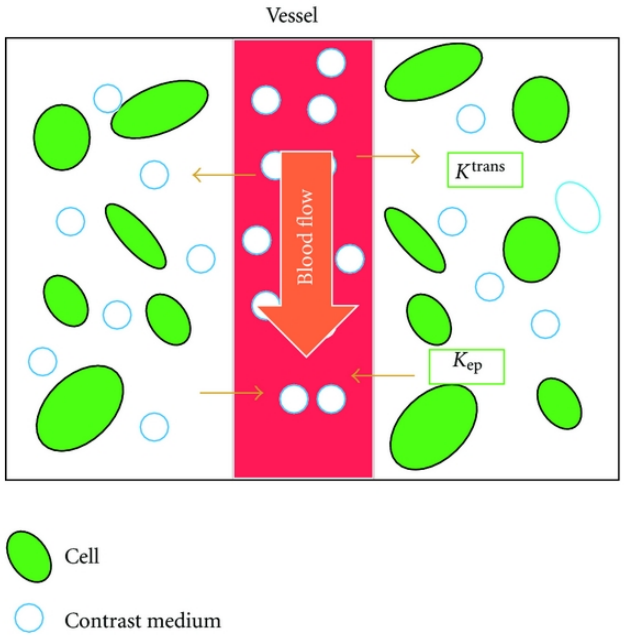

Figure 3.3 Schematic illustration of the Toft and Kermode model. K^{trans} = influx forward volume transfer constant (from plasma into EES). K_{ep} = the efflux rate constant from the EES into plasma. Adapted from [145] .

The traditional Toft and Kermode model was designed for tissues with low vascular fractions and can overestimate K^{trans} in tumors.[145] The following is the modified Tofts model that takes the fractional plasma volume (v_p) into account:

$$C_t(t) = v_p C_p(t) + K^{trans} \int_0^t C_p(\tau) e^{-K_{ep}(t-\tau)} d\tau$$

K^{trans} is the influx diffusive transport of gadolinium across the capillary endothelium from plasma into EES, and $K_{ep} = K^{trans}/v_e$ is the efflux rate constant from the EES into plasma.[146]

DCE MRI for Prostate Cancer

DCE MRI has become one of the most widely used imaging modality for detecting and delineating prostate cancer and/or for assessing the cancer aggressiveness.[147] Tumor vessels have greater permeability and weaker integrity in the vessel wall.[148, 149] Cancerous tissue also has a larger amount of interstitial space, so the contrast material concentration difference between the plasma and the interstitial tissue is larger.[148] Prostate cancer is known to have early intense enhancement and rapid washout of contrast material.[143, 147, 150-153] As shown in Figure 3.4, the voxel with cancerous tissue in the prostate of a patient has rapid uptake and wash-out of the gadolinium contrast agent than the voxels of normal prostate tissue.[150] Quantitative analyses show that elevated K^{trans} and K_{ep} were observed in prostate tumors.[147, 152, 153] DCE is most powerful in aiding diagnosis and detection when used with at least one other method, such as T_2-weighted imaging or ADC.[147, 154]

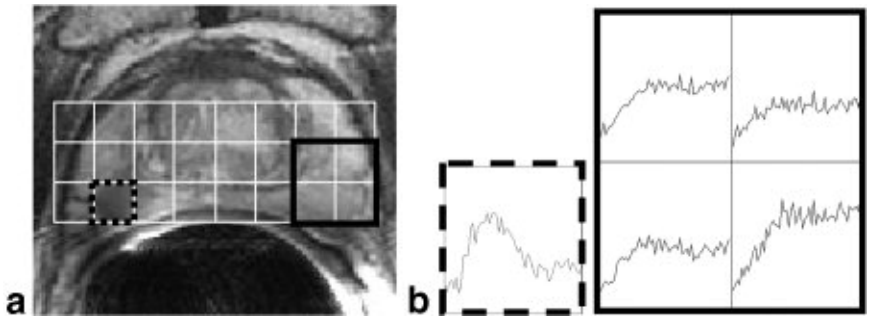

Figure 3.4 Example of a patient with MRI and concordance for cancer, showing a rapid enhancement and washout of contrast agent in the cancerous region (dotted line) vs. the contralateral normal region (solid line). (a) A T_2-weighted image with a grid overlaid. (b) Average DCE data for the regions marked on the grid in (a). Each DCE curve is from data averaged over 7x7 pixels, corresponding to 50mm^2. Adapted from [150].

3.2.4 Proton MR Spectroscopic Imaging (^{1}H MRSI)

Based on the chemical shift properties, MRSI acquires a spectrum of the resonance peaks of various biochemical metabolites from arrays of spatially localized voxels covering the object of interest. When used with the corresponding anatomical T_2-weighted images, MRSI provides metabolic information about prostate tissue by demonstrating the relative concentration of several metabolites that are at high enough concentration to be detectable and change significantly in cancer relative to normal prostate tissue.[148] In prostate cancer, reduced citrate and elevated choline compared to normal prostate tissue have been reported.[148, 150, 155, 156] In normal prostate tissue, high zinc levels inhibit aconitase, resulting in high levels of citrate that are not oxidized in the TCA cycle.[155] In prostate cancer tissue, the ZIP zinc transporters are downregulated, causing a decrease in zinc levels. With reduced zinc levels, citrate oxidation rate increases, resulting in a lower citrate

concentration.[156] As in other human cancers, elevated choline levels are associated with changes in cell membrane synthesis and degradation, cellular proliferation and differentiation, and changes in epithelial cell density. [156-160] Figure 3.5 demonstrates the shift in the citrate and choline relative concentration levels in normal versus cancerous prostate tissue. In the clinic, improved prostate cancer staging and localization has been shown when ^{1}H MRSI was added to the routine MRI exam, and a linear correlation between the magnitude of the decrease of citrate and the elevation of choline with the pathologic Gleason score has been demonstrated.[156, 161]

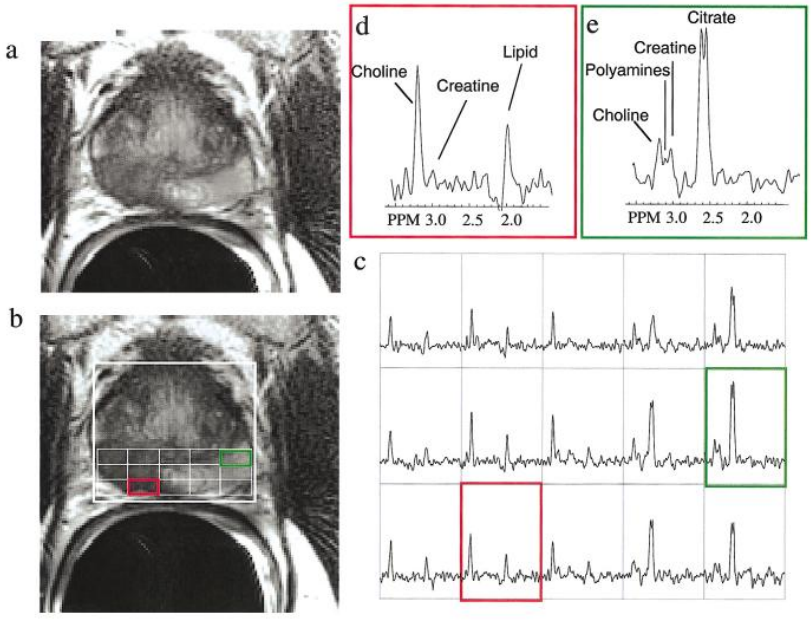

Figure 3.5 A representative patient prostate MRSI dataset comparing normal and cancerous prostate tissues. (a) A T_2-weighted FSE axial image of a large tumor in the right midgland to base. (b) A grid of the axial spectroscopic slices overlaid on the T_2-weighted image. (c) The corresponding 0.3cm^3 proton spectral array. Spectra in (d, red box) regions of cancer demonstrate dramatically elevated choline, and a reduction or absence of citrate relative to (e, green box) regions of healthy peripheral zone tissue. Adapted from [151].

3.3 Hyperpolarized ^{13}C MRI

While the multiparametric ^{1}H MRI exam has improved the sensitivity and specificity of the detection and delineation of prostate cancer, interpreting doubts and misdiagnosis are still problematic.[162, 163] A recent review panel concluded that better real-time metabolic imaging is still needed.[22] Combined with the multiparametric ^{1}H MRI exam, hyperpolarized (HP) ^{13}C MRI has the potential of providing important metabolic and physiologic information that can greatly aid in prostate cancer diagnosis and treatment monitoring.

3.3.1 Dynamic Nuclear Polarization

^{13}C MRSI of injected ^{13}C-laveled metabolic substrates is very challenging without hyperpolarization due to the low gyromagnetic ratio (1/4 that of ^{1}H) compared to ^{1}H MRSI. The technique of dynamic nuclear polarization (DNP) increases the signal-to-noise ratio of ^{13}C MR by more than 10,000 times, enabling real-time imaging of metabolic processes and physiological changes. DNP is based on the transfer of polarization from the electron spins to the nuclear spins. The polarization of nuclei is proportional to the magnetic field but inversely proportional to the temperature:

$$polarization \approx \frac{\gamma h B_0}{4\pi k T}$$

where γ is the gyromagnetic ratio, h is the Planck constant, B_0 is the magnetic field, k is the Boltzmann constant, and T is the temperature in Kelvin. To achieve higher polarization, a higher magnetic field and a lower temperature are the key factors. A DNP sample consists of the ^{13}C-labeled metabolic substrate (probe), a polarizing agent, and an appropriate

solvent.[164] The polarizing agent provides unpaired electron spins and are usually very stable organic-based radicals, such as trityl radicals. The main purpose of the solvent is to dissolve the ^{13}C-labeled probe at high concentration (molar range) and the polarizing radical, which results in a glass at the cryogenic temperatures used during polarization (0.75 to 1.5 Kelvin). Since the DNP polarization process depends on efficient spin diffusion to obtain efficient polarization of the ^{13}C-labeled probe, the probe preparation cannot crystalize.[164] In the pre-clinical hyperpolarizer (HyperSense, Oxford Instruments) used for the studies described in this thesis, the ^{13}C-labeled probes are exposed to a 3.35T magnetic field, and the temperature is kept at around 1.2K with cryogens. The magnetic moment of an electron is 2,700 times larger than that of a ^{13}C nucleus.[165] Under this condition in the polarizer, nearly 100% of the electrons are polarized (Figure 3.6). To provide efficient transfer of polarization from the electrons to the ^{13}C nuclei, the sample is irradiated with microwaves at the resonance frequency of the electron spins. Under the conditions described above, average solution state polarizations obtained from the hyperpolarized probes utilized ([1-^{13}C]pyruvate and ^{13}C urea) in this thesis are in the 20% range. After an approximate hour of polarizing, the sample is dissolved in a heated buffer solution and is brought to a physiologic temperature and pH within seconds. The solution is then injected into the subject, and the imaging is done immediately after.

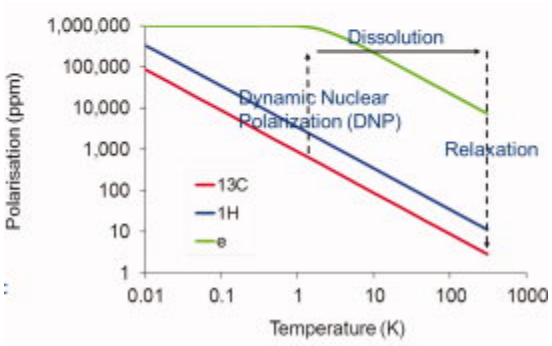

Figure 3.6 Polarization versus temperature of ^{13}C, ^{1}H, and electrons. At 3T and at room temperature, only 0.00025% of the ^{13}C nuclear spins were polarized. Lowering the temperature can achieve almost 100% polarization of the electron spins. As the sample is irradiated with microwaves close to the resonance frequency of the electron spins, electron-nuclear transitions are induced, and the nuclear spin polarization will be enhanced hundred-hold by DNP. Adapted from [165].

3.3.2 ^{13}C-labeled Metabolites

There are several endogenous, non-toxic ^{13}C labeled metabolites that have been successfully used as biomarkers for important biological processes. This dissertation focuses on the conversion of [1-^{13}C] pyruvate to [1-^{13}C] lactate, as well as the use of ^{13}C urea for studying perfusion.

Metabolism: [1-^{13}C] Pyruvate-to-[1-^{13}C] Lactate Conversion

Tumor tissue is known for its Warburg effect: increased levels of glycolysis even in the presence of oxygen.[166-168] Instead of metabolizing glucose by oxidation of glycolytic pyruvate in the mitochondrial tricarboxylic acid (TCA) cycle to maximize ATP production, cancerous tissue undergoes aerobic glycolysis and produces a large amount of lactate from pyruvate even with sufficient oxygen availability.[167, 168] Based on this property, the

hyperpolarized [1-^{13}C] lactate levels after the injection of hyperpolarized [1-^{13}C] pyruvate have been used to noninvasively measure the histologic grade of prostate cancer in the transgenic adenocarcinoma of the mouse prostate (TRAMP).[123] Hyperpolarized [1-^{13}C] pyruvate has also been used in human trials, and elevated hyperpolarized [1-^{13}C] lactate signal was observed in the cancerous regions of the prostate.[169]

Perfusion: ^{13}C Urea

Urea is an endogenous molecule that is not significantly metabolized in vivo; therefore, it is mainly used as a measure of perfusion.[21, 170] It has been used to study blood flow in preclinical murine cancer model, assess rat kidney function, and image cardiac perfusion in rodents.[171-173] One advantage of using hyperpolarized ^{13}C urea for perfusion imaging is that ^{13}C urea can be simultaneously polarized with other compounds, such as [1-^{13}C] pyruvate, allowing both metabolism and perfusion information to be obtained in a single *in vivo* experiment.[174]

3.3.3 ^{13}C MRI 3D GRASE Sequence

For this thesis project, the imaging of the HP ^{13}C studies was performed on a vertical bore 14T preclinical MRI scanner (Varian, Palo Alto, CA) at University of California, San Francisco. One of the main challenges of imaging HP ^{13}C biomarkers is that the magnetization is irreversibly lost due to factors such as resonance frequency saturation, in vivo metabolism, and T_1 relaxation.[175] The 3D GRASE sequence for HP ^{13}C imaging at high fields developed by Sukumar et al. is a single shot, multi-slice, chemical shift specific imaging technique that excites only one resonance at a time, avoiding the problem with

large chemical shift dispersion at 14T (Figure 3.7, [176]).[175, 177] The pulse sequence is essentially a spectral-spatial pulse, followed by two 180-degree refocusing pulses and an EPI acquisition.[175] The 180° refocusing pulses minimize the signal loss due to T_2* effects, which are large at high magnetic fields. With only 153ms of scan time per metabolite, high-resolution ^{13}C images can be acquired (2.5mm x 3.3mm x 3.3mm resolution, field of view = 40mm x 40mm), and images of multiple metabolites can all be obtained from a single injection within seconds. The ^{13}C MR images for all the experiments in this thesis were acquired at 35 seconds after injection. A slab-selective dynamic study from a TRAMP tumor (Figure 3.8, [123]) shows the rationale behind the chosen acquisition time: At 35 seconds after injection, the lactate signal is plateauing, and there is still sufficient pyruvate before the signal drops to the noise level, although differences in pyruvate delivery time could greatly impact the HP lactate-to-pyruvate ratio since the pyruvate is quickly reducing. Fortunately, the pyruvate deliver time was very reproducible in this animal model.[123]

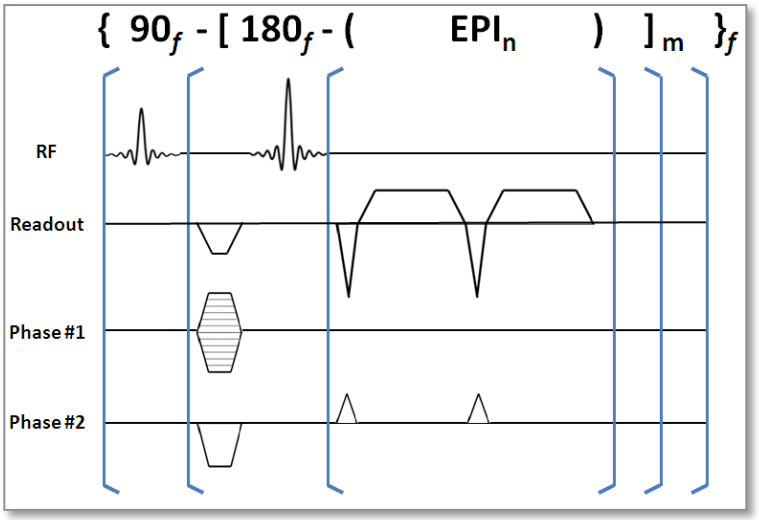

Figure 3.7 The 3D GRASE sequence designed for imaging HP ^{13}C metabolites at a 14T preclinical MRI scanner. n: the number of first phase encode. m: the number of second phase encode. f: the frequency of the metabolite of interest (pyruvate, lactate, etc.). Adapted from [176]. For the experiments in this thesis, n and m are 12 and 16.

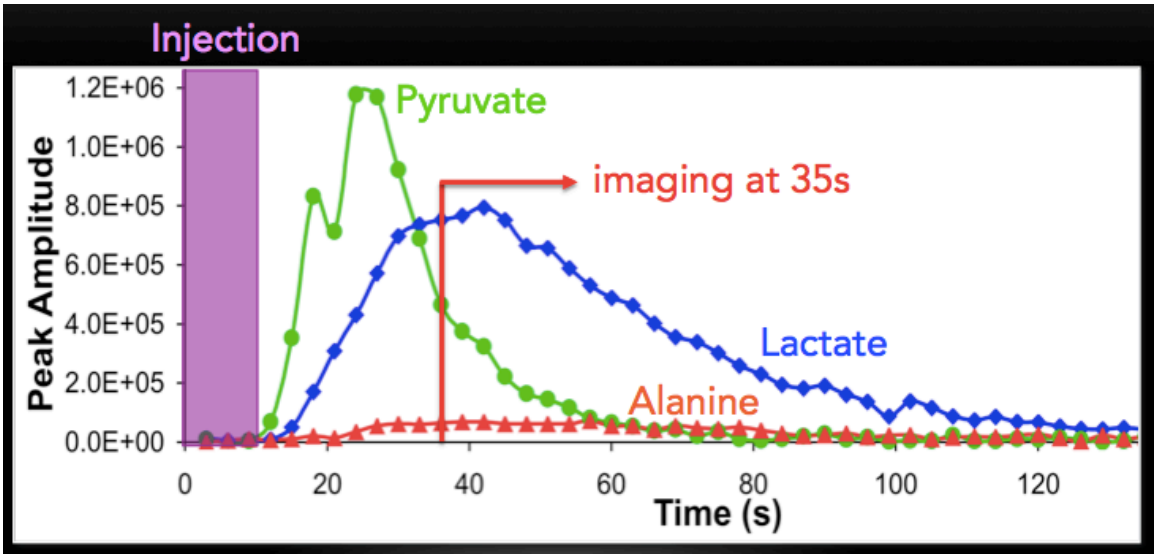

Figure 3.8 The slab-selective dynamic HP ^{13}C experiment in a TRAMP tumor. 350μL of [1-^{13}C] pyruvate was injected at a constant rate during the first 12 seconds through the tail vein catheter. MR spectra were acquired every 3 seconds with 5° flip angle and a 10-mm-thick slice. Adapted from [123].

3.4 MR Thermometry

Focal thermal therapy for low- and intermediate-risk localized prostate cancer has gained more attention in the recent years. More research has been devoted to focal thermal therapy since it is minimally invasive and causes fewer side effects compared to the traditional, more aggressive options, such as surgery and radiation. To achieve accurate heat deposition and temperature control, as well as a safe treatment procedure, real-time temperature monitoring is necessary. MR thermometry can noninvasively provide temperature measurements as well as anatomical images with superior soft tissue contrast. As discussed below, several MR parameters are sensitive to temperature changes.

3.4.1 Temperature-Sensitive MR Parameters

Proton density-weighted images can be used to determine the temperature change. Between 30°C and 76°C, the proton density is inversely proportional to temperature changes by -0.30 ± 0.01%/°C.[124, 178] This change is due to changes in the susceptibility that reflects the shift in the populations of the parallel and anti-parallel spins at different temperatures, not changes in the actual proton density.[124] The proton density method is, however, more robust in fat compared to muscle tissues.[178]

The T_1 relaxation time, or the spin-lattice relaxation, of water describes the dipolar interactions of macromolecules and water molecules through translational and rotational motion. This motion is temperature-dependent, causing T_1 to increase with temperature elevations.[124] The relationship between T_1 and temperature can be described as follows:

$$T_1 \propto e^{-E_a(T_1)/kT}$$

where $E_a(T_1)$ is the activation energy of the relaxation process, k is the Boltzmann constant, and T is the absolute temperature.[124, 179] T_1 has a linear dependence on temperature within tissue when the temperature is below 43°C[180]:

$$T_1(T) = T_1(T_{ref}) + m\,(T - T_{ref})$$

where T_{ref} is the reference temperature, and $m = dT_1/dT$ is the tissue-specific temperature dependence of T_1.[124] At 43°C, the lethal heat dose causes cell death, and at even higher temperatures and thermal doses, coagulation and dessication can occur. As a result of these potential irreversible tissue changes, the linear relationship fails to hold true.[180] While there are MR acquisition sequences that can make T_1-weighted images less prone to motion, its sensitivity drops in higher magnetic field strength.[181]

Since diffusion coefficient (D) is based on Brownian motion, and since Brownian motion is faster as the temperature increases, a higher temperature would lead to an increase in D. The temperature change can be calculated from the diffusion coefficients D and D_{ref} that are acquired at different temperatures T and T_{ref}, respectively[124]:

$$\Delta T = T - T_{ref} = \frac{kT_{ref}^2}{E_a(D)}\left(\frac{D - D_{ref}}{D_{ref}}\right)$$

The advantages of diffusion coefficient-based MR thermometry include its high sensitivity and independence of field strength.[124] However, the temperature dependence of D is not linear, as the permeability of the biological barriers and membranes changes with temperature.[181] In addition, irreversible tissue coagulation, cell swelling, and the water exchange between intra- and extracellular spaces during hyperthermia all result in dramatic changes in D, making this modality unsuitable for this thesis project.[181, 182]

3.4.2 Proton Resonance Frequency (PRF) MR Thermometry

This thesis project adapted PRF-based MR thermometry for monitoring hyperthermia treatments as it does not have the above-mentioned shortcomings of the other modalities.

As water molecules form hydrogen bonds with other water molecules, the electronic configuration of the molecules is altered, leading to less efficient shielding of the ^1H nuclei by the electron cloud. As the temperature increases, the thermal energy causes the hydrogen bonds to stretch, bend, and break.[124, 183, 184] More water molecules remain

in the non-hydrogen bonded state, so more of the ^{1}H nuclei experience a lower local magnetic field B_{loc}, which can be described by the shielding constant σ:

$$B_{loc} = (1 - \sigma)B_0$$

As a result, the resonance frequency becomes:

$$\omega = \gamma B_0(1 - \sigma)$$

Phase Mapping

A gradient-recall echo (GRE) MR imaging sequence can capture the phase change due to the temperature-dependent change in resonance frequency.[185] Multiple baseline images are taken prior to the heating, and the temperature change is linearly related to the phase difference between the baseline image and the subsequent image:

$$\Delta T = \frac{\varphi(T) - \varphi(T_0)}{\gamma \alpha B_0 TE}$$

where φ(T) and φ(T_0) are the phase of the current and the baseline images respectively, ϒ is the gyromagnetic ratio, α is the PRF change coefficient, B_0 is the magnetic field strength, and TE is the echo time.[124] The baseline image is acquired at a known temperature. With the calculated temperature difference from the phase difference, the temperature of the current image can be computed.

Phase Drift

Since PRF-based MR thermometry requires a stable magnetic field, any external changes affecting the magnetic field, such as the use of intense gradients, can cause a drift in the phase that's not due to a change in the temperature.[186] Phase drift can be corrected by

having an oil phantom that is not sensitive to PRF-based thermometry. PRF-based thermometry is based on the bonding and breaking of the hydrogen bonds among water molecules, which are absent in oil. Therefore, any phase changes observed in the oil phantoms will reflect the phase drift of the magnetic field.[187, 188] Drift correction can be applied by subtracting the average of the drifts from all phantoms, by performing a linear correction, or by fitting a linear plane using at least three reference phantoms.[189] Algorithms for higher-order drift correction have also been demonstrated.[190]

Motion

Both intra-scan motion (movements during the MR image acquisition) and inter-scan motion (movements or displacements between the acquisition of images) can cause significant errors in temperature monitoring during treatments.[124] Motion results in a difference in phase from baseline that is not due to a change in temperature. The problem with motion is especially serious in the upper abdominal organs due to respiration. Respiration gating, as applied in this thesis project, can be used to reduce errors caused by respiration.[191] Other methods such as multi-baseline or referenceless (or self-referenced) thermometry can be applied to correct for non-repetitive motions.[192, 193]

Chapter 4: Assessing High-Intensity Focused Ultrasound Treatment of Prostate Cancer with Hyperpolarized ^{13}C Dual-Agent Imaging of Metabolism and Perfusion

4.1 Introduction

Prostate cancer is the most frequently diagnosed invasive cancer in men.[1] However, prostate cancer is extremely variable in its aggressiveness and subsequent history of progression to a lethal disease.[1] Men diagnosed with low- or intermediate-risk localized prostate cancer have historically faced the dilemma of having to select either aggressive definitive treatments such as surgery or whole-gland radiation therapy with their associated complications, or the psychologically burdensome option of active surveillance without treatment.[194, 195] Focal therapies have recently been integrated within the clinic that allow for definitive treatment of low- or intermediate-risk intraprostatic lesions while reducing the risk of significant complications seen with more radical therapy.[196-199] High-intensity focused ultrasound (HIFU) is one of the modalities being investigated as a precision technique for effective thermal ablation for such cases.[4, 199, 200]

HIFU or Focused Ultrasound (FUS) is capable of creating ablative levels of tissue heating within tumor via delivery of ultrasound energy while sparing structures outside of the beam focus.[201] Responses of tissues to thermal therapies depend on both the temperature elevation and the duration. In general, high-intensity ultrasound refers to ultrasound with intensity greater than $5W/cm^2$.[202] Immediate cell death occurs at a temperature beyond 56°C for at least 1 second.[9] During HIFU treatment, a high-power ultrasound wave is focused at the focal point, raising the temperature in the focal zone to

beyond 80°C within seconds.[203] This heat exposure leads to protein denaturation, mitochondrial dysfunction, irreversible cell death, and coagulative necrosis in the ablated zone.[23, 203] In the margin zone (the zone directly adjacent to the ablated zone), a mixture of destroyed tissue and viable cells is observed. The tissues in the margin zone still receive thermal-induced injuries, but the effects can be sub-lethal and reversible.[23] Some of the cells damaged with primary thermal insult will undergo partial cellular breakdown and subsequent recovery.[204] Other cells will die subsequently due to secondary injury (inflammation, apoptosis, ischemia, etc.).[204]

Image guidance, provided by ultrasound or MRI, is crucial in improving tissue targeting and treatment monitoring, and promising results have been shown in various applications in clinical trials.[15, 81, 205-211] The superior soft-tissue contrast and high spatial-resolution make MRI the best imaging method for prostate cancer.[212] The current state-of-the-art for imaging localized prostate cancer, multiparametric (mp) ^{1}H MRI (anatomic, perfusion and diffusion weighted imaging), has demonstrated the ability to localize tumors for subsequent biopsy and focal treatment.[212] In addition, with the ability to provide real-time thermometry feedback, MRI allows for even better controlled heat deposition.[213, 214] Therefore, the combination of HIFU and MR-guidance is a powerful focal therapy modality for localized prostate cancer.[197, 215-218] While there are multiple ways to assess treatment outcome, including ultrasound-measured elasticity and the clinical gold standard dynamic contrast-enhanced (DCE) MRI, these methods only delineate coagulated tissues or the lack of perfusion.[219, 220]. There remains a clinical need to define effective

ablation at an earlier time point and provide critical metabolic and perfusion information on the partially treated regions for improved adjuvant therapy.

Varying heat doses in partially treated regions may cause a diverse effect on residual areas of prostate cancer perfusion and metabolism, which could hold the key to more accurately assessing treatment response at an early time-point and for improving treatment protocols for individual patients. Hyperpolarized ^{13}C MRI is a powerful new metabolic imaging method which uses specialized instrumentation to provide signal enhancements of over 10,000-fold for ^{13}C enriched, safe, endogenous, non-radioactive compounds. The unprecedented gain in sensitivity provided by hyperpolarization can be combined with fast ^{13}C MRI techniques to provide high-spatial resolution images of the injected metabolic probe, HP [1-^{13}C] pyruvate, as well as its down-stream metabolites.[19] Specifically the apparent rate of conversion of HP [1-^{13}C] pyruvate to [1-^{13}C] lactate (k_{PL}) catalyzed by lactate dehydrogenase (LDH) and the associated HP [1-^{13}C] lactate/[1-^{13}C] pyruvate ratio and has shown great potential for not only detecting prostate cancer, but for also assessing the aggressiveness (pathologic grade) of the cancer and its subsequent response to therapy in both pre-clinical and clinical studies.[19, 123, 169, 221-223] Prostate cancer, particularly high-grade prostate cancer, is associated with a high HP [1-^{13}C] lactate/[1-^{13}C] pyruvate ratio and k_{PL} and both are dramatically reduced with effective treatment.

Another important feature of HP ^{13}C MRI is that it can encode chemical as well as spatial information, thereby providing the potential for using multiple HP ^{13}C-labeled probes in order to detect both metabolism ([1-^{13}C] pyruvate) and perfusion (^{13}C-urea)

simultaneously after a single injection of the combined HP probes.[174, 212] Initial pre-clinical studies have indicated that metabolically inactive [^{13}C] urea can be used as a perfusion contrast agent to image blood flow, and has several advantages over gadolinium-based agents, including direct proportionality of signal to tracer concentration, naturally substance at physiologic concentrations and inherently high contrast-to-noise ratio due to the absence of background signal.[174] As mentioned above, DCE MRI currently serves as the clinical gold standard of assessing HIFU treatment efficacy, and in this study the serial HP ^{13}C-urea change after HIFU was compared to DCE MRI to assess whether it provides similar or improved information. Methods for co-polarizing ^{13}C-pyruvate and ^{13}C-urea have also been developed, successfully polarized, and injected in pre-clinical models to simultaneously measure perfusion and metabolism.[174] In a recent dual probe (^{13}C urea and [1-^{13}C] pyruvate) HP ^{13}C MRI pre-clinical study of prostate cancer, significant changes in ^{13}C-urea (perfusion) was able to distinguish high- from low-grade cancer.[222] Currently, there is no published data on the temporal changes in perfusion and glycolytic metabolism that occur with complete ablation or partially HIFU treated tissues.

In this study a combined HP dual agent (^{13}C-pyruvate and ^{13}C-urea) ^{13}C MRI/mp-^{1}H MRI approach was used to characterize temporal changes in prostate cancer metabolism and perfusion after exposure to ablative and sub-lethal doses of HIFU using a transgenic adenocarcinoma of mouse prostate (TRAMP) model [224, 225] and a focused ultrasound applicator designed for murine studies. The overall goal of the study is to establish early HP ^{13}C MRI metabolic and perfusion changes that predict effective HIFU treatment and lead to improved adjuvant treatment of partially treated regions.

4.2 Material and Methods

4.2.1 Murine Tumor Model

The TRAMP model is a well-established murine prostate model that closely mimics the progression of human prostate cancer.[224, 225] Specifically, the perfusion and metabolism of TRAMP model mimic human disease.[222, 226] Mice of C57Bl6 X FVB background, (n=5) weighing 30-40g with solid prostate tumor of 1.5-2.2 cm^3 were selected for HIFU treatments (Table 4.1). Tumor size was determined by identifying the tumor region of interests (ROIs) on the T2-weighted anatomical MRI images. During the HIFU treatment and the MRI session, mice were anesthetized with 1%-2% isoflurane. A pressure sensor (SA Instruments, NY, USA) for respiration monitoring was placed under the animal, positioned within the mouse holder and the coil that fit in the 14T MRI scanner. The respiration rate was maintained at 60-75 breaths/minute.

Mouse #	Tumor Volume (cm^3)	Lac/Pyr	Number of Sonica-tions	Input Power (W)	I_{SPTA} (W/cm^2)	Duration (s/sonica-tion)	Estimated % of tumor ablated
1	2.039	1.06±0.77	1	15	400.92	90	50%
2	1.759	2.28±0.60	2	12	303.00	60	35%
3	2.225	3.01±1.08	2	12	303.00	60	50%
4	1.485	1.46±0.63	2	12	303.00	45	40%
5	2.037	2.38±1.23	2	11.6	292.90	45	20%

Table 4.1 Summary of the tumor volumes, baseline tumor lactate-to-pyruvate ratio (an indicator for tumor aggressiveness), treatment parameters (power and duration), and ablated volumes in the five mice studied.

4.2.2 Small Animal FUS Device—Fabrication and Characterization

Small focused ultrasound applicators were fabricated in-house, using spherical focused transducers (PZT-4 material, 12.7mm diameter, 41.4mm radius of curvature, 5.6MHz) mounted on a 3D-printed acrylonitrile butadiene styrene (ABS) housing designed to provide air backing, conduits for RF power leads, and fluid injection port (Figure 4.1). This configuration was selected based upon practical constrains of size, frequency, and availability to provide a defined region of ablation within these mouse tumors, and not a small discrete focal zone. The transducer housing was integrated with a conical shaped standoff with a 1-cm diameter window, and filled with degassed water in order to couple the acoustic energy to the mouse and to adjust the distance such that the focus was within the tumor. The custom applicators were characterized and calibrated with intensity beam plots using a 3D computer controlled scanning system (Velmex Inc., Bloomfield, NY) with a calibrated hydrophone (HNP-0400, Onda Corp, Sunnyvale, CA). Applicators under test were operated in burst mode at 200 cycles with 1kHz repetition following standard measurement methods, and the peak-to-peak voltage from the hydrophone was measured using an oscilloscope (Keysight DSO-X-2024A 200MHz Digital Oscilloscope, Keysight Technologies, Santa Rosa, CA) and converted to intensity. Maps of the distribution and the peak intensity for applied powers were measured in degassed water. Intensity beam plots of the X-Z (coronal) and X-Y (axial) planes were acquired. The step sizes were 0.2mm along the X and Z axes and 1mm along the Y axis. The acoustic output power as a function of electrical input power (2W-16W) was measured using the radiation force balance technique, and used to scale applied power for desired high intensity delivery during animal studies.

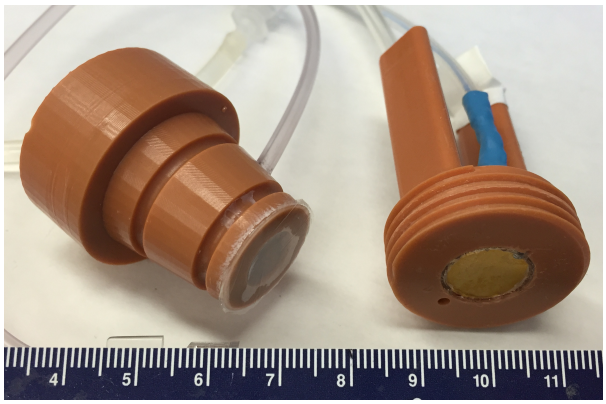

Figure 4.1. The fabricated HIFU applicator for ablating murine tumors. Right: The ultrasound transducer mounted on the ABS housing. The backend has conduits for RF power leads, and fluid injection port. Left: The conical shaped standoff with a 1-cm diameter window for adjusting the distance such that the focus was within the tumor.

4.2.3 FUS Tumor Ablation

The ventral and dorsal abdominal regions of the mouse around the tumor was depilated for efficient coupling of the ultrasound energy, and the applicator tip was placed and compressed over either left or right side of the tumor target region and coupled to the skin with ultrasound transmission gel. The applicator was positioned from a ventral-lateral approach so that no major organs were in the ultrasound beam path to avoid injuries in other organs. A 30 durometer rubber absorber and intermediate gel pad, with acoustic gel was positioned on the opposite side of the tumor to absorb and dissipate the exiting ultrasound energy, and to prevent reflection. RF power was applied continuous wave using a single channel from a four-channel amplifier (Advanced Surgical Systems, Inc.; 500-009 RF generator), and the sonications were performed at 5.6 MHz, 11.6-15W net electrical power, spatial-peak temporal-average intensity (I_{SPTA}) = 292.9-401.9W/cm^2 for 45 to 60

seconds. Each mouse received 1 to 2 treatments depending on the size of the tumor. The goal was to generate ablated and partially treated regions within the same TRAMP tumor for serial imaging studies, not to ablate the entire tumor or a specific discrete region for assessment of therapeutic efficacy. Therefore, ablative ultrasound intensities were directed toward one side or half of the tumor. A high-intensity and long-duration (60s) HIFU treatment was performed on Mouse 1, and then the power setting and duration were adjusted for the following mice to achieve optimal outcomes. For the subsequent mice, two sonications were performed for each mouse at a lower power and a shorter duration. Between the two sonications, the location of the applicator was shifted slightly (~1mm) in order to generate a larger thermal damage zone. Figure 4.2 shows the setup schema and a photo taken during a HIFU treatment. Table 4.1 lists the HIFU treatment parameters applied for TRAMP mice of varying tumor size and baseline metabolic activity that were studied. Both the HIFU intensity and duration were also varied between mice to allow for differing ablated and partially treated regions.

(a)

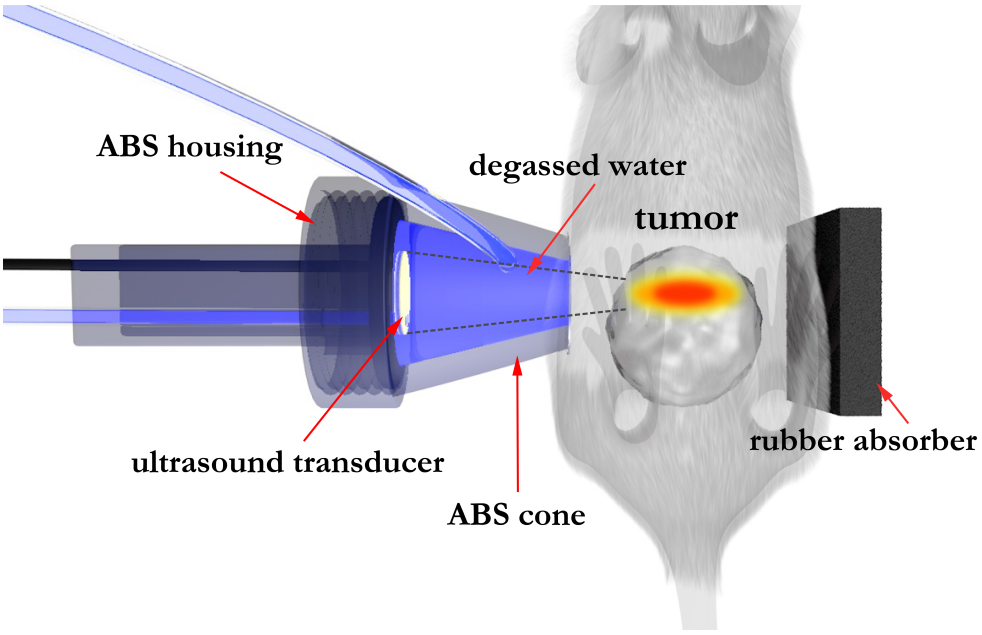

(b)

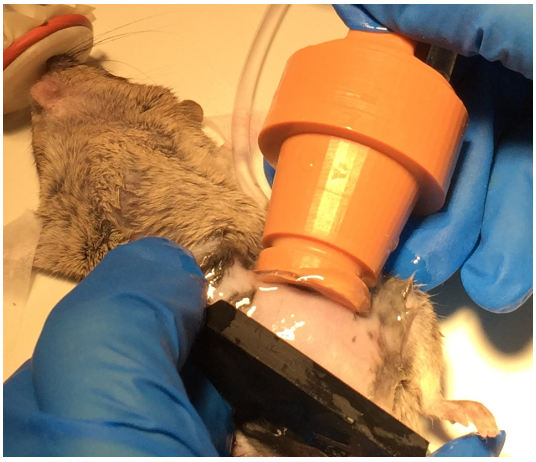

Figure 4.2. (a) Diagram showing the setup used for HIFU treatment of TRAMP tumors. The cone of the focused ultrasound applicator was filled with degassed water to adjust the depth such that the focal zone fell within the tumor. The ultrasound power and duration (Table 4.1) were adjusted to produce regions of ablation and partial treatment in all five TRAMP mice treated. The rubber absorber was positioned to absorb and dissipate the leftover ultrasound energy, and prevent reflections. Acoustic gel was applied at the interface between the mouse and the cone, and between the mouse and the rubber absorber. (b) A photo taken during a HIFU treatment on a mouse.

4.2.4 MR Imaging

The MR imaging was performed on a wide-bore 14T micro-imaging system (Varian Instruments, Palo Alto, CA) equipped with 1000 mT/m gradients and multi-nuclear capabilities. Each imaging study included (1) T_2-weighted images for anatomical references (TE/TR = 20/1200 ms; voxel size 0.16x0.16x1 mm^3, field of view 4cm x 4cm), (2) diffusion-weighted imaging (DWI) using a spin-echo diffusion weighted sequence (TE/TR = 20/1200ms; voxel size 0.31x0.31x1mm^3, field of view 4cm x 4cm, diffusion gradient amplitude 39G/cm, gradient duration 2ms, gradient separation 13ms, four b-values were used: 25, 188, 331, and 514s/mm^2), (3) DCE MRI acquired using a T1-weighted gradient echo sequence serving as a comparison to the clinical standard (TE/TR = 1.11/39 ms; voxel size 0.31x0.31x1 mm; acquired over 5 minutes), and (4) the co-hyperpolarized [1-^{13}C] pyruvate and ^{13}C urea (voxel size 2.5x2.5x2.5 mm). The contrast agent gadolinium solution used for DCE MRI was made with Magnevist© at 1:6 dilution. A volume of 150μL of the gadolinium solution was injected through the tail vein catheter followed by 150μL flushing saline solution over a total of 30 seconds. The [1-^{13}C] pyruvate and ^{13}C urea samples, as well as the buffer solution, were prepared following the previously published protocols.[123, 171] Once the samples were polarized, a dissolution step brought the samples back to physiologic temperature, and 450μL of the solution was injected through the tail vein catheter over 15 seconds. As determined in the previous studies, the ^{13}C images were acquired 35 seconds after the injection.[123] The ^{13}C data were acquired in the following order: (1) a 2-degree flip angle spectrum, (2) the 3D images of pyruvate, lactate, and urea using a 3D GRASE sequence,[227] and (3) a 90-degree flip angle spectrum. The spectra served as a supplemental verification of proper polarization levels and

successful injections. These imaging studies were performed at four time points and comprise a baseline acquired 1 day before the treatment, 3-4 hours after the HIFU treatment, and both 1 and 5 days post-treatment.

4.2.5 Histopathology

Mice were sacrificed immediately after the last imaging time point, and the resected tumors were sliced in 3-mm sections and immersed in a freshly prepared solution of 2% (w/v) triphenyl tetrazolium chloride (TTC) in phosphate-buffered saline (PBS) for 25 minutes at room temperature. TTC is a tissue viability stain.[228] Functional dehydrogenases and cofactors convert the colorless TTC into a bright red pigment, while the non-viable tissues stay in the native color. Pictures of gross pathology were taken before and 25 minutes after the TTC staining. The tissues were then fixed in 10% buffered formalin, transitioned into ethanol, and embedded in paraffin blocks. The sliced tissues underwent standard histological processing and H&E staining, and sections were registered to the corresponding MR images. Based on the pathology, an investigator (RB) highly experienced in murine pathology identified two types of treated tissues as a result of different heat exposures: (1) complete ablation: regions not stained by TTC (appeared as the native tissue color) that had less than 10% viable, intact structures on H&E, (2) margin zone: regions with a weaker TTC staining that had less than 50% necrosis/fibrosis/coagulation on H&E, and (3) non-lethal exposure or untreated tumor tissues: regions with dark red TTC staining and appeared viable on H&E. The identified regions were correlated to the T2-weighted, HP ^{13}C, and DCE MRI results.

4.2.6 Data Analysis

The MR apparent diffusion coefficient (ADC) maps were calculated from the diffusion-weighted images using VNMRJ 4.0 (Agilent Inc., Santa Clara, CA, USA). The ablated and margin zones were identified on the T2-weighted, ADC, and DCE MRI images and verified with histopathology. These regions of interest (ROI) were drawn on the DCE MRI data using the Editor module in Slicer3 (http://www.slicer.org).[229] The means of the ROI's were calculated using LabelStatistics under the Quantification module. The same regions were then identified on the T2-weighted anatomical images and then overlapped onto the ^{13}C images using custom software developed in-house programmed in IDL Software.

Pharmacokinetic modeling was applied to the intensity-over-time DCE MRI data, based on the extended Tofts Kermode model using a native T1 = 1.4s and a relaxivity, r_1 = 3.7L/(mmol × s), and v_p = 0.1.[230] The arterial input function (C_p) was characterized using a bi-exponential function, based upon a study performed in mice, where $C_p(t) = Amp \times D(a_1 \exp\{(t - t_0)m_1\} + a_2 \exp\{(t - t_0)m_2\})$, and where Amp = 20, D = 0.62 mmol/kg of Gd-DTPA, a_1 = 0.1 kg/L, m_1 = 0.0175/min, a_2 = 0.19 kg/L, m_2 = 0.00115/min.[231] The Amp was introduced to account for overall signal differences between our experimental measures and the one from the literature, and as only measures normalized to pre-treatment values were reported. The model was fit to the data using non-linear least squares estimation with the "optim" function in R (R Foundation for Statistical Computing, Vienna, Austria).[232] The quantitative DCE transfer constants (K^{trans}) were computed, and the values were normalized to the baseline values prior to the treatment. The DCE MRI images were then converted into concentration of gadolinium, and to calculate the area

under the curve (AUC), the concentration was summed over a time course of 5 minutes with 6-second intervals.[233] The DCE MRI AUC data in the tumor was normalized to the DCE MRI AUC data in normal muscle tissues. For each time point, the means were computed for each mouse and then averaged among all mice.

The spectrum acquired with a 2-degree flip angle immediately before the 3D GRASE images was used to normalize the ^{13}C data. The ^{13}C pyruvate and lactate signals were normalized to the pyruvate signal from the spectrum, while the urea signal was normalized to the spectral urea signal. Only voxels with signal-to-noise ratios larger than 3 were considered. All voxels used to analyze a region were completely within the defined boundary (i.e. voxels on the boundary of the ablated region and the margin zone were not considered).

The means of the ^{13}C-labeled lactate, pyruvate, and urea imaging results as well as the DCE MRI AUC and K^{trans}, and the ADC, were calculated at baseline and each of the post-treatment follow-up time points. The significance of each of the post-HIFU time points compared to baseline was reported using the standard Mann-Whitney-Wilcoxon rank signed test, $p<0.05$.

4.3 Results

4.3.1 Small Animal FUS—Acoustic Characterization

Figure 4.3 shows the intensity beam plots of the coronal and axial cross sections of the focused ultrasound applicator beam pattern, as measured outside of the distal conical tip, and represents the portion to be positioned within the tumor. The full width half max of the

coronal slice of the ultrasound beam was 0.8mm, and the 50% contour of the beam intensity extended 9mm from the surface of the cone. As measured by the radiation force balance, the acoustic efficiency of the ultrasound HIFU applicator ranged between 35-45%. The required applied power level to deliver the desired focal intensity for each animal experiment was scaled from the low power calibration measurements using this measured efficiency, with 11.6-15 W power delivery required to generate focal intensities of I_{SPTA} = 292.9-400.9W/cm^2 as in Table 4.1 for ablative doses of HIFU to be applied to the murine tumors. With the narrow beam width and high intensity delivery, local ablation was effectively achieved in all five TRAMP mice.

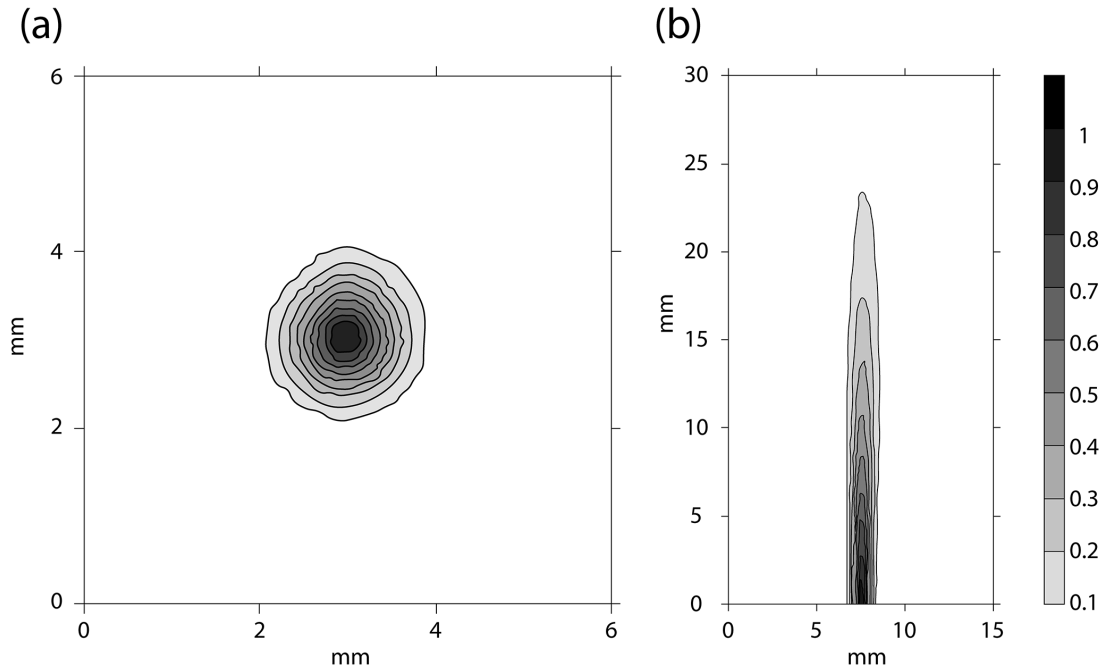

Figure 4.3. The (a) transverse (4mm from the cone surface) and (b) axial cross-sections (starting from 2mm from the cone surface) of the ultrasound beam mapped out with a hydrophone in degassed water. The beam plots were performed with the cone attached (Figure 4.2). As shown in (b), the focal zone was adjusted such that it was near the surface of the cone where the top of the tumor would be positioned.

4.3.2 Pathologic and Imaging Effects of HIFU

Figures 4.3 and 4.4 show representative sets of HP ^{13}C/mp-^{1}H MRI serial data with associated pathology from mice having 2.2cm^3 and 1.5cm^3 tumors treated with HIFU. The baseline HP ^{13}C lactate/pyruvate ratios were 3.01 ± 1.08 and 1.46 ± 0.63, indicating a range in metabolic activity consistent with varying pathologic grades of these tumors.[123] The baseline HP ^{13}C lactate/pyruvate and tumor volumes for all 5 mice studied (Table 4.1) demonstrate a range of cancer aggressiveness, from a ratio of 1.06 indicating a less aggressive tumor, to 3.01 as in a late-stage prostate tumor. In the ablated region 5 days after HIFU, both TTC (Figure 4.4a and 4.5a) and H&E staining (Figure 4.4b and 4.5b), Ki-67 (Figure 4.4c and 4.5c) and PIM (Figure 4.4d and 4.5d) demonstrated fragmented, non-viable cells consistent with coagulative necrosis.[204] In the partially treated tissue surrounding the ablated regions (margin zones) a mixture of destroyed tissue and viable cells were observed. As shown in Table 4.2, the viable cells were highly proliferative (mean Ki-67 staining 89.6% ± 4.3%). About 25% of the viable tumor was hypoxic (PIM staining positive for 25% ± 1.6% of the tumor) and were pathologically poorly differentiated (98.6% ± 1.0% of the tumor cells being poorly differentiated). The two mice had 1.1cm^3 and 0.6cm^3 ablated regions, respectively. The ablated and margin zones were then registered to the MRI T_2-weighted anatomical images (Figure 4.4e and 4.5e) in order to compare changes in measurements of metabolism (normalized HP ^{13}C lactate) and perfusion (normalized ^{13}C urea and DCE MRI). Figures 4.4e and 4.5e shows representative imaging results at baseline, 3-4 hours, 1 day and 5 days post HIFU treatment. For both mice at baseline, normalized images of HP ^{13}C lactate and HP ^{13}C urea, DCE MRI AUC were heterogeneous in intensity but clearly observable throughout the TRAMP tumor consistent

with viable metabolically active prostate cancer. Despite differences HIFU dose applied and the associated shape and size of the ablated region in the two cases, a similar post-treatment tissue response was observed. In the pathologically ablated regions, the intensity of normalized HP ^{13}C lactate or HP ^{13}C urea and gadolinium AUC images were reduced to the level of the noise by 3 to 4 hours after treatment. Neither metabolism nor perfusion showed signs of recovery in the ablated regions by the 5-day time point in either case. In contrast, the partially treated zone had an initial decrease in metabolism (normalized lactate images) and perfusion (normalized urea and DCE MRI AUC images) 3-4 hours after treatment, followed by recovery back to or beyond baseline values by 5 days after treatment.

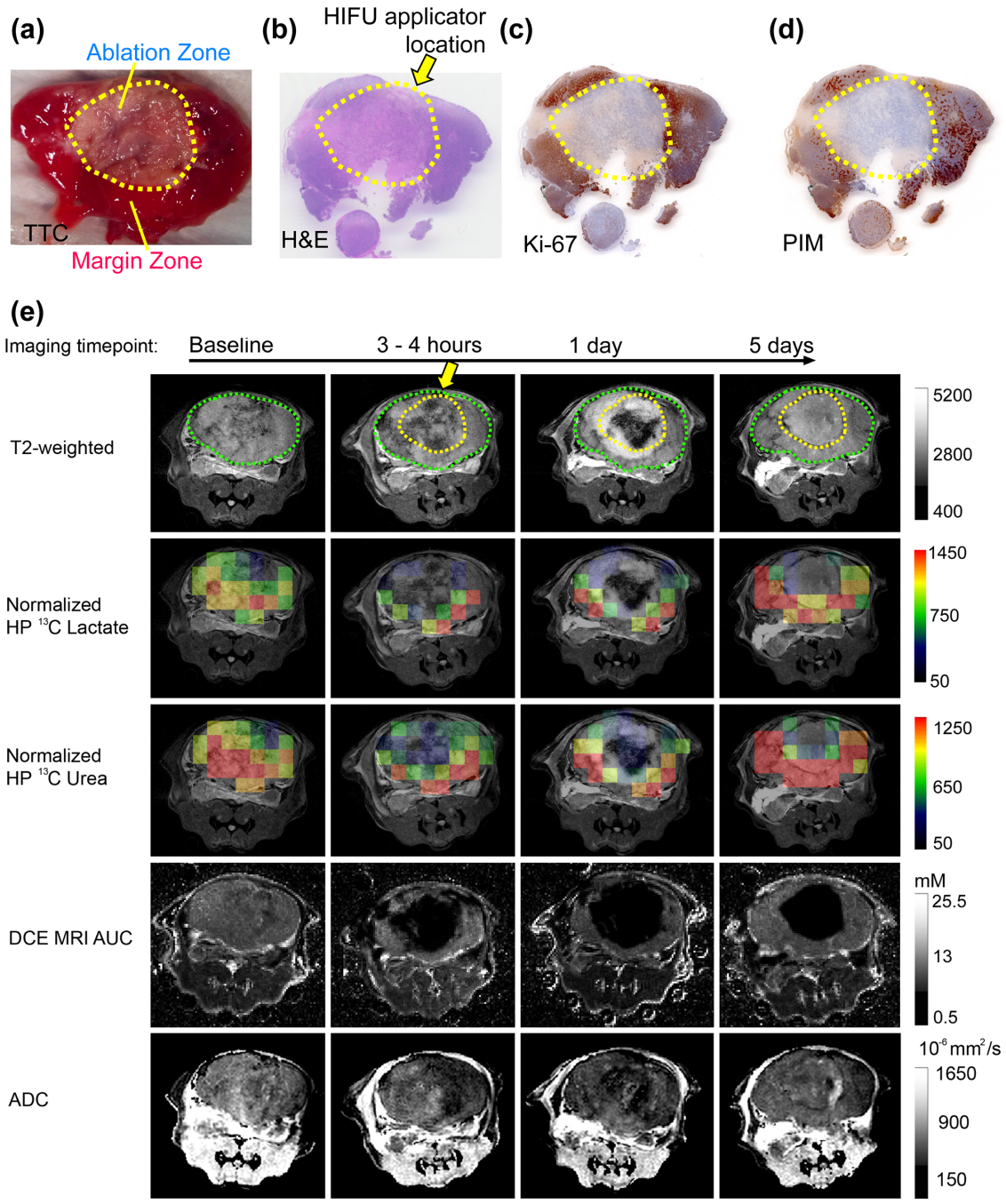

Figure 4.4. Representative (a) TTC, (b) H&E, (c) Ki-67, and (d) PIM stained pathologic sections, and (e) the corresponding T_2 weighted images, overlaid HP ^{13}C lactate, ^{13}C urea images on the T_2 weighted images, DCE MRI AUC, and ADC of a large aggressive TRAMP tumor (Mouse 3). The position of the HIFU applicator is indicated by the yellow arrow. The region of ablation is demarcated by a dashed yellow line, and the outline of the TRAMP tumor is demarcated by the dashed green line. The margin zone was the region between the yellow and green lines.

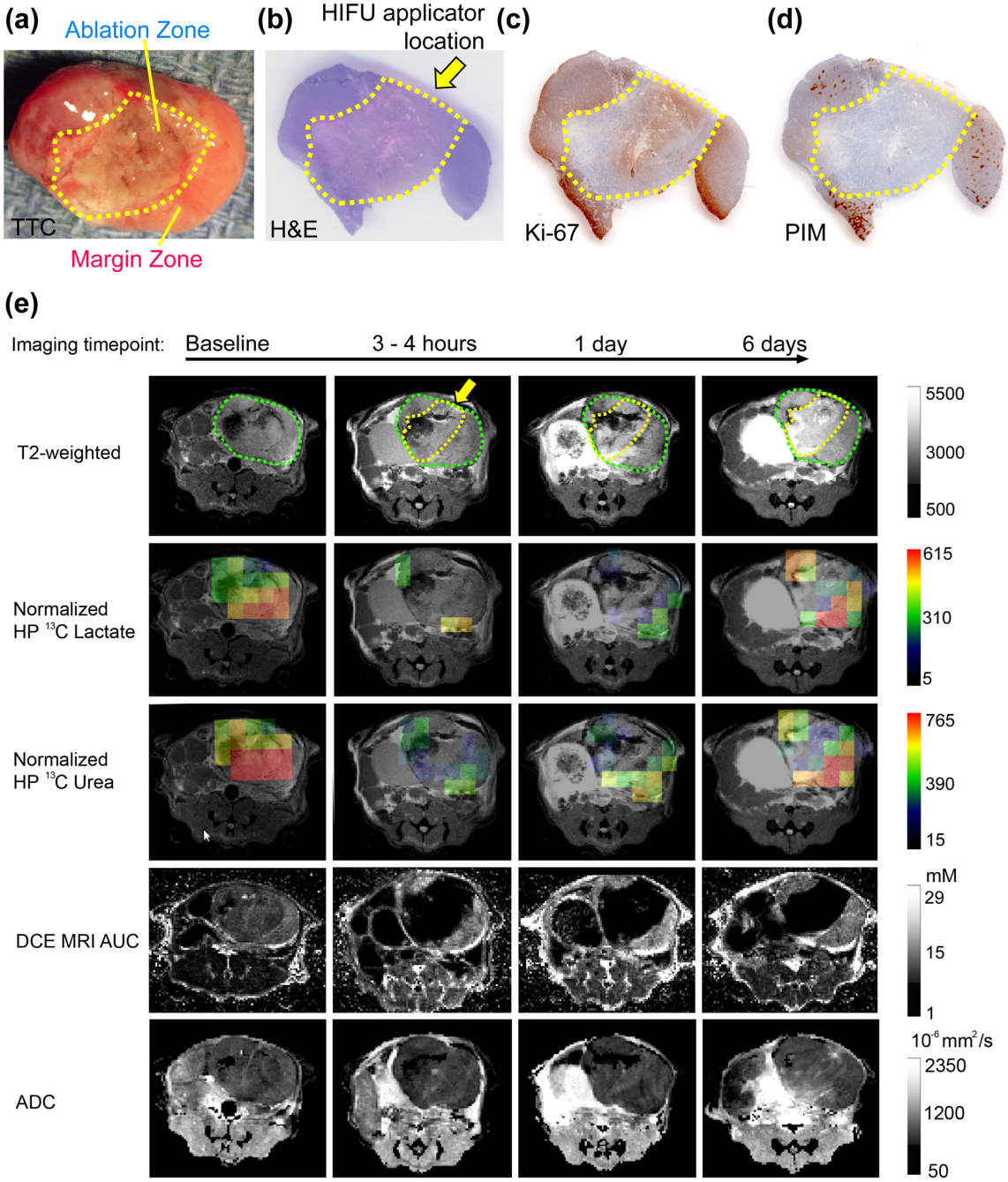

Figure 4.5. Representative (a) TTC, (b) H&E, (c) Ki-67, and (d) PIM stained pathologic sections, and (e) the corresponding T_2 weighted images, overlaid HP ^{13}C lactate, ^{13}C urea images on the T_2 weighted images, DCE MRI AUC, and ADC of a smaller, less aggressive TRAMP tumor (Mouse 4). The position of the HIFU applicator is indicated by the yellow arrow. The region of ablation is demarcated by a dashed yellow line, and the outline of the TRAMP tumor is demarcated by the dashed green line. The margin zone was the region between the yellow and green lines.

	H&E (%)			
Mouse #	Poorly differentiated	Well differentiated	Ki-67 (% stained)	PIM (% stained)
1	100	0	95	30
2	100	0	95	20
3	95	5	98	25
4	100	0	95	30
5	98	2	75	25

Table 4.2 The histology readings of H&E, Ki-67, and PIM of the partially treated zones of all five mice after the 5-day imaging time point.

Figure 4.6 shows representative DCE MRI data in the margin zone of Mouse 2 treated with HIFU. The pre-treatment DCE MRI curve (blue) is consistent with the presence of high-grade prostate cancer: fast wash-in and fast wash-out of the gadolinium contrast agent.[234, 235] At 3-4 hours after the treatment (red), the time to peak DCE MRI intensity is longer (200s vs. 100s), the plateau of the DCE intensity curve increased, and minimal contrast agent wash-out was observed. These changes are consistent with early vascular congestion and rupturing [236], and an increase in the extravascular, extracellular space volume fraction (v_e) from cell death due to the thermal dose delivered to this region. One day after the treatment (orange), the wash-in slope was still lower than the baseline values indicating the vasculature hadn't fully recovered. Five days after the treatment (green), both the wash-in and wash-out slopes were higher than baseline, consistent with the pathologic finding of a poorly differentiated residual tumor (Table 4.2).

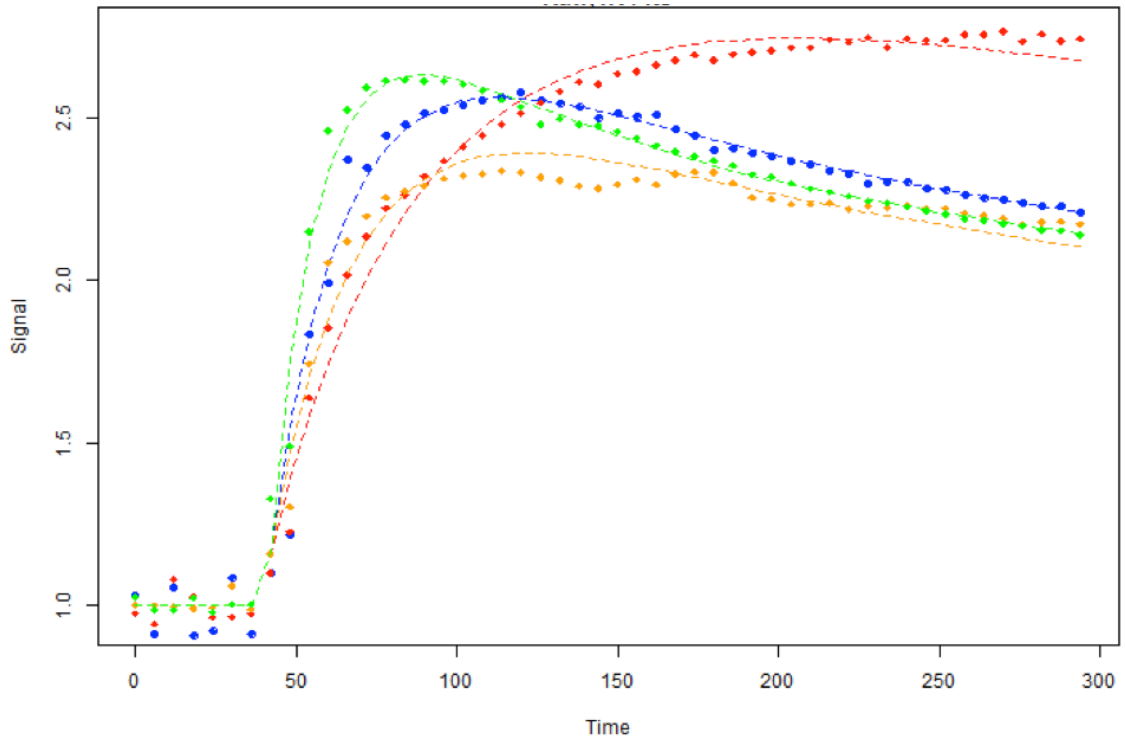

Figure 4.6. These representative DCE MRI curves from Mouse 2 at baseline (blue), 3-4 hours after treatment (red), 1 (yellow) and 5 (green) days after HIFU treatment. The y-axis is the signal intensity over the average of the pre-contrast enhanced baselines (the first six time points).

The compiled HP ^{13}C/mp-^{1}H MRI data from the 5 mice studied (Figure 4.7) quantitatively demonstrates the reproducibility of the significant loss of metabolism (HP ^{13}C lactate production) and perfusion (urea, DCE MRI and K^{trans}) at 3-4 hours after treatment in the ablated regions with no significant ($p = 0.31$) recovery by 5-6 days after treatment. In the tissues that received sub-lethal heat dose, there was a significant 60% ± 12.4% drop in HP ^{13}C lactate production and a significant 30 ± 13.7% drop in urea perfusion 3-4 hours after treatment, followed by recovery back to baseline by 5 days after treatment. DCE MRI K^{trans} and AUC showed a similar trend as the ^{13}C urea, having a complete loss of perfusion with

no recovery in the ablated region while having a 40%-50% decrease 3-4 hours after treatment followed by recovery by 5 days.

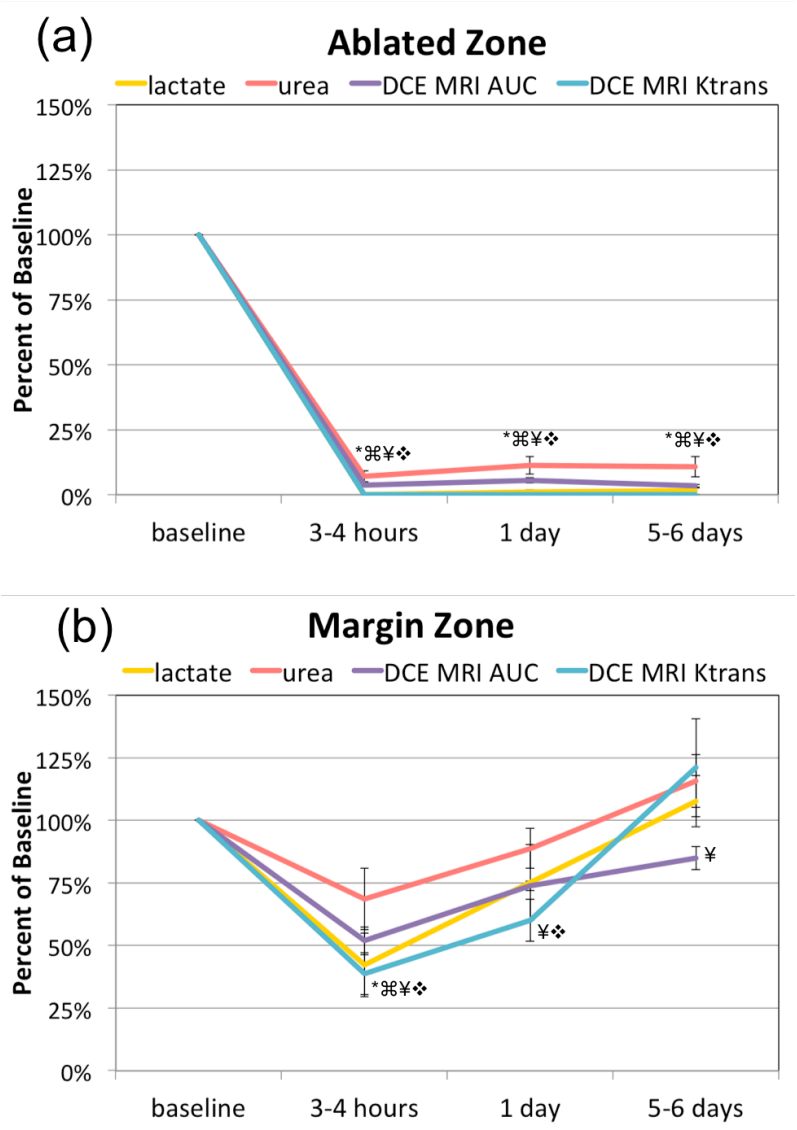

Figure 4.7. A graphical summary of the means ± stand errors change of baseline of HP ^{13}C urea, [1-^{13}C] lactate, DCE MRI AUC, and K^{trans} in the ablated (a) and margin (b) zones of the TRAMP tumor after HIFU treatment. Statistically significant changes ($p<0.05$) compared to baseline are indicated by the following symbols: * for lactate, ⌘ for urea, ¥: for DCE MRI AUC, and ❖ for K^{trans}.

The change in ADC was not significantly different from baseline versus time after HIFU treatment in either the ablated or margin regions. However, there was a trend for increasing ADC versus time in the ablated regions (% change from baseline being: -4% ± 12%, 13% ± 15%, 25% ± 17%, for 3-4 hours, 1 day and 5 days respectively). Whereas in the margin region, where there was recovery of tumor perfusion and metabolism, mean water ADC was variable with no net change by 5 days after treatment (7% ± 21%). The mean water ADC was non-significantly ($p= 0.16$) higher in the ablated (1.1×10^{-3} mm^2/sec) versus the partially treated zone (0.77×10^{-3} mm^2/sec). Additionally, tumor volume had a significant increase from baseline (a day before the treatment) to the day of the treatment (20% ± 4% increase from baseline), and then remained constant for the duration of the follow-up (21% ± 2% and 19% ± 5% for 1 and 5 days after treatment, respectively).

4.4 Discussion

The overall objective of this pre-clinical study was to develop HP ^{13}C MR biomarkers of prostate cancer ablation using HIFU, such that imaging at the time of treatment can be used to accurately predict the success and extent of coagulative ablation, and to identify tissues bordering the tumor that are potentially sensitized to adjuvant treatment (radiation, chemotherapy) by non-lethal hyperthermic heat doses. The ability to accurately predict the extent and success of HIFU ablation and tumor borders that have received sensitizing hyperthermic doses will be of vital importance in upcoming clinical trials of focal HIFU, both alone and in combination with adjuvant therapy in prostate cancer. To accomplish this goal a combined HP dual agent (^{13}C-pyruvate and ^{13}C-urea) ^{13}C MRI/mp-^{1}H MRI

approach was used for the first time to establish early serial changes (3-4 hours up to 6 days) in perfusion and metabolism that occur in regions of HIFU ablation and adjacent partial treatment zones in the well-established TRAMP model.[222, 224-226] In the ablated zone, the thermal insult was sufficient to cause complete cell death and coagulative necrosis, resulting in a complete loss of metabolism and perfusion by 3-4 hours after treatment without any recovery by 5 days. The loss of perfusion was demonstrated by a complete loss and lack of recovery of HP ^{13}C urea signal and water signal intensity on DCE MRI, and an associated loss of production in HP [1-^{13}C]lactate from HP [1-^{13}C]pyruvate. The loss of perfusion and metabolism in ablated regions were consistent across tumors of varying volume and aggressiveness and the regions of loss of perfusion spatially correlated with lost metabolism. These findings are consistent with the presence of coagulative necrosis in the ablated regions. While prior ^{1}H MRI studies have not reported on changes in tumor metabolism after HIFU, the observed loss of perfusion in HIFU ablated tumors is consistent with prior contrast enhanced ^{1}H MRI studies. The loss of contrast agent enhancement in the ablated regions after focused ultrasound treatments has been demonstrated in patients with breast cancer [237] and liver metastases.[9] It is important to note that in this study neither tumor volume nor water ADC predicted effective ablation. Similar to prior publications we observed an early non-significant decrease in ADC, and a trend towards increasing water ADC over time in the ablated region.[238] Additionally, at 5 days after treatment the ADC was higher in the ablated zone than in the partially treated zone, consistent with the literature.[239] Tumor volume changes after HIFU are confounded by the fact that only part of the tumor was ablated in this study, and there was tumor growth in the partially treated regions as described below.

In contrast to the ablated region, partially treated tissues bordering the ablated region had a significant decrease in perfusion (HP ^{13}C urea and DCE MRI) and metabolism (HP ^{13}C lactate) 3-4 hours after treatment, followed by recovery of both perfusion and metabolism back to or beyond baseline values by 5 days after treatment. As compared to the ablated regions, there was much more variability in all of the imaging data in partially treated tumor regions; most likely due to the baseline pathologic heterogeneity of TRAMP tumors and differences in the thermal doses delivered. The time course of perfusion and metabolic recovery are consistent with the delivery of a reversible sub-lethal thermal dose; with histopathology, Ki-67 and PIM staining at 5 days after treatment indicating the recovery of proliferating, predominately poorly differentiated tumor cells, and levels of hypoxia consistent with baseline high-grade TRAMP tumors prior to treatment.[222] The early reduction of HP ^{13}C lactate production with effective cancer treatment has been shown in a number of HP ^{13}C MRI publications. Specifically, a reduction in HP [1-^{13}C]lactate signals have been observed in subcutaneous murine lymphoma tumors after chemotherapy[240], in a rat glioma tumor model after radiotherapy[241], and in a murine model of human breast adenocarcinoma following doxorubicin treatment.[242] Additionally the magnitude of HP ^{13}C lactate production at 5 days post treatment is also consistent with what has been reported in the literature for highly proliferative TRAMP tumors prior to treatment. [123, 169, 243] The early reduction in HP ^{13}C urea and its relationship to increased tumor hypoxia is consistent with a prior study that reported that reduced ^{13}C-urea AUC was associated with increased hypoxia in high-versus low-grade TRAMP tumors.[36] The clinical gold standard for measuring effective HIFU is DCE MRI, and the observed decrease

in K^{trans} and DCE MRI AUC immediately after HIFU and its recovery days after treatment have repeatedly been demonstrated in other studies.[236, 238, 244] However, it is important to note that if follow-up HIFU is required to treat residual tumor after the initial DCE MRI, entrapped contrast agent within coagulated tissue regions could negatively impact the accuracy of the proton resonance frequency shift MR thermometry.[245-247] This study demonstrated that HP ^{13}C urea provides similar information about tumor perfusion after HIFU therapy as DCE MRI, however there were small differences in the magnitude of the decrease in these perfusion biomarkers as well the degree of their recovery. These differences are most likely due to the size difference between gadolinium and urea molecules, and additional studies are needed to more fully understand the mechanism of these differences. More importantly, HP ^{13}C MRI can be repeated during the HIFU treatment process without impacting the MR thermometry measurements.

The understanding of temporal perfusion and metabolic changes in the partially treated zone could be important for determining the timing of adjuvant therapies such as chemotherapy and radiation. It has been shown that reduced perfusion can negatively affect the outcome of chemotherapy since a lower concentration of anticancer drugs would be delivered to the tumor.[248] In addition, the presence of oxygen is crucial for effective radiation treatment: reactive oxygen species in tissues cause oxidative damage in DNA, proteins, and lipids, mediating the cytotoxic effect through mechanisms such as DNA strand breaks, loss of protein function, and membrane damage.[249] Therefore hypoxic tumor regions are resistant to radiotherapy due to the lack of oxygen.[250] Increased cellular proliferation is also known to modulate therapeutic response with increased cellular

proliferation being associated with more effective chemo- and radiation therapy. [251-253] Tumor hypoxia resulting from reduced perfusion and a reduction in HP [1-^{13}C]lactate production indicating reduced cellular proliferation observed in partially treated tumor tissue 3-4 hours after the HIFU treatment, both suggest that this would *not* be an optimum time for adjuvant treatment.[222, 254] The recovery of perfusion, as indicated by the urea signal and DCE MRI AUC and K^{trans}, and increased proliferation based on a high rate of HP ^{13}C lactate production, suggests that subjecting the residual prostate cancer to adjuvant treatment at 5 days after the HIFU treatment would result in a better outcome.

A limitation of this study was that MRI based temperature maps were not acquired in this study, so differences in the imaging parameters over time within the partially treated regions could not be related to thermal dose.[124, 255] An ongoing hyperthermia study is investigating the dose related changes in metabolism and perfusion in TRAMP tumors by performing real-time temperature mapping at the time of treatment. Another limitation was that the first imaging follow-up time was 3-4 hours after treatment, not immediately after treatment, since mice were allowed to physiologically recover from treatment before being exposed to the lengthy mp-^{1}H MRI/HP ^{13}C MRI acquisition under anesthesia. In ongoing hyperthermia studies, fast ^{13}C MRI (< 1sec) after injection of co-polarized ^{13}C pyruvate and ^{13}C urea is being performed right after treatment, without the longer mp-^{1}H MRI exam.

4.5 Summary

In summary, this study demonstrated that in a single imaging acquisition after injection of co-polarized [1-^{13}C]pyruvate and ^{13}C-urea that the region of HIFU induced coagulative ablation can be identified by complete loss of perfusion and metabolism. Moreover, recovery of perfusion and metabolism over time in surrounding tissues, receiving non-lethal hyperthermic heat doses, can be measured, which may be useful for discerning the best time to apply adjuvant chemo- and radiation therapy. The utility of these HP ^{13}C MR measures of perfusion and metabolism in optimizing focal HIFU, either alone or in combination with adjuvant therapy, will need be tested in future studies. The use of this HP dual agent ^{13}C MRI approach in patient HIFU studies in the near future is possible due to HP ^{13}C pyruvate MRI already being used in patient studies [169, 223], and the combined use of HP ^{13}C urea and [1-^{13}C]pyruvate imaging in patients is in progress.

Chapter 5: Compact Ultrasound Applicator for Hyperthermia Treatment of the Transgenic Adenocarcinoma Mouse Prostate Model (TRAMP) with MR Thermometry in a 14T MRI Scanner

5.1 Introduction

Focal thermal therapy is a treatment option that has the potential of improving the post-treatment quality of life of patients since it is minimally invasive and causes fewer side effects. In particular, hyperthermia and its use in conjunction with adjuvant therapies have been widely studied. Hyperthermia has been applied to rectal cancer, prostate cancer, brain tumors, pancreatic cancer, breast cancer, and more, and several studies have shown that hyperthermia combined with adjuvant therapies, such as radiation, chemotherapy, and drug delivery, yields better results than applying those therapies alone.[6, 43, 59, 256-260]

During a hyperthermia treatment, the targeted tissue is exposed to temperatures between 39°C and 45°C for about 30-60 minutes.[261-263] This increase in temperature causes changes in tissue perfusion and metabolism, potentially making the tissue more susceptible to the adjuvant therapies.[43, 59, 264] Understanding these changes in the tumor after hyperthermia is extremely useful in determining the dose and timing of the adjuvant therapies.

Magnetic resonance imaging (MRI) is one of the optimal imaging modalities suitable for guiding thermal therapy to improve targeting, achieve better control, and monitor post-treatment response. MR-guided thermal therapy has been applied to multiple clinical settings.[257, 260, 265, 266] With its superior soft tissue contrast, MRI provides high-

resolution anatomical images, aiding in the identification of malignant tissues and the aiming of the therapy devices.[212] In addition to localizing the disease, MRI is capable of assessing temperature changes in tissues noninvasively, which greatly improves the delivery of heat, especially in the case of hyperthermia where the temperature has to be maintained between a very tight range, 39°C and 45°C, for a prolonged period of time.[124, 260, 267]

Beyond the anatomical and temperature information that MRI contributes, the emerging technique hyperpolarized (HP) ^{13}C MRI can provide tumor metabolic and perfusion information noninvasively.[19] ^{13}C-labeled molecules are incorporated into metabolic pathways and behave in the same ways as the unlabeled, naturally occurring metabolites. With dynamic nuclear polarization, HP ^{13}C MR achieves a greater than 10,000-fold signal enhancement despite ^{13}C's low natural abundance, gyromagnetic ratio, and natural concentration compared to ^{1}H.[20, 21] This dramatic signal enhancement allows the monitoring of enzymatic conversions through key biochemical pathways.[19] Specifically, the conversion of HP [1-^{13}C] pyruvate to HP [1-^{13}C] lactate catalyzed by lactate dehydrogenase (LDH), represented by the conversion rate (k_{PL}) and/or the [1-^{13}C] pyruvate/[1-^{13}C] lactate ratio, has repeatedly been used to detect cancer, assess tumor aggressiveness, and monitor treatment response.[17, 19, 123, 169, 240, 243, 268, 269] With HP ^{13}C MRI, both chemical as well as spatial information is encoded, allowing simultaneous detection of metabolism ([1-^{13}C] pyruvate) and perfusion (^{13}C-urea) with a single injection of multiple ^{13}C-labeled probes.[174, 212] Metabolically inactive ^{13}C urea has been used as a perfusion contrast agent in pre-clinical studies to image blood flow.

[171, 173, 222, 270] Advantages such as direct proportionality of signal to tracer concentration, natural substance at physiologic concentrations, and inherently high contrast-to-noise ratio due to the absence of background signal make ^{13}C urea a better perfusion tracer than gadolinium-based agents.[174] The technique for co-polarizing ^{13}C-pyruvate and ^{13}C-urea has been developed, and successful simultaneous measurements of perfusion and metabolism in pre-clinical models have been demonstrated.[174, 222, 270, 271] While an increase in perfusion during and after hyperthermia has repeatedly been shown [272-274] for some *in vivo* and clinical studies, the changes are not always consistent or predictable. Further, there is currently no published data on glycolytic metabolism changes in tissues that occur shortly after hyperthermia exposure.

Correlating the temperature maps during the hyperthermia treatment to the metabolic and perfusion maps acquired with HP ^{13}C MRI after the treatment is the key to understanding the effects of hyperthermia on tumor physiology and metabolism, which is crucial information for treatment planning and development of adjuvant therapies. For accurate heat deposition and a stable steady-state temperature, a well-controlled heating system and concurrent temperature monitoring are necessary. The objective of the study is to design, fabricate, and evaluate a compact ultrasound hyperthermia device and temperature-monitoring platform compatible with the small bore of a preclinical 14T MRI scanner (Varian, Palo Alto, CA) at University of California, San Francisco. A preliminary ^{13}C MRI murine study is presented to demonstrate the feasibility of noninvasive MR imaging assessment of the metabolic and physiological changes in prostate cancer early after delivery of MR-guided ultrasound hyperthermia treatment.

5.2 Material and Methods

5.2.1 Ultrasound Hyperthermia Device Fabrication and Characterization

The housing of the hyperthermia applicator (20mm x 27mm x 7mm) was made with Mold Star 30 – platinum silicone rubber (Smooth-On) cured in in-house 3D-printed molds to create (1) the curvature on the backside to fit in the cylindrical bore of the MR coil, and (2) the rectangular chamber where the transducer was mounted, and where the cooling degassed water was circulated through (Figure 5.1a). The silicone housing provided conduits for RF power leads as well as fluid injection ports. An 8mm x 5mm gold-plated planar PZT transducer was mounted on a thin piece of hard plastic with four 1mm x 1mm x 1mm cork spacers at each corner to ensure air-backing (Figure 5.1b). The air-backed transducer was then adhered to the platform in the chamber of the applicator housing using Sil-Poxy (Smooth-On). The surface of the housing was sealed with a piece of 0.076-mm-thick silicone sheet to create a watertight chamber that allowed degassed water to flow through during the treatment. The degassed water layer ensured the acoustic coupling from the transducer to the tissue, and the active water circulation prevented the transducer from overheating, provided surface cooling to push the maximum temperature away from the skin surface, and protected the skin of the mouse from thermal damage. The distensible silicone membrane and the flexible silicone housing allowed the device to conform to the rounded abdomen of the mouse and the distended tumor mass. The hyperthermia device was designed to be compact (thickness = 7mm) to fit within the coil and mouse holder due to the space constraint of the preclinical 14T MRI scanner (bore diameter = 40mm). Figure 5.1(c) shows a picture of the actual ultrasound hyperthermia device fabricated.

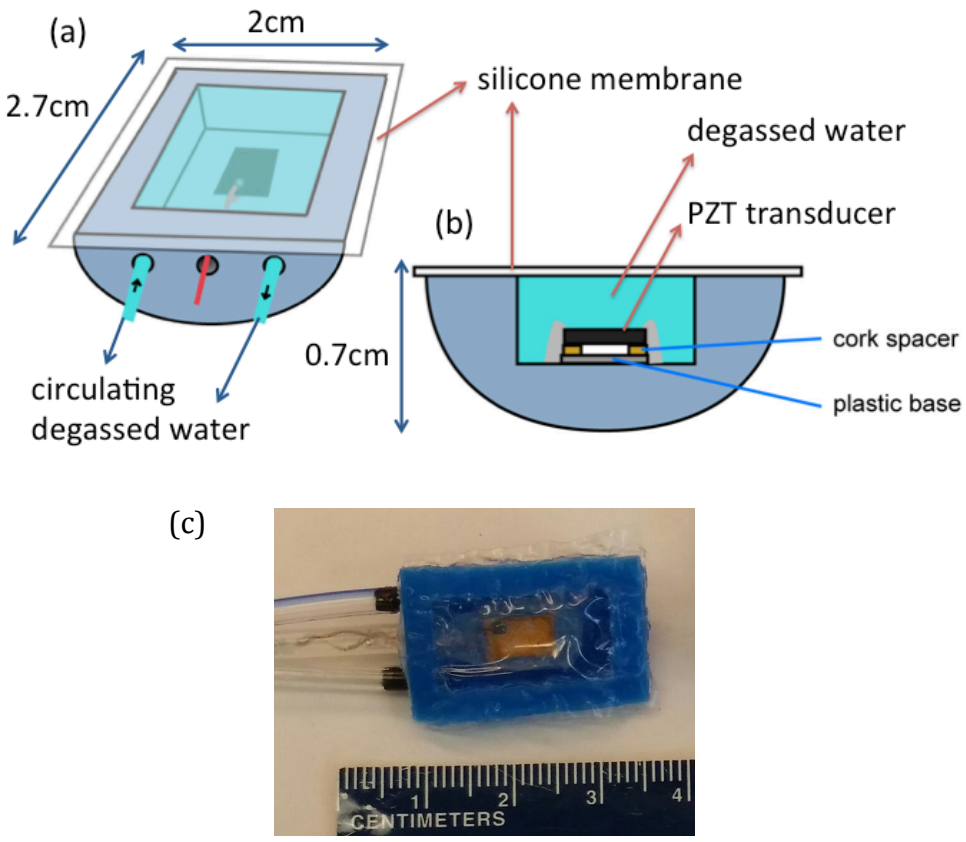

Figure 5.1. (a), (b): The compact ultrasound hyperthermia applicator design. The transducer was mounted on a plastic base with cork spacers at the corners to ensure air-backing. The plastic base was adhered to the platform of the chamber in the flexible silicone housing. A 0.076-mm-thick distensible silicone membrane sealed the silicone housing, making the chamber watertight. Degassed water was circulated through the device during the hyperthermia treatment for cooling purposes. The thickness of the entire device was only 0.7cm. (c): A photo of the actual ultrasound hyperthermia device fabricated.

The hyperthermia applicator was characterized and calibrated with intensity beam plots using a computer controlled 3D stepper-motor scanning system (Velmex Inc., Bloomfield, NY) with a calibrated hydrophone (HNP-0400, Onda Corp, Sunnyvale, CA). The applicator under test was operated in burst mode at 113 cycles with 1kHz repetition following standard beam plot measurement methods, and the peak-to-peak voltage from the

hydrophone was measured using an oscilloscope (Keysight DSO-X-2024A 200MHz Digital Oscilloscope, Keysight Technologies, Santa Rosa, CA) and converted to intensity. Maps of the distribution and the peak intensity for applied powers were measured in degassed water. Intensity beam plots of the transverse and axial planes were acquired. The step sizes were 0.2mm along either of the axes in the transverse plane, and 1mm along longitudinal axial axis. The acoustic output power as a function of electrical input power (0.5W-3.5W) was measured using the radiation force balance technique, and used to scale applied power for desired hyperthermia delivery during animal studies.

5.2.2 MR Imaging and Thermometry

The MR images were acquired with a 14T MRI scanner (Varian) with a bore diameter of 40mm. High-resolution T2-weighted anatomical images (voxel size 0.15625mm x 0.15625mm x 1mm, field of view (FOV) = 40mm x 40mm, TE = 20ms, TR = 1200ms) were acquired prior to the hyperthermia treatment in order to ensure the correct aiming of the applicator as well as the alignment of the applicator with the absorber. Once the optimal positioning was achieved, 10 slices (slice thickness = 1mm with a 0.25mm gap between two adjacent slices) from the center of the ultrasound transducer were monitored with concurrent MR thermometry during hyperthermia. A gradient-echo (GRE) sequence (voxel size 0.3125mm x 0.3125mm x 1mm, FOV = 40mm x 40mm, TE = 2.5ms, TR = 65ms) was used for proton resonance frequency (PRF)-based thermometry.[124] For the first 2 minutes, pre-treatment images were taken every 10 seconds without heating. The degassed water circulation going through the applicator was turned on at a rate of 13mL/min at the 10th pre-treatment time point, and the 11th time point was used as the

baseline for the real-time temperature monitoring during the treatment. The phase images were calculated from the real and imaginary image files. Then, the phase differences between the baseline and the subsequent time points were converted into temperatures in Matlab based on the following formula:

$$\Delta T = \frac{\varphi(t) - \varphi(t_0)}{\gamma \alpha B_0 TE}$$

where ΔT is the change in temperature from baseline, φ(t) is the phase at time point t, $\varphi(t_0)$ is the phase at baseline (before heating), ϒ is the gyromagnetic ratio, α is PRF change coefficient -0.01ppm/°C , B_0 is the magnetic field strength, and TE is the echo time.[124]

Real-time phase drift correction was implemented during the treatment. Oil phantoms were placed around the hyperthermia setup. The exact locations of the oil phantoms were identified on the baseline T2-weighted images prior to the hyperthermia treatment, and ROI's defined within the center. The mean phase of three of the oil phantoms on each slice was calculated and then subtracted from the phase of each tissue pixel on the slice prior to the conversion from phase to temperature. The baseline drift-corrected temperature maps were overlaid with the anatomical images and displayed in real-time during the treatment to visualize the heat distribution. The temperature maps were updated every 10 seconds for the first five minutes of heating, and then every 30 seconds for the next 25 minutes during steady state.

5.2.3 MR Temperature Verification in Phantom

To verify the MR thermometry and the real-time drift correction, heating was performed using the fabricated ultrasound hyperthermia applicator on a phantom mimicking tissue acoustic and thermal properties.[275] The applicator was placed on top of the phantom, aiming downwards into the phantom and an acoustic absorber, which was used to prevent reflection of the leftover ultrasound energy (Figure 5.2). The degassed water-filled absorber had the same design as the housing of the applicator without a mounted transducer. Three calibrated fiber optic temperature sensors (IPITEK©) were inserted into the phantom at different locations. Four oil phantoms were placed around the tissue-mimicking phantom and applicator for phase drift monitoring and correction.[187, 188] 2 minutes of baseline images were acquired prior to the heating. RF power was applied continuous wave using a single channel from a four-channel amplifier (Advanced Surgical Systems, Inc.; 500-009 RF generator). The power was passed through a low-pass filter (Bencher, Inc., Model YA-1) and an isolation transformer to minimize the noise and artifacts from the electronics. The ultrasound hyperthermia was performed at 10MHz with 0.6-1.1W net electrical input power for 30 minutes with a closed-loop degassed water circulatory cooling system. The water pump (Cole-Parmer Instrument Company MasterFlex® Console Drive) circulated the degassed water through the silicone tubings (2mm inner diameter) at 13mL/min. Cooling was monitored for 15 minutes after the treatment. After the treatment, MR temperatures with and without the drift correction were compared to the measurements of the fiber optic temperature sensors.

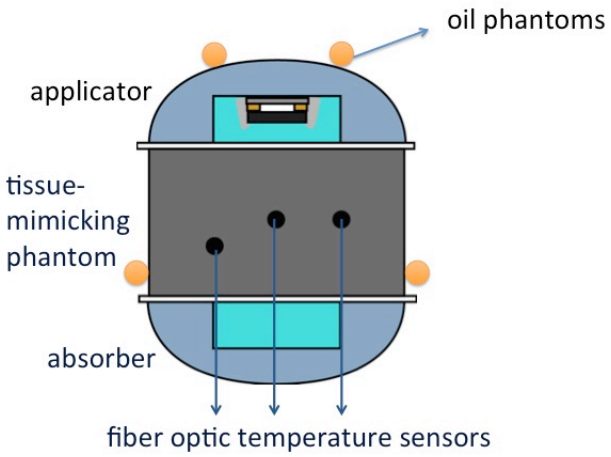

Figure 5.2. The setup of the phantom experiment for MR thermometry and phase drift correction verification. The ultrasound hyperthermia applicator was placed on top of the tissue-mimicking phantom, aiming downwards through the phantom into the acoustic absorber. Four oil phantoms were placed around the phantom and the ultrasound applicator for phase drift monitoring. Three calibrated fiber optic temperature sensors were inserted into the tissue-mimicking phantom to measure the absolute temperature at different locations in the phantom. An acoustic absorber filled with degassed water was placed under the phantom to absorb and dissipate the leftover ultrasound energy. Acoustic gel was applied at the interfaces between the applicator and the phantom, and between the phantom and the absorber.

5.2.4 Murine Tumor Model

The transgenic adenocarcinoma of mouse prostate (TRAMP) model is a well-established murine prostate model that closely mimics the progression as well as the perfusion and metabolism of human prostate cancer.[222, 224-226] Mice of C57Bl6 X FVB background (n=6), weighing 30-40g with solid prostate tumors of 0.58-3.25 cm^3 were selected for hyperthermia treatments. The tumor dimensions were determined based on the T2-weighted anatomical MRI images. A pressure sensor (SA Instruments, NY, USA) for respiration monitoring was placed under the animal, positioned within the mouse holder and the custom RF coil specific to mouse studies and the 14T MRI scanner. During the

hyperthermia treatment and the MRI session, mice were anesthetized with 1%-2% isoflurane while maintaining the respiration rate at 60-75 breaths/minute.

5.2.5 Mouse Hyperthermia Treatment

A total of 6 mice were treated with hyperthermia in the 14T MRI scanner. The mice were depilated using Nair™ on the ventral and dorsal abdominal regions for efficient acoustic energy coupling at both the ultrasound beam entrance and exit sites. For each hyperthermia treatment, the mouse was in the supine position in the MRI scanner, and the applicator was compressed and secured onto the depilated ventral side of the abdomen of the mouse, aiming from ventral to dorsal through the tumor (Figure 5.3). The positioning was verified with the T2-weighted anatomical MR images to ensure that the spine of the mouse was not in the ultrasound beam path in order to prevent reflection and preferential heating hear the spine. Degassed water was circulated through the device during the treatment at 13mL/min for cooling purposes. On the dorsal side of the animal, the absorber was placed to absorb the leftover ultrasound energy and prevent reflection back into the target region. The hyperthermia applicator was coupled to the ventral side of the mouse and the absorber was coupled to the dorsal side of the mouse using ultrasound transmission gel. A rectal probe was inserted into the rectum of the mouse to measure the basal temperature in order to accurately quantify the background or starting temperature prior to start of the treatment and power adjustment to reach the desired hyperthermic range. Once a steady basal starting temperature was acquired, the rectal probe was removed to avoid imaging artifacts during the MRI sessions. A consensus on the optimal temperature range for hyperthermia has not been agreed upon in the field, but to prevent

heat-induced damage and morphological changes in tumor vessels and decrease in blood flow caused by congestion and embolism, a temperature range between 39°C and 42°C was chosen for this study.[49, 276] Four to five olive oil phantoms were placed around the mouse for phase drift correction. The hyperthermia treatments were performed in a 14T MRI scanner (Varian, Palo Alto, CA) as previously described. Each treatment was 30 minutes of ultrasound heating at 10MHz with net output acoustic power ranging from 0.60-1.81W (Table 5.1). The power was constantly adjusted manually during heating in order to maintain the temperature in the targeted tumor area to be within 39°C and 42°C based on the visual feedback of the overlaid temperature images from the MR thermometry. For these preliminary experiments, a closed-loop control was not integrated within the system. The goal was to achieve only partial hyperthermia treatment of the tumor and to leave the remaining tumor tissue nominally untreated for comparison. Table 5.1 summarizes the treatment input power ranges for mice of various tumor sizes and basal pre-treatment temperatures.

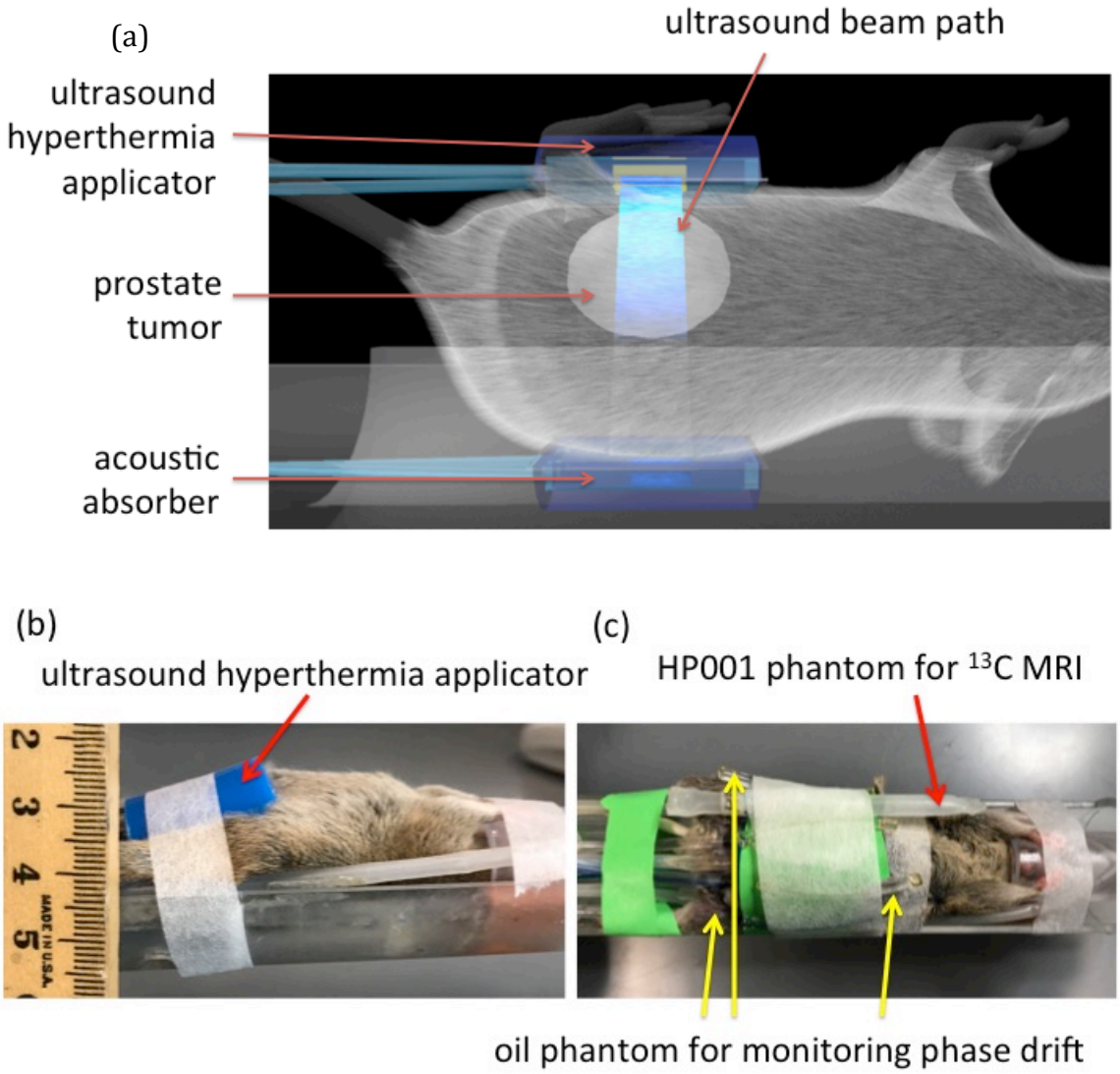

Figure 5.3. (a) Diagram showing the setup used for hyperthermia treatment of a TRAMP tumor. The silicone housing of the ultrasound hyperthermia applicator was filled with circulating degassed water to cool the transducer and prevent thermal damage of the skin of the mouse. The ultrasound hyperthermia applicator aimed from ventral to dorsal through the solid tumor. On the dorsal side, an acoustic absorber filled with degassed water was aligned with the applicator to absorb and dissipate the leftover ultrasound energy and prevent reflections. Acoustic gel was applied at the interfaces between the mouse and the hyperthermia applicator, and between the mouse and the acoustic absorber. (b) The side view and (c) top-down view of the setup on a mouse during a hyperthermia treatment.

Mouse #	Tumor Volume (cm^3)	Mouse Basal Temperature (°C)	Acoustic Power (W)	Volume heated to 39-42°C (mm^3)	Maximum temperature during steady state (°C)
1	1.95	34.0	0.60-1.16	122.8	43.6
2	1.51	32.7	0.95-1.51	114.4	40.7
3	1.01	33.0	1.03-1.81	68.5	40
4	1.95	33.5	0.95-1.59	53.7	40.5
5	0.58	33.4	0.82-0.95	72.0	42.1
6	3.25	34.0	0.82-1.03	169.0	39.4

Table 5.1 Summary of the tumor volumes, mouse basal temperatures before treatments, acoustic input powers, volumes heated to the hyperthermic temperature range (39°C-42°C), and the maximum temperatures reached during steady state of the six mice treated with hyperthermia.

5.2.6 Initial Hyperthermia Treatment Study with Hyperpolarized ^{13}C MRI Monitoring

An initial hyperthermia treatment study with hyperpolarized ^{13}C MRI monitoring was performed on a large late stage TRAMP mouse tumor on the 14T MRI scanner. The ^{13}C-labeled pyruvate and urea samples and the buffer solution were prepared following the previously published protocols.[171] The co-polarizations of ^{13}C-labeled pyruvate and urea were done in HyperSense DNP Polariser (Oxford Instruments plc). A catheter was placed in the tail vein of the mouse prior to the imaging session. Baseline T2-weighted anatomical images and the HP ^{13}C MRI were acquired right before the placement of the hyperthermia device. The treatment setup and the 30-minute hyperthermia treatment were described in the previous section. Immediately after the treatment, the applicator was removed, and the post-treatment T2-weighted images and the HP ^{13}C imaging of co-polarized ^{13}C-labeled pyruvate and urea were acquired (15 minutes post-treatment). The co-polarized ^{13}C-labeled pyruvate and urea probes in 450μL of the dissolution solution (buffer mixed with

the HP ^{13}C-labeled metabolites) were injected through a tail vein catheter over a period of 15 seconds. HP 3D GRASE ^{13}C MRI was initiated at 35 seconds after the injection. A 2-degree flip angle spectrum of an imaging slab through the tumor was acquired immediately before the 3D GRASE sequence, and a 90-degree flip angle spectrum was acquired at the end of the acquisition. These spectra were used for verification of a successful injection, sufficient polarization levels, metabolite frequencies used in the 3D GRASE acquisition, and for data normalization.

5.2.7 Data Analysis

Thermometry Data

Regions of interest (ROIs) were identified in Matlab on the magnitude images from the GRE sequence. The exact same voxels were registered to the drift-corrected temperature maps, and the mean of the temperatures of all the voxels within each ROI was calculated at every time point. A graph of the temperature over time was generated for each ROI to visualize the temperatures that the region of tissue was exposed to during the course of the treatment.

HP ^{13}C MRI Data

The lactate-to-pyruvate ratio was calculated for each voxel. The urea images were normalized to the area of the urea peak on the 2-degree spectrum acquired immediately before the 3D GRASE acquisition. Only voxels with signal-to-noise ratios larger than 3 were considered. Based on the overlaid images of the drift-corrected temperature maps on the magnitude anatomical images from the GRE sequence, the regions that received a

hyperthermic heat dose were identified on the pre- and post-treatment T2-weighted images. These regions were registered to the HP ^{13}C images using custom software developed in-house programmed in IDL Software. The means of the lactate-to-pyruvate ratios and the normalized HP ^{13}C urea in the heated regions were calculated.

5.3 Results

5.3.1 Ultrasound Hyperthermia Applicator

Figure 5.4 shows the intensity beam plot of the transverse cross section of the planar ultrasound hyperthermia applicator beam pattern measured 3mm from the silicone membrane on the surface of the applicator. The 25% intensity contour approximately encompasses a 3mm x 4.5mm area. As measured by the radiation force balance, the acoustic efficiency (ratio of acoustic power output to applied electrical power) of the hyperthermia applicator was 43%. The required applied power levels to raise and maintain the temperature to the desired hyperthermia temperature range in the animal experiments were determined based on the power calibration measurements using this measured efficiency as well as the basal temperature of each animal and the visual feedback of the temperature maps during treatments.

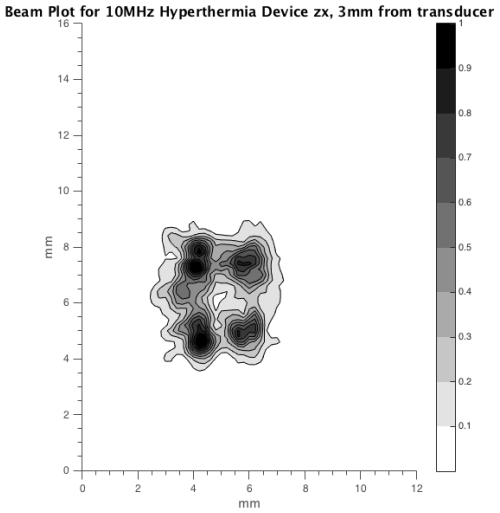

Figure 5.4. The transverse cross section of the normalized intensity beam plot of the ultrasound hyperthermia device mapped out with a hydrophone in degassed water measured 3mm from the surface of the applicator.

5.3.2 MR Temperature Verification in Phantom

The hyperthermia treatment resulted in an increase of 6-7°C in the phantom. Figure 5.5a shows the average phase drift from four oil phantoms on the slice where the tips of the fiber optic sensors were. An average of -1°C to -1.5°C drift in the oil phantoms was observed during the experiment. Figure 5.5b shows temperature measurements from one representative fiber optic sensor along with the PRF-based MR temperature measurements with and without the phase drift correction at where the tip of the fiber optic sensor was located in the phantom. The comparisons between the temperature measurements from the fiber optic sensor and the PRF-based MR thermometry (with and without the phase drift correction) were only made during cooling (the last 15 minutes of the experiment) after the ultrasound power was turned off to avoid inaccuracies due to the preferential acoustic absorption or interactions of the ultrasound with the plastic casing on the tips of the fiber optic sensors. As shown in Figure 5.5b, with the phase drift correction, the

temperatures based on the PRF-based MR thermometry agreed closely with the fiber optics temperature measurements.

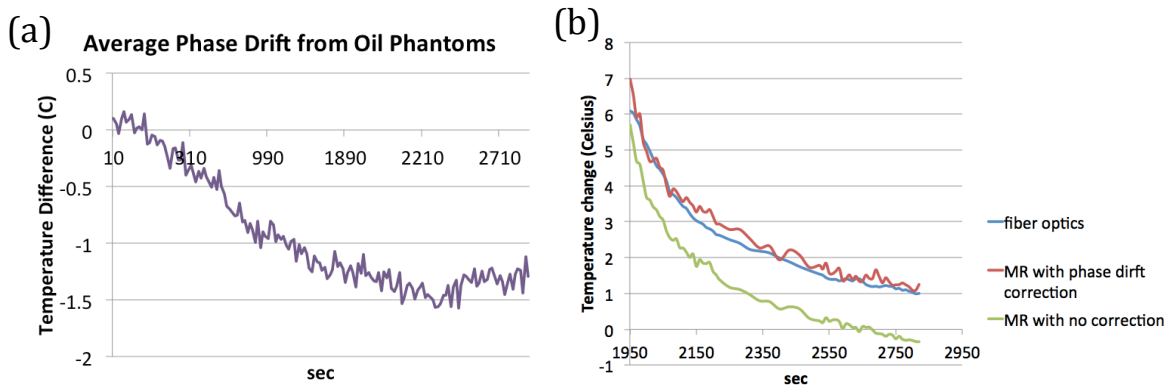

Figure 5.5. (a) The average phase drift from the four oil phantoms around the tissue-mimicking phantom and the ultrasound applicator. (b) The MR temperature results with and without phase drift correction, and the measurements from the fiber optic temperature sensors during the 15 minutes of cooling after 30 minutes of heating.

5.3.3 Murine Hyperthermia Studies

Figure 5.6a is a series of anatomical images of the same axial cross section overlaid with the temperature maps at different time points during the hyperthermia treatment of a mouse bearing a 1.95-cm^3 solid prostate tumor with a baseline temperature of 34°C. 10-20 seconds after the power was turned on, the temperature of the targeted tumor tissue within the ultrasound beam path increased quickly to over 39°C and was maintained between 39°C and 42°C during steady state (last 22 minutes of heating). A total of 122.8mm^3 of the tumor tissue was maintained at the hyperthermic temperature range (39°C-42°C) during the 22-minute of steady state heating, spanning across 4 axial slices (total thickness = 5mm) with a maximum depth and width of 0.76cm x 0.45cm.

Figure 5.6b presents the average temperature in different regions of interest. In the region within the beam path (Figure 5.6b, red), the temperature was raised rapidly to above 39°C with only 6.5 minutes of heating. The temperature in this region was maintained between 39°C and 42°C throughout the rest of the treatment. The temperature was easily and precisely controlled by adjusting the input acoustic power level and/or the flow rate of the cooling degassed water, as demonstrated at 850 seconds: decreasing the input power and increasing the flow rate successfully lowered the temperature to 40°C. In an untreated region away from the targeted region of hyperthermic treatment (Figure 5.6b, blue), no significant temperature elevation was observed. The contrast between the profiles of the two regions demonstrates the capability of achieving local hyperthermia treatment in a murine tumor.

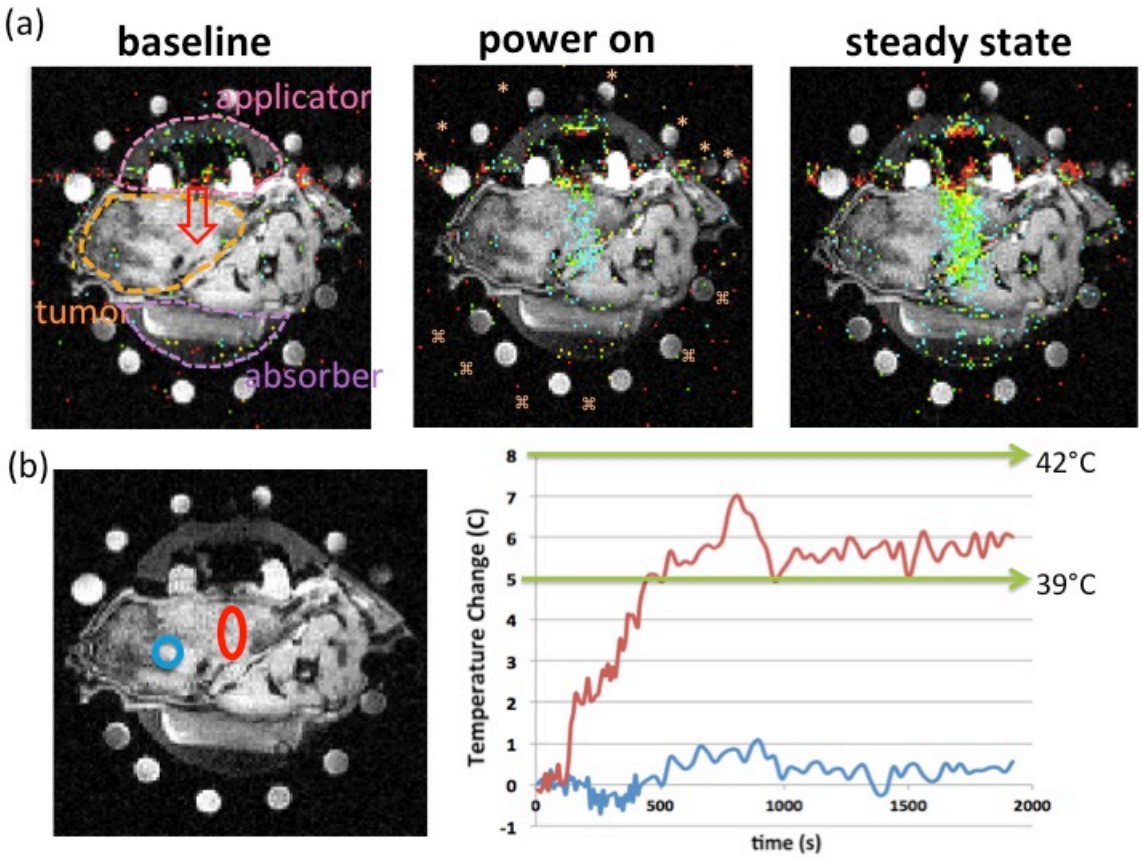

Figure 5.6. (a) Temperature maps overlaid on the anatomical images of hyperthermia in a mouse bearing a 1.95cm^3 solid prostate tumor. The applicator was placed on the ventral side of the mouse, aiming into the tumor and aligning with the absorber on the dorsal side of the animal. The red arrow on the baseline image indicates the direction of the ultrasound beam path. Blue: 39-40°C. Green: 40-42°C. Yellow: 42-45°C. Red: > 45°C. *: oil phantoms for monitoring phase drift. ★: HP001 phantom for HP ^{13}C MRI studies. ⌘: water tubing with circulating heated water for keeping the mouse warm. (b) Temperature profiles during the hyperthermia treatment in a mouse. The basal temperature of the mouse was 34°C. The red region was the targeted tumor tissue within the ultrasound beam path where hyperthermic temperature range was maintained during the steady state. The blue region was tumor tissue away from the ultrasound beam path where minimal temperature change was observed.

Figure 5.7 shows another representative case of hyperthermia treatment in a mouse bearing a much smaller 0.58cm^3 prostate tumor. The applicator on the ventral side of the animal targeted at the tumor using an angle that avoided heating the spine and the urethra (Figure 5.7a). As in the prior case, only a small portion of the tumor (72mm^3) was heated, spanning across six axial slices (a total of 7.5mm thick) with a maximum depth and width of 0.61cm x 0.36cm on the central heated slice. Figure 5.7b shows the temperature profiles of two regions of interest, both within the ultrasound treatment path. The region on the ventral portion of the tumor (red, closer to the ultrasound transducer) had a steeper increase in temperature during the first minute of heating and was maintained close to but not exceeding 42°C. The region on the dorsal end of the tumor (green, further away from the ultrasound transducer) reached 39°C 30 seconds later than the region closer to the transducer and was maintained at close to 39.5°C throughout the rest of the treatment. The temperature map also demonstrates that the applicator was capable of performing volumetric hyperthermia treatment without overheating and damaging the skin of the mouse.

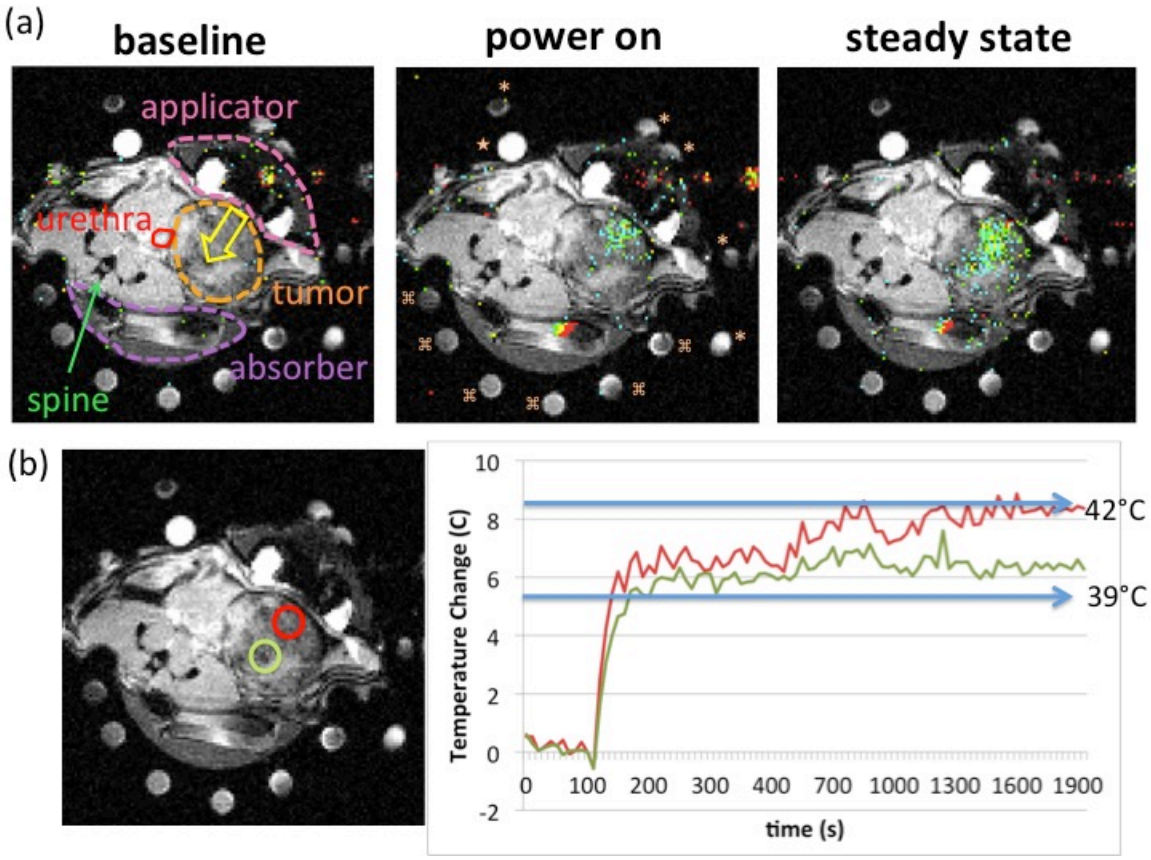

Figure 5.7. (a) Temperature maps overlaid on the anatomical images of hyperthermia in a mouse bearing a 0.58cm^3 solid prostate tumor. The applicator was placed on the ventral side of the mouse, aiming into the tumor and aligning with the absorber on the dorsal side of the animal. The yellow arrow on the baseline image indicates the direction of the ultrasound beam path. Blue: 39-40°C. Green: 40-42°C. Yellow: 42-45°C. Red: > 45°C. *: oil phantoms for monitoring phase drift. ★: HP001 phantom for HP ^{13}C MRI studies. ⌘: water tubing with circulating heated water for keeping the mouse warm. (b) Temperature profiles during the hyperthermia treatment in a mouse. The basal temperature of the mouse was 33.5°C. The red region was the targeted tumor tissue within the ultrasound beam path on the ventral side of the tumor closer to the ultrasound transducer. The green region was the targeted tumor tissue within the ultrasound beam path on the dorsal side of the tumor further away from the ultrasound transducer.

5.3.4 Results: Hyperpolarized ^{13}C MR Monitoring of Hyperthermia Treatment

Figure 5.8 shows initial data from a mouse with a 3.25cm^3 solid prostate tumor with a small focal area within the tumor treated with 30 minutes of hyperthermia. The pink dotted line on the central axial slice of the treated region indicates the hyperthermia targeted tumor region. Figure 5.8a demonstrates that local hyperthermia was achieved successfully with the treated region being maintained in the hyperthermic temperature range (39°C to 42°C) during the last 22 minutes of steady state heating, while regions outside of the ultrasound beam path did not demonstrate a significant temperature increase. Minor reflection occurred at the interface between the mouse and the absorber on the dorsal side (Figure 5.8a, yellow rectangle), but no thermal damage was observed on the skin of the mouse. Figure 5.8b shows that metabolism (lactate-to-pyruvate ratio) and perfusion (urea) MR imaging results pre- and post-treatment. There was a 12% decrease in the lactate-to-pyruvate ratio and a 9% increase in urea signal in the heated region 15 minutes after the hyperthermia treatment relative to the region prior to treatment.

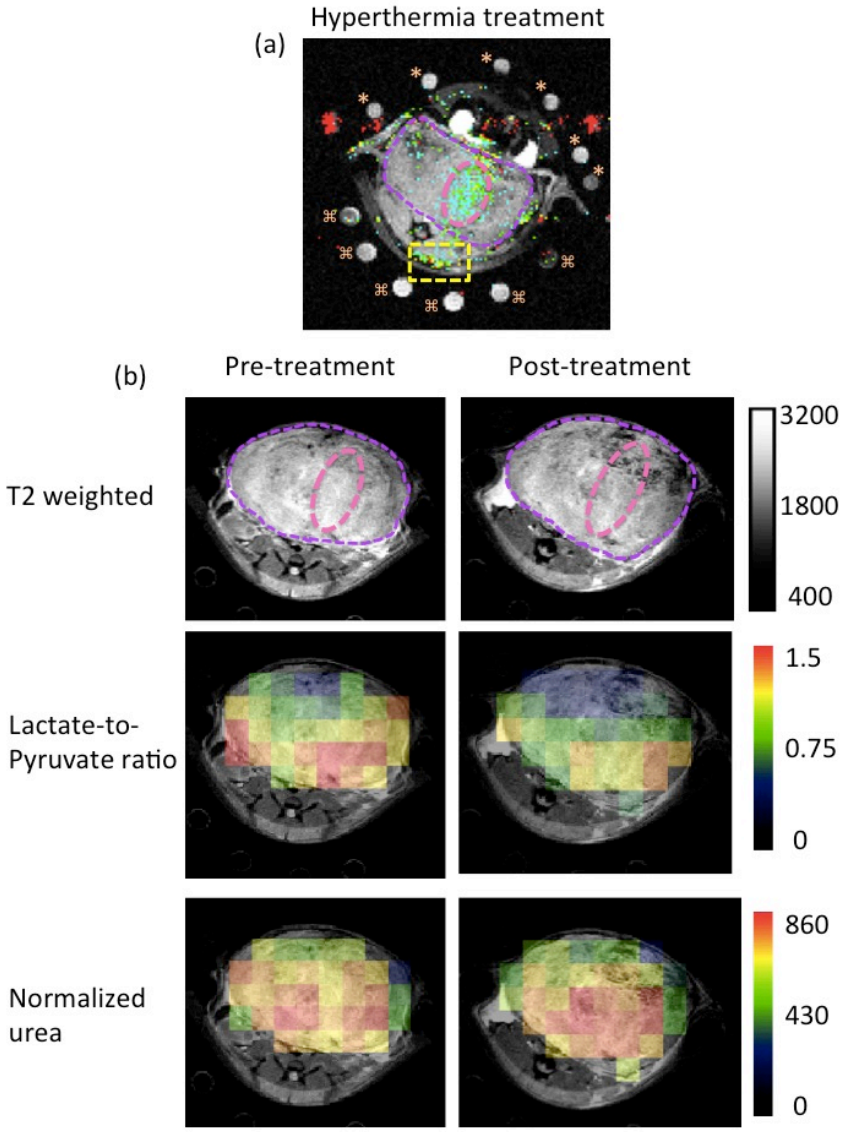

Figure 5.8. The preliminary ^{13}C MRI data of a mouse treated with 30 minutes of hyperthermia. The pink dotted line outlines the tissue receiving hyperthermia temperature during the steady state. The TRAMP tumor is demarcated by the dashed purple line. (a) The anatomical axial image of the center of the heated tumor tissue overlaid with a temperature map acquired during the steady state. Minor reflection between the dorsal side of the mouse and the absorber (yellow rectangle) was observed. Blue: 39-40°C. Green: 40-42°C. Yellow: 42-45°C. Red: > 45°C. *: oil phantoms for monitoring phase drift. ⌘: water tubing with circulating heated water for keeping the mouse warm. (b) The corresponding T2 weighted anatomical images as well as overlaid lactate-to-pyruvate ratio and HP ^{13}C urea images on the T2 weighted images of the central heated tumor slice.

5.4 Discussion

In this study, we demonstrated that an MR-compatible compact small animal ultrasound hyperthermia applicator capable of performing focal hyperthermia in murine models in an ultra high field 14T preclinical MRI scanner with concurrent MR thermometry feedback was feasible. In the six mice with TRAMP tumors of varying sizes and locations, reproducible hyperthermic heat doses were delivered to focal regions within the tumor with the ultrasound beam directed away from the surrounding critical structures (bone, bladder, seminal vesicles, urethra, etc.). The current commercially available small-animal MR-guided high intensity focused ultrasound (MRgHIFU) and MR-guided focused ultrasound (MRgFUS) systems are designed for much larger bore (>15.4cm) magnets that operate at lower magnetic field strengths (3T, 4.7T, or 7T) than the much narrower bore 14T system (4cm) used in these studies.[8, 119-122, 277] The high ultrasound frequency (10MHz) utilized in these studies was selected for increased ultrasound energy absorption in the targeted tumor tissue, thereby preventing excessive ultrasound penetration and reflection on the dorsal side of the animal, as the prostate tumors studied had a low ultrasound attenuation. The ultrasound applicator had sufficient cooling water flow rates and sufficient temperature control to eliminate thermal damage to the skin of the mice treated. The compact hyperthermia applicator fabricated in this project was also very thin (0.7cm), allowing for hyperthermia treatments on mice within the narrow 14T MRI scanner bore to be performed using an acoustic absorber, anesthesia delivery system, respiration sensor, and warm water lines for maintaining the core body temperature of the mice.

PRF-based MR thermometry with real-time phase drift correction was validated with fiber optic temperature sensors in a phantom that mimics the acoustic properties of tissues. Phase drift correction was necessary for the MR system utilized since a drift of 0.8°C to 1.2°C was observed in a phantom monitored for 30 minutes with no heating, and an average drift of 1.5°C was observed during a 30-minute hyperthermia treatment in a tissue mimicking phantom. The phase drift correction minimizes errors between the fiber optic measurements and the MR thermometry to less than 0.5°C and over similar 30-minute time frame of hyperthermia sessions. Minimal imaging artifacts from the ultrasound transducer were observed during experiments. The degassed water circulating through the applicator did cause flow artifacts reflected in both the T2-weighted anatomical images and the temperature maps, but the artifacts was present only in the regions outside of the mice thus did not interfere with the thermal monitoring in the regions of interest within the tumors.

The initial HP ^{13}C MRI study performed pre- and post-hyperthermia treatment demonstrated the feasibility of examining the immediate changes in both metabolism (lactate-to-pyruvate ratio) and perfusion (urea) early after exposure to hyperthermic temperatures. The understanding of the immediate tissue response to hyperthermia is crucial in order to optimize treatment efficacy, as hyperthermia is mainly applied as an adjunct therapy to radiation and/or chemotherapy.[13, 53-56, 60-63] An increase in perfusion results in higher oxygenation and lower hypoxia, thereby improves the effectiveness of radiation treatment.[52] A higher perfusion also allows for better delivery of the anticancer drugs to the targeted region, leading to efficient chemotherapy.[45, 57]

The enhancement in vascular permeability is also a known effect of hyperthermia, which can promote drug penetration and delivery.[278-280] In addition, increased cellular proliferation is associated with more effective chemo- and radiation therapy.[251-253] While perfusion changes in tissue due to hyperthermia has been reported, the immediate effects of hyperthermia on tissue metabolism is still unknown.[272-274] The technique of HP ^{13}C MRI, as demonstrated in this study, opens the door to noninvasive assessments of both perfusion and metabolism, which can greatly aid in the determination of the timing and dose of the adjuvant radiation and/or chemotherapy. More HP ^{13}C MRI experiments following hyperthermia treatments in TRAMP mice are currently being conducted in order to quantify and determine the significance of the metabolic and perfusion changes of the prostate tumors immediately after hyperthermia.

To achieve different heating patterns or treatment goals, different design factors can be adjusted for future experiments: (1) Higher frequency ultrasound transducers can be used to increase the attenuation in the tissue to further prevent energy penetration beyond the tumors, (2) larger ultrasound transducers or possibly phased arrays or multi-transducer systems can be used to deliver heat to a larger volume of tumor tissues and focus in the tumor at depth, and (3) automated control over the electrical input power based on the thermometry feedback can be implemented to maintain a more stable temperature during the steady state.

5.5 Summary

In summary, an MR-compatible compact ultrasound hyperthermia applicator capable of volumetric heating in murine tumors at a 14T MRI scanner with a 4cm bore has been fabricated and shown feasible for MR-guided hyperthermia delivery in a small-bore preclinical 14T system. Concurrent MR PRF-based thermometry has been implemented for accurate temperature monitoring and control. This study also demonstrated the feasibility of using the HP dual agent ^{13}C MRI approach to study the tissue metabolic and perfusion responses to hyperthermia treatments. Ongoing *in vivo* murine experiments with HP ^{13}C MRI post-hyperthermia follow-ups will be used to understand the significance of the metabolic and perfusion changes in tumor tissues in relation to the efficacy of adjuvant radiation and chemotherapy.

Reference

1. *Cancer Facts & Figures 2017*, 2017, American Cancer Society: Atlanta.
2. Chan, J.M., R.M. Jou, and P.R. Carroll, *The relative impact and future burden of prostate cancer in the United States.* J Urol, 2004. **172**(5 Pt 2): p. S13-6; discussion S17.
3. Chin, J.L., et al., *Magnetic Resonance Imaging-Guided Transurethral Ultrasound Ablation of Prostate Tissue in Patients with Localized Prostate Cancer: A Prospective Phase 1 Clinical Trial.* Eur Urol, 2016. **70**(3): p. 447-55.
4. Marien, A., et al., *Target ablation--image-guided therapy in prostate cancer.* Urol Oncol, 2014. **32**(6): p. 912-23.
5. Ramsay, E., et al., *Evaluation of Focal Ablation of Magnetic Resonance Imaging Defined Prostate Cancer Using Magnetic Resonance Imaging Controlled Transurethral Ultrasound Therapy with Prostatectomy as the Reference Standard.* J Urol, 2017. **197**(1): p. 255-261.
6. Salgaonkar, V.A., et al., *Thermal Dosimetry Analysis Combined with Patient-specific Thermal Modeling of Clinical Interstitial Ultrasound Hyperthermia Integrated within HDR Brachytherapy for Treatment of Locally Advanced Prostate Cancer.* Proceedings from the 14th International Symposium on Therapeutic Ultrasound, 2017. **1821**.
7. Ghai, S., et al., *Real-Time MRI-Guided Focused Ultrasound for Focal Therapy of Locally Confined Low-Risk Prostate Cancer: Feasibility and Preliminary Outcomes.* AJR Am J Roentgenol, 2015. **205**(2): p. W177-84.
8. Frazier, N., et al., *High intensity focused ultrasound hyperthermia for enhanced macromolecular delivery.* J Control Release, 2016. **241**: p. 186-193.
9. Kennedy, J.E., *High-intensity focused ultrasound in the treatment of solid tumours.* Nat Rev Cancer, 2005. **5**(4): p. 321-7.
10. Dickson, J.A. and S.K. Calderwood, *Temperature range and selective sensitivity of tumors to hyperthermia: a critical review.* Ann N Y Acad Sci, 1980. **335**: p. 180-205.
11. Hurwitz, M. and P. Stauffer, *Hyperthermia, radiation and chemotherapy: the role of heat in multidisciplinary cancer care.* Semin Oncol, 2014. **41**(6): p. 714-29.
12. Hurwitz, M., et al., *Response of blood flow to hyperthermia in human prostate tumors: Opportunities for enhanced radiation effect and drug delivery.* Journal of Clinical Oncology, 2014. **32**(4).
13. Datta, N.R., et al., *Local hyperthermia combined with radiotherapy and-/or chemotherapy: recent advances and promises for the future.* Cancer Treat Rev, 2015. **41**(9): p. 742-53.
14. Kaur, P., et al., *Combined hyperthermia and radiotherapy for the treatment of cancer.* Cancers (Basel), 2011. **3**(4): p. 3799-823.
15. Ellis, S., et al., *Clinical applications for magnetic resonance guided high intensity focused ultrasound (MRgHIFU): present and future.* J Med Imaging Radiat Oncol, 2013. **57**(4): p. 391-9.
16. Ramsay, E., et al., *MR thermometry in the human prostate gland at 3.0T for transurethral ultrasound therapy.* J Magn Reson Imaging, 2013. **38**(6): p. 1564-71.

17. Chen, A.P., et al., *Hyperpolarized C-13 spectroscopic imaging of the TRAMP mouse at 3T-initial experience.* Magn Reson Med, 2007. **58**(6): p. 1099-106.
18. Zhang, V., *Monitoring tumor response of prostate cancer to radiation therapy by multi-parametric 1H and hyperpolarized 13C magnetic resonance imaging*, 2014, [Order No. 3642693]. University of California, San Francisco.
19. Kurhanewicz, J., et al., *Analysis of cancer metabolism by imaging hyperpolarized nuclei: prospects for translation to clinical research.* Neoplasia, 2011. **13**(2): p. 81-97.
20. Ardenkjaer-Larsen, J.H., et al., *Increase in signal-to-noise ratio of > 10,000 times in liquid-state NMR.* Proc Natl Acad Sci U S A, 2003. **100**(18): p. 10158-63.
21. Keshari, K.R. and D.M. Wilson, *Chemistry and biochemistry of 13C hyperpolarized magnetic resonance using dynamic nuclear polarization.* Chem Soc Rev, 2014. **43**(5): p. 1627-59.
22. Muller, B.G., et al., *The role of magnetic resonance imaging (MRI) in focal therapy for prostate cancer: recommendations from a consensus panel.* BJU Int, 2014. **113**(2): p. 218-27.
23. Chu, K.F. and D.E. Dupuy, *Thermal ablation of tumours: biological mechanisms and advances in therapy.* Nat Rev Cancer, 2014. **14**(3): p. 199-208.
24. Diederich, C.J., *Thermal ablation and high-temperature thermal therapy: overview of technology and clinical implementation.* Int J Hyperthermia, 2005. **21**(8): p. 745-53.
25. Boyes, A., et al., *Prostate tissue analysis immediately following magnetic resonance imaging guided transurethral ultrasound thermal therapy.* J Urol, 2007. **178**(3 Pt 1): p. 1080-5.
26. Coad, J.E., *Practical Pathology Perspectives for Minimally Invasive Hyperthermic Medical Devices.* Energy-Based Treatment of Tissue and Assessment Vi, 2011. **7901**.
27. Coad, J.E. *Thermal fixation: a central outcome of hyperthermic therapies*. in *SPIE*. 2005. Bellingham, WA.
28. Coad, J.E. and J.C. Bischof, *Histologic differences between cryothermic and hyperthermic therapies.* Thermal Treatment of Tissue: Energy Delivery and Assessment Ii, 2003. **4954**: p. 27-36.
29. Cheng, M., M. Fay, and K. Steinke, *Percutaneous CT-guided thermal ablation as salvage therapy for recurrent non-small cell lung cancer after external beam radiotherapy: A retrospective study.* Int J Hyperthermia, 2016. **32**(3): p. 316-23.
30. Chinnaratha, M.A., et al., *Percutaneous thermal ablation for primary hepatocellular carcinoma: A systematic review and meta-analysis.* J Gastroenterol Hepatol, 2016. **31**(2): p. 294-301.
31. Crouzet, S., et al., *Salvage high-intensity focused ultrasound (HIFU) for locally recurrent prostate cancer after failed radiation therapy: Multi-institutional analysis of 418 patients.* BJU Int, 2017. **119**(6): p. 896-904.
32. Lencioni, R., et al., *Image-Guided Ablation of Malignant Liver Tumors: Recommendations for Clinical Validation of Novel Thermal and Non-Thermal Technologies - A Western Perspective.* Liver Cancer, 2015. **4**(4): p. 208-14.
33. Regier, M. and F. Chun, *Thermal Ablation of Renal Tumors: Indications, Techniques and Results.* Dtsch Arztebl Int, 2015. **112**(24): p. 412-8.
34. Horkan, C., et al., *Reduced tumor growth with combined radiofrequency ablation and radiation therapy in a rat breast tumor model.* Radiology, 2005. **235**(1): p. 81-8.

35. Solazzo, S., et al., *RF ablation with adjuvant therapy: comparison of external beam radiation and liposomal doxorubicin on ablation efficacy in an animal tumor model.* Int J Hyperthermia, 2008. **24**(7): p. 560-7.
36. Deng, Z., et al., *Hyperthermia-triggered drug delivery from iRGD-modified temperature-sensitive liposomes enhances the anti-tumor efficacy using high intensity focused ultrasound.* J Control Release, 2016. **243**: p. 333-341.
37. Han, H., et al., *Effect of high intensity focused ultrasound (HIFU) in conjunction with a nanomedicines-microbubble complex for enhanced drug delivery.* J Control Release, 2017. **266**: p. 75-86.
38. Hijnen, N., et al., *Thermal combination therapies for local drug delivery by magnetic resonance-guided high-intensity focused ultrasound.* Proc Natl Acad Sci U S A, 2017. **114**(24): p. E4802-E4811.
39. Ulbrich, K., et al., *Targeted Drug Delivery with Polymers and Magnetic Nanoparticles: Covalent and Noncovalent Approaches, Release Control, and Clinical Studies.* Chem Rev, 2016. **116**(9): p. 5338-431.
40. Zhang, N., et al., *A Multifunctional Theranostic Nanoagent for Dual-Mode Image-Guided HIFU/Chemo- Synergistic Cancer Therapy.* Theranostics, 2016. **6**(3): p. 404-17.
41. Rosenberg, J., et al., *Hyperthermia associated with drug intoxication.* Crit Care Med, 1986. **14**(11): p. 964-9.
42. Baronzio, G.F. and E.D. Hager, *Hyperthermia in cancer treatment : a primer*. Medical intelligence unit. 2006, Georgetown, Tex.

New York, N.Y.: Landes Bioscience/Eurekah.com ;
Springer Science + Business Media. 366 p.

43. Wust, P., et al., *Hyperthermia in combined treatment of cancer.* Lancet Oncol, 2002. **3**(8): p. 487-97.
44. Kong, G., R.D. Braun, and M.W. Dewhirst, *Characterization of the effect of hyperthermia on nanoparticle extravasation from tumor vasculature.* Cancer Res, 2001. **61**(7): p. 3027-32.
45. Bettaieb, A., Wrzal, P.K., and Averill-Bates, D.A., *Hyperthermia: Cancer Treatment and Beyond*, in *Cancer Treatment - Convnetional and Innovative Approaches*, L. Rangel, Editor. 2013, InTech.
46. Sugahara, T., et al., *Kadota Fund International Forum 2004. Application of thermal stress for the improvement of health, 15-18 June 2004, Awaji Yumebutai International Conference Center, Awaji Island, Hyogo, Japan. Final report.* Int J Hyperthermia, 2008. **24**(2): p. 123-40.
47. Pallepati, P. and D.A. Averill-Bates, *Mild thermotolerance induced at 40 degrees C protects HeLa cells against activation of death receptor-mediated apoptosis by hydrogen peroxide.* Free Radic Biol Med, 2011. **50**(6): p. 667-79.
48. Vujaskovic, Z., et al., *Temperature-dependent changes in physiologic parameters of spontaneous canine soft tissue sarcomas after combined radiotherapy and hyperthermia treatment.* Int J Radiat Oncol Biol Phys, 2000. **46**(1): p. 179-85.
49. Karino, T., S. Koga, and M. Maeta, *Experimental studies of the effects of local hyperthermia on blood flow, oxygen pressure and pH in tumors.* Jpn J Surg, 1988. **18**(3): p. 276-83.

50. Lepock, J.R., *Role of nuclear protein denaturation and aggregation in thermal radiosensitization.* Int J Hyperthermia, 2004. **20**(2): p. 115-30.
51. Dewey, W.C., et al., *Cellular responses to combinations of hyperthermia and radiation.* Radiology, 1977. **123**(2): p. 463-74.
52. Song, C.W., et al., *Implications of increased tumor blood flow and oxygenation caused by mild temperature hyperthermia in tumor treatment.* Int J Hyperthermia, 2005. **21**(8): p. 761-7.
53. Vernon, C.C., et al., *Radiotherapy with or without hyperthermia in the treatment of superficial localized breast cancer: results from five randomized controlled trials. International Collaborative Hyperthermia Group.* Int J Radiat Oncol Biol Phys, 1996. **35**(4): p. 731-44.
54. van der Zee, J., et al., *Comparison of radiotherapy alone with radiotherapy plus hyperthermia in locally advanced pelvic tumours: a prospective, randomised, multicentre trial. Dutch Deep Hyperthermia Group.* Lancet, 2000. **355**(9210): p. 1119-25.
55. Franckena, M., et al., *Long-term improvement in treatment outcome after radiotherapy and hyperthermia in locoregionally advanced cervix cancer: an update of the Dutch Deep Hyperthermia Trial.* Int J Radiat Oncol Biol Phys, 2008. **70**(4): p. 1176-82.
56. Wen, Q.L., et al., *Comparing radiotherapy with or without intracavitary hyperthermia in the treatment of primary nasopharyngeal carcinoma: a retrospective analysis.* Tumori, 2014. **100**(1): p. 49-54.
57. Song, C.W., *Effect of local hyperthermia on blood flow and microenvironment: a review.* Cancer Res, 1984. **44**(10 Suppl): p. 4721s-4730s.
58. Saad, A.H. and G.M. Hahn, *Ultrasound enhanced drug toxicity on Chinese hamster ovary cells in vitro.* Cancer Res, 1989. **49**(21): p. 5931-4.
59. Hildebrandt, B., et al., *The cellular and molecular basis of hyperthermia.* Crit Rev Oncol Hematol, 2002. **43**(1): p. 33-56.
60. Sugimachi, K., et al., *Chemotherapy combined with or without hyperthermia for patients with oesophageal carcinoma: a prospective randomized trial.* Int J Hyperthermia, 1994. **10**(4): p. 485-93.
61. Issels, R.D., et al., *Neo-adjuvant chemotherapy alone or with regional hyperthermia for localised high-risk soft-tissue sarcoma: a randomised phase 3 multicentre study.* Lancet Oncol, 2010. **11**(6): p. 561-70.
62. Colombo, R., et al., *Long-term outcomes of a randomized controlled trial comparing thermochemotherapy with mitomycin-C alone as adjuvant treatment for non-muscle-invasive bladder cancer (NMIBC).* BJU Int, 2011. **107**(6): p. 912-8.
63. Shen, H., et al., *The regimen of gemcitabine and cisplatin combined with radio frequency hyperthermia for advanced non-small cell lung cancer: a phase II study.* Int J Hyperthermia, 2011. **27**(1): p. 27-32.
64. Kong, G., R.D. Braun, and M.W. Dewhirst, *Hyperthermia enables tumor-specific nanoparticle delivery: effect of particle size.* Cancer Res, 2000. **60**(16): p. 4440-5.
65. Needham, D. and M.W. Dewhirst, *The development and testing of a new temperature-sensitive drug delivery system for the treatment of solid tumors.* Adv Drug Deliv Rev, 2001. **53**(3): p. 285-305.

66. Patra, S., et al., *Dual-responsive polymer coated superparamagnetic nanoparticle for targeted drug delivery and hyperthermia treatment.* ACS Appl Mater Interfaces, 2015. **7**(17): p. 9235-46.
67. Toraya-Brown, S. and S. Fiering, *Local tumour hyperthermia as immunotherapy for metastatic cancer.* Int J Hyperthermia, 2014. **30**(8): p. 531-9.
68. Skitzki, J.J., E.A. Repasky, and S.S. Evans, *Hyperthermia as an immunotherapy strategy for cancer.* Curr Opin Investig Drugs, 2009. **10**(6): p. 550-8.
69. Takeda, T. and T. Takeda, *Combination by Hyperthermia and Immunotherapy: DC Therapy and Hyperthermia*, in *Hyperthermic Oncology from Bench to Bedside*, S. Kokura, T. Yoshikawa, and T. Ohnishi, Editors. 2016, Springer Singapore: Singapore. p. 319-327.
70. Miller, D.L., et al., *Overview of therapeutic ultrasound applications and safety considerations.* J Ultrasound Med, 2012. **31**(4): p. 623-34.
71. Zhou, Q., et al., *Piezoelectric single crystals for ultrasonic transducers in biomedical applications.* Prog Mater Sci, 2014. **66**: p. 87-111.
72. Chan, V., Perlas, A., *Basics of Ultrasound Imaging*, in *Atlas of Ultrasound-Guided Procedures in Interventional Pain Management*, S.N. Narouze, Editor. 2011, Springer-Verlag New York. p. 13-19.
73. Hynynen, K. and R.M. Jones, *Image-guided ultrasound phased arrays are a disruptive technology for non-invasive therapy.* Phys Med Biol, 2016. **61**(17): p. R206-48.
74. Adams, M.S., *Endoluminal ultrasound applicators for thermal therapy of pancreatic tumors*, 2017, [Order No. 10599836]. University of California, San Francisco.
75. Deardorff, D.L., C.J. Diederich, and W.H. Nau, *Control of interstitial thermal coagulation: comparative evaluation of microwave and ultrasound applicators.* Med Phys, 2001. **28**(1): p. 104-17.
76. Ni, Y., et al., *A review of the general aspects of radiofrequency ablation.* Abdom Imaging, 2005. **30**(4): p. 381-400.
77. Brace, C.L., *Microwave tissue ablation: biophysics, technology, and applications.* Crit Rev Biomed Eng, 2010. **38**(1): p. 65-78.
78. Nishikawa, H. and Y. Osaki, *Comparison of high-intensity focused ultrasound therapy and radiofrequency ablation for recurrent hepatocellular carcinoma.* Hepatobiliary Surg Nutr, 2013. **2**(3): p. 168-70.
79. Kim, Y.S., et al., *High-intensity focused ultrasound therapy: an overview for radiologists.* Korean J Radiol, 2008. **9**(4): p. 291-302.
80. Hesley, G.K., K.R. Gorny, and D.A. Woodrum, *MR-Guided Focused Ultrasound for the Treatment of Uterine Fibroids.* CardioVascular and Interventional Radiology, 2013. **36**(1): p. 5-13.
81. Pron, G., *Magnetic Resonance-Guided High-Intensity Focused Ultrasound (MRgHIFU) Treatment of Symptomatic Uterine Fibroids: An Evidence-Based Analysis.* Ont Health Technol Assess Ser, 2015. **15**(4): p. 1-86.
82. Coakley, F.V., et al., *Pelvic applications of MR-guided high intensity focused ultrasound.* Abdominal Imaging, 2013. **38**(5): p. 1120-1129.
83. Abe, K. and T. Taira, *Focused Ultrasound Treatment, Present and Future.* Neurol Med Chir (Tokyo), 2017. **57**(8): p. 386-391.

84. Mihcin, S., et al., *Methodology on quantification of sonication duration for safe application of MR guided focused ultrasound for liver tumour ablation.* Comput Methods Programs Biomed, 2017. **152**: p. 125-130.
85. Singh, V.A., et al., *Magnetic resonance guided focused ultrasound for treatment of bone tumors.* J Orthop Surg (Hong Kong), 2017. **25**(2): p. 2309499017716256.
86. Bretsztajn, L. and W. Gedroyc, *Brain Focused Ultrasound: what's the 'FUS' all about? A review of current and emerging neurological applications.* Br J Radiol, 2018: p. 20170481.
87. Coluccia, D., et al., *Enhancing Glioblastoma Treatment using Cisplatin-Gold-Nanoparticle Conjugates and Targeted Delivery with Magnetic Resonance-Guided Focused Ultrasound.* Nanomedicine, 2018.
88. Iacopino, D.G., et al., *Preliminary experience with a transcranial magnetic resonance-guided focused ultrasound surgery system integrated with a 1.5-T MRI unit in a series of patients with essential tremor and Parkinson's disease.* Neurosurg Focus, 2018. **44**(2): p. E7.
89. Ichikawa, S., et al., *MR-guided Focused Ultrasound for Uterine Fibroids: A Preliminary Study of Relationship between the Treatment Outcomes and Factors of MR Images Including Elastography.* Magn Reson Med Sci, 2018.
90. Lamsam, L., et al., *A review of potential applications of MR-guided focused ultrasound for targeting brain tumor therapy.* Neurosurg Focus, 2018. **44**(2): p. E10.
91. Dickson, J.A. and D.S. Muckle, *Total-body hyperthermia versus primary tumor hyperthermia in the treatment of the rabbit VX-2 carcinoma.* Cancer Res, 1972. **32**(9): p. 1916-23.
92. Overgaard, J., *Simultaneous and sequential hyperthermia and radiation treatment of an experimental tumor and its surrounding normal tissue in vivo.* Int J Radiat Oncol Biol Phys, 1980. **6**(11): p. 1507-17.
93. Dahl, O., *Effect of hyperthermia on a neurogenic rat cell line (BT4A) in vivo.* Acta Radiol Oncol, 1982. **21**(1): p. 67-77.
94. Miyamoto, R., et al., *Cetuximab delivery and antitumor effects are enhanced by mild hyperthermia in a xenograft mouse model of pancreatic cancer.* Cancer Sci, 2016. **107**(4): p. 514-20.
95. Lokerse, W.J.M., et al., *Comparing the therapeutic potential of thermosensitive liposomes and hyperthermia in two distinct subtypes of breast cancer.* J Control Release, 2017. **258**: p. 34-42.
96. Lord, P.F., et al., *Production of systemic hyperthermia in the rat.* Eur J Cancer Clin Oncol, 1984. **20**(8): p. 1079-85.
97. Horkan, C., et al., *Radiofrequency ablation: Effect of pharmacologic modulation of hepatic and renal blood flow on coagulation diameter in a VX2 tumor model.* J Vasc Interv Radiol, 2004. **15**(3): p. 269-74.
98. Hakime, A., et al., *Combination of radiofrequency ablation with antiangiogenic therapy for tumor ablation efficacy: study in mice.* Radiology, 2007. **244**(2): p. 464-70.
99. Yang, W., et al., *Radiofrequency ablation combined with liposomal quercetin to increase tumour destruction by modulation of heat shock protein production in a small animal model.* Int J Hyperthermia, 2011. **27**(6): p. 527-38.

100. Moussa, M., et al., *Effect of thermal dose on heat shock protein expression after radio-frequency ablation with and without adjuvant nanoparticle chemotherapies.* Int J Hyperthermia, 2016. **32**(8): p. 829-841.
101. Velez, E., et al., *Hepatic Thermal Ablation: Effect of Device and Heating Parameters on Local Tissue Reactions and Distant Tumor Growth.* Radiology, 2016. **281**(3): p. 782-792.
102. Shi, Y., et al., *Orthotopic Esophageal Cancers: Intraesophageal Hyperthermia-enhanced Direct Chemotherapy in Rats.* Radiology, 2017. **282**(1): p. 103-112.
103. Breen, M.S., et al., *Three-dimensional comparison of interventional MR radiofrequency ablation images with tissue response.* Comput Aided Surg, 2004. **9**(5): p. 185-91.
104. Lepetit-Coiffe, M., et al., *Real-time monitoring of radiofrequency ablation of rabbit liver by respiratory-gated quantitative temperature MRI.* J Magn Reson Imaging, 2006. **24**(1): p. 152-9.
105. Wu, H., et al., *Real-time monitoring of radiofrequency ablation and postablation assessment: accuracy of contrast-enhanced US in experimental rat liver model.* Radiology, 2014. **270**(1): p. 107-16.
106. Ueki, A., et al., *Therapeutic Effects of CT-guided Radiofrequency Ablation with Concurrent Platinum-Doublet Chemotherapy in a Rabbit VX2 Lung Tumor Model.* Radiology, 2017. **283**(2): p. 391-398.
107. Pandeya, G.D., et al., *Feasibility of noninvasive temperature assessment during radiofrequency liver ablation on computed tomography.* J Comput Assist Tomogr, 2011. **35**(3): p. 356-60.
108. Chen, Z., et al., *Intratumoural GM-CSF microspheres and CTLA-4 blockade enhance the antitumour immunity induced by thermal ablation in a subcutaneous murine hepatoma model.* Int J Hyperthermia, 2009. **25**(5): p. 374-82.
109. Yoon, J., et al., *High-frequency microwave ablation method for enhanced cancer treatment with minimized collateral damage.* Int J Cancer, 2011. **129**(8): p. 1970-8.
110. Hinshaw, J.L., et al., *Percutaneous tumor ablation tools: microwave, radiofrequency, or cryoablation--what should you use and why?* Radiographics, 2014. **34**(5): p. 1344-62.
111. Ohno, T., et al., *Expansion of an ablated site and induction of apoptosis after microwave coagulation therapy in rat liver.* J Hepatobiliary Pancreat Surg, 2001. **8**(4): p. 360-6.
112. Bhardwaj, N., et al., *A comparative histological evaluation of the ablations produced by microwave, cryotherapy and radiofrequency in the liver.* Pathology, 2009. **41**(2): p. 168-72.
113. Salahi, S., et al., *Miniature microwave applicator for murine bladder hyperthermia studies.* Int J Hyperthermia, 2012. **28**(5): p. 456-65.
114. Hohenforst-Schmidt, W., et al., *Enhancement of Intratumoral Chemotherapy with Cisplatin with or without Microwave Ablation and Lipiodol. Future Concept for Local Treatment in Lung Cancer.* J Cancer, 2015. **6**(3): p. 218-26.
115. Vogl, T.J., et al., *Study on the effect of chemoembolization combined with microwave ablation for the treatment of hepatocellular carcinoma in rats.* Diagn Interv Radiol, 2017. **23**(2): p. 150-155.
116. Zhu, J., et al., *Enhanced antitumor efficacy through microwave ablation in combination with immune checkpoints blockade in breast cancer: A pre-clinical study in a murine model.* Diagn Interv Imaging, 2018.

117. Moon, T.J. and C.L. Brace, *Design of a dual slot antenna for small animal microwave ablation studies.* Conf Proc IEEE Eng Med Biol Soc, 2016. **2016**: p. 348-351.
118. Curto, S., et al., *An integrated platform for small-animal hyperthermia investigations under ultra-high-field MRI guidance.* Int J Hyperthermia, 2017: p. 1-11.
119. Fite, B.Z., et al., *Magnetic resonance thermometry at 7T for real-time monitoring and correction of ultrasound induced mild hyperthermia.* PLoS One, 2012. **7**(4): p. e35509.
120. Rapoport, N., et al., *Focused ultrasound-mediated drug delivery to pancreatic cancer in a mouse model.* J Ther Ultrasound, 2013. **1**: p. 11.
121. Liu, Y., et al., *Concurrent Visualization of Acoustic Radiation Force Displacement and Shear Wave Propagation with 7T MRI.* PLoS One, 2015. **10**(10): p. e0139667.
122. Wong, A.W., et al., *Ultrasound ablation enhances drug accumulation and survival in mammary carcinoma models.* J Clin Invest, 2016. **126**(1): p. 99-111.
123. Albers, M.J., et al., *Hyperpolarized 13C lactate, pyruvate, and alanine: noninvasive biomarkers for prostate cancer detection and grading.* Cancer Res, 2008. **68**(20): p. 8607-15.
124. Rieke, V. and K. Butts Pauly, *MR thermometry.* J Magn Reson Imaging, 2008. **27**(2): p. 376-90.
125. Wang, P., *Evaluation of MR thermometry with proton resonance frequency method at 7T.* Quant Imaging Med Surg, 2017. **7**(2): p. 259-266.
126. Nishimura, D.G., *Principles of Magnetic Resonance Imaging*. 1.1 ed. 2010: http://www.lulu.com.
127. Abd-Alazeez, M., et al., *The accuracy of multiparametric MRI in men with negative biopsy and elevated PSA level--can it rule out clinically significant prostate cancer?* Urol Oncol, 2014. **32**(1): p. 45 e17-22.
128. Bratan, F., et al., *Influence of imaging and histological factors on prostate cancer detection and localisation on multiparametric MRI: a prospective study.* Eur Radiol, 2013. **23**(7): p. 2019-29.
129. de Rooij, M., et al., *Accuracy of multiparametric MRI for prostate cancer detection: a meta-analysis.* AJR Am J Roentgenol, 2014. **202**(2): p. 343-51.
130. Kurhanewicz, J. and D.B. Vigneron, *Magnetic Resonance Spectroscopy of Prostate Cancer.* Emagres, 2016. **5**(1): p. 923-943.
131. Elster, A.D., *Questions and Answers in Magnetic Resonance Imaging*. 1994, St. Louis, Missouri: Mosby-Year Book, Inc.
132. Oh, W.K., Hurwitz, M., D'Amico, A.V., et al., *Biology of Prostate Cancer*, in *Holland-Frei Cancer Medicine*, D.W. Kufe, Pollock, R.E., Weichselbaum, R.R., et al., Editor. 2003, BC Decker: Hamilton (ON).
133. Anwar, S.S., et al., *Assessment of apparent diffusion coefficient values as predictor of aggressiveness in peripheral zone prostate cancer: comparison with Gleason score.* ISRN Radiol, 2014. **2014**: p. 263417.
134. Esen, M., et al., *Utility of ADC measurement on diffusion-weighted MRI in differentiation of prostate cancer, normal prostate and prostatitis.* Quant Imaging Med Surg, 2013. **3**(4): p. 210-6.
135. Lebovici, A., et al., *Evaluation of the normal-to-diseased apparent diffusion coefficient ratio as an indicator of prostate cancer aggressiveness.* Bmc Medical Imaging, 2014. **14**.

136. Itou, Y., et al., *Clinical utility of apparent diffusion coefficient (ADC) values in patients with prostate cancer: can ADC values contribute to assess the aggressiveness of prostate cancer?* J Magn Reson Imaging, 2011. **33**(1): p. 167-72.
137. Wang, H.Z., S.J. Riederer, and J.N. Lee, *Optimizing the precision in T1 relaxation estimation using limited flip angles.* Magn Reson Med, 1987. **5**(5): p. 399-416.
138. Buckley, D., Parker, G., *Measuring Contrast Agent Concentration in T1-Weighted Dynamic Contrast-Enhanced MRI*, in *Dynamic Contrast-Enhanced Magnetic Resonance Imaging in Oncology*, A. Jackson, Buckley, D., Parker, G., Editor. 2005, Springer: New York.
139. Fukunaga, T., et al., *Accuracy of semiquantitative dynamic contrast-enhanced MRI for differentiating type II from type I endometrial carcinoma.* J Magn Reson Imaging, 2015. **41**(6): p. 1662-8.
140. Isebaert, S., et al., *Evaluation of semi-quantitative dynamic contrast-enhanced MRI parameters for prostate cancer in correlation to whole-mount histopathology.* Eur J Radiol, 2012. **81**(3): p. e217-22.
141. Kazerooni, A.F., et al., *Semiquantitative dynamic contrast-enhanced MRI for accurate classification of complex adnexal masses.* J Magn Reson Imaging, 2017. **45**(2): p. 418-427.
142. Medved, M., et al., *Semiquantitative analysis of dynamic contrast enhanced MRI in cancer patients: Variability and changes in tumor tissue over time.* J Magn Reson Imaging, 2004. **20**(1): p. 122-8.
143. Verma, S., et al., *Overview of dynamic contrast-enhanced MRI in prostate cancer diagnosis and management.* AJR Am J Roentgenol, 2012. **198**(6): p. 1277-88.
144. O'Connor, J.P., et al., *Dynamic contrast-enhanced imaging techniques: CT and MRI.* Br J Radiol, 2011. **84 Spec No 2**: p. S112-20.
145. Chikui, T., et al., *The principal of dynamic contrast enhanced MRI, the method of pharmacokinetic analysis, and its application in the head and neck region.* Int J Dent, 2012. **2012**: p. 480659.
146. Tofts, P.S., et al., *Estimating kinetic parameters from dynamic contrast-enhanced T(1)-weighted MRI of a diffusable tracer: standardized quantities and symbols.* J Magn Reson Imaging, 1999. **10**(3): p. 223-32.
147. Berman, R.M., et al., *DCE MRI of prostate cancer.* Abdom Radiol (NY), 2016. **41**(5): p. 844-53.
148. Choi, Y.J., et al., *Functional MR imaging of prostate cancer.* Radiographics, 2007. **27**(1): p. 63-75; discussion 75-7.
149. Brawer, M.K., et al., *Predictors of pathologic stage in prostatic carcinoma. The role of neovascularity.* Cancer, 1994. **73**(3): p. 678-87.
150. Noworolski, S.M., et al., *Dynamic contrast-enhanced MRI in normal and abnormal prostate tissues as defined by biopsy, MRI, and 3D MRSI.* Magn Reson Med, 2005. **53**(2): p. 249-55.
151. Zidan, S., Tantawy, H.I., *Prostate carcinoma: Accuracy of diagnosis and differentiation with Dynamic Contrast-Enhanced MRI and Diffusion Weighted Imaging.* The Egyptian Journal of Radiology and Nuclear Medicine, 2015. **46**(4): p. 1193-1203.
152. Sung, Y.S., et al., *Prostate cancer detection on dynamic contrast-enhanced MRI: computer-aided diagnosis versus single perfusion parameter maps.* AJR Am J Roentgenol, 2011. **197**(5): p. 1122-9.

153. Ocak, I., et al., *Dynamic contrast-enhanced MRI of prostate cancer at 3 T: a study of pharmacokinetic parameters.* AJR Am J Roentgenol, 2007. **189**(4): p. 849.
154. Tan, C.H., et al., *Dynamic contrast-enhanced MRI for the detection of prostate cancer: meta-analysis.* AJR Am J Roentgenol, 2015. **204**(4): p. W439-48.
155. Sankineni, S., M. Osman, and P.L. Choyke, *Functional MRI in prostate cancer detection.* Biomed Res Int, 2014. **2014**: p. 590638.
156. Kurhanewicz, J., et al., *Combined magnetic resonance imaging and spectroscopic imaging approach to molecular imaging of prostate cancer.* J Magn Reson Imaging, 2002. **16**(4): p. 451-63.
157. Aboagye, E.O. and Z.M. Bhujwalla, *Malignant transformation alters membrane choline phospholipid metabolism of human mammary epithelial cells.* Cancer Res, 1999. **59**(1): p. 80-4.
158. Cuadrado, A., et al., *Phosphorylcholine: a novel second messenger essential for mitogenic activity of growth factors.* Oncogene, 1993. **8**(11): p. 2959-68.
159. Exton, J.H., *Phosphatidylcholine breakdown and signal transduction.* Biochim Biophys Acta, 1994. **1212**(1): p. 26-42.
160. Galons, J.P., et al., *Metabolic changes in undifferentiated and differentiated human colon adenocarcinoma cells studied by multinuclear magnetic resonance spectroscopy.* Biochimie, 1989. **71**(8): p. 949-61.
161. Vigneron, D.B., Males, R., Hricak, H., Noworolski, S., Carrol, P.R., Kurhanewicz, J. *Prostate cancer: correlation of 3D MRSI metabolite levels with histologic grade*. in *RSNA*. 1998. Chicago.
162. Panebianco, V., et al., *Pitfalls in Interpreting mp-MRI of the Prostate: A Pictorial Review with Pathologic Correlation.* Insights Imaging, 2015. **6**(6): p. 611-30.
163. Quon, J.S., et al., *False positive and false negative diagnoses of prostate cancer at multi-parametric prostate MRI in active surveillance.* Insights Imaging, 2015. **6**(4): p. 449-63.
164. Ha, M. and V.K. Michaelis, *High-Frequency Dynamic Nuclear Polarization NMR for Solids: Part 1 – An Introduction*, in *Modern Magnetic Resonance*, G.A. Webb, Editor. 2017, Springer International Publishing: Cham. p. 1-24.
165. Hurd, R.E., et al., *Hyperpolarized 13C metabolic imaging using dissolution dynamic nuclear polarization.* J Magn Reson Imaging, 2012. **36**(6): p. 1314-28.
166. Warburg, O., *The Metabolism of Carcinoma Cells.* The Journal of Cancer Research, 1925. **9**(1): p. 148-163.
167. Vander Heiden, M.G., L.C. Cantley, and C.B. Thompson, *Understanding the Warburg effect: the metabolic requirements of cell proliferation.* Science, 2009. **324**(5930): p. 1029-33.
168. Liberti, M.V. and J.W. Locasale, *The Warburg Effect: How Does it Benefit Cancer Cells?* Trends Biochem Sci, 2016. **41**(3): p. 211-8.
169. Nelson, S.J., et al., *Metabolic imaging of patients with prostate cancer using hyperpolarized [1-(1)(3)C]pyruvate.* Sci Transl Med, 2013. **5**(198): p. 198ra108.
170. Brindle, K.M., et al., *Tumor imaging using hyperpolarized 13C magnetic resonance spectroscopy.* Magn Reson Med, 2011. **66**(2): p. 505-19.
171. von Morze, C., et al., *Imaging of blood flow using hyperpolarized [(13)C]urea in preclinical cancer models.* J Magn Reson Imaging, 2011. **33**(3): p. 692-7.

172. von Morze, C., et al., *Monitoring urea transport in rat kidney in vivo using hyperpolarized (1)(3)C magnetic resonance imaging.* Am J Physiol Renal Physiol, 2012. **302**(12): p. F1658-62.
173. Lau, A.Z., et al., *Cardiac perfusion imaging using hyperpolarized (13)C urea using flow sensitizing gradients.* Magn Reson Med, 2016. **75**(4): p. 1474-83.
174. Wilson, D.M., et al., *Multi-compound polarization by DNP allows simultaneous assessment of multiple enzymatic activities in vivo.* J Magn Reson, 2010. **205**(1): p. 141-7.
175. Sukumar, S., Larson, P.E., Keshari, K., Kurhanewicz, J., Vigneron, D. *Single Shot, Chemical Shift Specific Imaging Methods for Hyperpolarized Carbon-13 Studies at 14T*. in *International Society of Magnetic Resonance in Medicine*. 2010. Stockholm, Sweden.
176. Sukumar, S., Hu, S., Larson, P.E., Zhang, V.Y., Ohliger, M., Bok, R., Kurhanewicz, J., Vigneron, D. *Single-shot, 2D and 3D Dynamic Imaging of Hyperpolarized 13C Biomarkers In Vivo at 14.1 Tesla*. in *International Society for Magnetic Resonance in Medicine*. 2012. Melbourne, Australia.
177. Oshio, K. and D.A. Feinberg, *Single-Shot Grase Imaging without Fast Gradients.* Magnetic Resonance in Medicine, 1992. **26**(2): p. 355-360.
178. Chen, J., B.L. Daniel, and K.B. Pauly, *Investigation of proton density for measuring tissue temperature.* J Magn Reson Imaging, 2006. **23**(3): p. 430-4.
179. Nelson, T.R. and S.M. Tung, *Temperature dependence of proton relaxation times in vitro.* Magn Reson Imaging, 1987. **5**(3): p. 189-99.
180. Peller, M., et al., *T1 relaxation time at 0.2 Tesla for monitoring regional hyperthermia: feasibility study in muscle and adipose tissue.* Magn Reson Med, 2002. **47**(6): p. 1194-201.
181. Quesson, B., J.A. de Zwart, and C.T. Moonen, *Magnetic resonance temperature imaging for guidance of thermotherapy.* J Magn Reson Imaging, 2000. **12**(4): p. 525-33.
182. Moseley, M.E., et al., *Early detection of regional cerebral ischemia in cats: comparison of diffusion- and T2-weighted MRI and spectroscopy.* Magn Reson Med, 1990. **14**(2): p. 330-46.
183. Hindman, J.C., *Proton Resonance Shift of Water in Gas and Liquid States.* Journal of Chemical Physics, 1966. **44**(12): p. 4582-&.
184. Schneider, W.G., Bernstein, H.J., Pople, J.A., *Proton Magnetic Resonance Chemical Shift of Free (Gaseous) and Associated (Liquid) Hydride Molecules.* The Journal of Chemical Physics, 1958. **28**(4): p. 601-607.
185. Ishihara, Y., et al., *A precise and fast temperature mapping using water proton chemical shift.* Magn Reson Med, 1995. **34**(6): p. 814-23.
186. El-Sharkawy, A.M., et al., *Monitoring and correcting spatio-temporal variations of the MR scanner's static magnetic field.* MAGMA, 2006. **19**(5): p. 223-36.
187. Kuroda, K., et al., *Temperature mapping using the water proton chemical shift: a chemical shift selective phase mapping method.* Magn Reson Med, 1997. **38**(5): p. 845-51.
188. Wyatt, C., et al., *Hyperthermia MRI temperature measurement: evaluation of measurement stabilisation strategies for extremity and breast tumours.* Int J Hyperthermia, 2009. **25**(6): p. 422-33.

189. De Poorter, J., et al., *Noninvasive MRI thermometry with the proton resonance frequency (PRF) method: in vivo results in human muscle.* Magn Reson Med, 1995. **33**(1): p. 74-81.
190. Bing, C., et al., *Drift correction for accurate PRF-shift MR thermometry during mild hyperthermia treatments with MR-HIFU.* Int J Hyperthermia, 2016. **32**(6): p. 673-87.
191. Escoffre, J.M. and A. Bouakaz, *Therapeutic Ultrasound*. 2015: Springer International Publishing.
192. de Senneville, B.D., et al., *Motion correction in MR thermometry of abdominal organs: a comparison of the referenceless vs. the multibaseline approach.* Magn Reson Med, 2010. **64**(5): p. 1373-81.
193. Salomir, R., et al., *Reference-free PRFS MR-thermometry using near-harmonic 2-D reconstruction of the background phase.* IEEE Trans Med Imaging, 2012. **31**(2): p. 287-301.
194. Chen, R.C., et al., *Association Between Choice of Radical Prostatectomy, External Beam Radiotherapy, Brachytherapy, or Active Surveillance and Patient-Reported Quality of Life Among Men With Localized Prostate Cancer.* JAMA, 2017. **317**(11): p. 1141-1150.
195. Serrell, E.C., et al., *Review of the comparative effectiveness of radical prostatectomy, radiation therapy, or expectant management of localized prostate cancer in registry data.* Urol Oncol, 2017.
196. Jain, A.K. and R.D. Ennis, *Focal therapy, differential therapy, and radiation treatment for prostate cancer.* Adv Urol, 2012. **2012**: p. 573193.
197. Tay, K.J., et al., *New advances in focal therapy for early stage prostate cancer.* Expert Rev Anticancer Ther, 2017. **17**(8): p. 737-743.
198. Woodrum, D.A., et al., *Prostate cancer: state of the art imaging and focal treatment.* Clin Radiol, 2017. **72**(8): p. 665-679.
199. Mendhiratta, N., Taneja, S.S., *Focal Therapy for Prostate Cancer*, in *Prostate Cancer: Science and Clincial Practice*, J.H. Mydlo, Godec, C.J., Editor. 2016, Elsevier Ltd.
200. Sivaraman, A. and E. Barret, *Focal Therapy for Prostate Cancer: An "A la Carte" Approach.* Eur Urol, 2016. **69**(6): p. 973-5.
201. Cline, H.E., et al., *Focused US system for MR imaging-guided tumor ablation.* Radiology, 1995. **194**(3): p. 731-7.
202. Copelan, A., et al., *High-Intensity Focused Ultrasound: Current Status for Image-Guided Therapy.* Semin Intervent Radiol, 2015. **32**(4): p. 398-415.
203. Kennedy, J.E., G.R. Ter Haar, and D. Cranston, *High intensity focused ultrasound: surgery of the future?* Br J Radiol, 2003. **76**(909): p. 590-9.
204. Coad, J.E., *Practical Pathology Perspectives for Minimally Invasive Hyperthermic Medical Devices*, in *SPIE*, T.P. Ryan, Editor 2011: San Francisco, CA.
205. Wang, Y., et al., *Ultrasound-guided high-intensity focused ultrasound treatment for abdominal wall endometriosis: preliminary results.* Eur J Radiol, 2011. **79**(1): p. 56-9.
206. Orsi, F., et al., *Ultrasound guided high intensity focused ultrasound (USgHIFU) ablation for uterine fibroids: Do we need the microbubbles?* Int J Hyperthermia, 2015. **31**(3): p. 233-9.
207. Zhou, M., et al., *Ultrasound-guided high-intensity focused ultrasound ablation for adenomyosis: the clinical experience of a single center.* Fertil Steril, 2011. **95**(3): p. 900-5.

208. Foley, J.L., et al., *Image-guided HIFU neurolysis of peripheral nerves to treat spasticity and pain.* Ultrasound Med Biol, 2004. **30**(9): p. 1199-207.
209. Jolesz, F.A., *MRI-guided focused ultrasound surgery.* Annu Rev Med, 2009. **60**: p. 417-30.
210. Napoli, A., et al., *MR-guided high-intensity focused ultrasound: current status of an emerging technology.* Cardiovasc Intervent Radiol, 2013. **36**(5): p. 1190-203.
211. Maloney, E. and J.H. Hwang, *Emerging HIFU applications in cancer therapy.* Int J Hyperthermia, 2015. **31**(3): p. 302-9.
212. Verma, S., Lamba, M.A.S., Vigneron, D.B., Jung, A., Kurhanewicz, J., *Multi-parametric Magnetic Resonance Imaging Approaches in Focal Prostate Cancer Therapy*, in *Imaging and Focal Therapy of Early Prostate Cancer*, T.J. Polascik, Editor. 2012, Springer: USA.
213. Lewa, C.J. and Z. Majewska, *Temperature relationships of proton spin-lattice relaxation time T1 in biological tissues.* Bull Cancer, 1980. **67**(5): p. 525-30.
214. Kim, Y.S., *Advances in MR image-guided high-intensity focused ultrasound therapy.* Int J Hyperthermia, 2015. **31**(3): p. 225-32.
215. Yiallouras, C. and C. Damianou, *Review of MRI positioning devices for guiding focused ultrasound systems.* Int J Med Robot, 2015. **11**(2): p. 247-55.
216. Zini, C., et al., *Ultrasound- and MR-guided focused ultrasound surgery for prostate cancer.* World J Radiol, 2012. **4**(6): p. 247-52.
217. Napoli, A., et al., *Real-time magnetic resonance-guided high-intensity focused ultrasound focal therapy for localised prostate cancer: preliminary experience.* Eur Urol, 2013. **63**(2): p. 395-8.
218. Chopra, R., *Transurethral MR-HIFU for the treatment of localized prostate cancer.* J Ther Ultrasound, 2015(3(Suppl 1): O59).
219. Aoyagia, R., et al., *Localized elasticity measurement for detection of coagulation during HIFU therapy.* Conf Proc IEEE Eng Med Biol Soc, 2013. **2013**: p. 6273-6.
220. Zhao, W.P., J.Y. Chen, and W.Z. Chen, *Dynamic contrast-enhanced MRI serves as a predictor of HIFU treatment outcome for uterine fibroids with hyperintensity in T2-weighted images.* Exp Ther Med, 2016. **11**(1): p. 328-334.
221. Keshari, K.R., et al., *Metabolic reprogramming and validation of hyperpolarized 13C lactate as a prostate cancer biomarker using a human prostate tissue slice culture bioreactor.* Prostate, 2013. **73**(11): p. 1171-81.
222. Chen, H.Y., et al., *Assessing Prostate Cancer Aggressiveness with Hyperpolarized Dual-Agent 3D Dynamic Imaging of Metabolism and Perfusion.* Cancer Res, 2017. **77**(12): p. 3207-3216.
223. Aggarwal, R., D.B. Vigneron, and J. Kurhanewicz, *Hyperpolarized 1-[(13)C]-Pyruvate Magnetic Resonance Imaging Detects an Early Metabolic Response to Androgen Ablation Therapy in Prostate Cancer.* Eur Urol, 2017. **72**(6): p. 1028-1029.
224. Hurwitz, A.A., et al., *The TRAMP mouse as a model for prostate cancer.* Curr Protoc Immunol, 2001. **Chapter 20**: p. Unit 20 5.
225. Greenberg, N.M., et al., *Prostate cancer in a transgenic mouse.* Proc Natl Acad Sci U S A, 1995. **92**(8): p. 3439-43.
226. Costello, L.C., et al., *Human prostate cancer ZIP1/zinc/citrate genetic/metabolic relationship in the TRAMP prostate cancer animal model.* Cancer Biol Ther, 2011. **12**(12): p. 1078-84.

227. Sukumar, S., et al. *Single-shot Frequency and Time Specific, 3D Imaging Method for Measuring Hyperpolarized 13C Biomarkers In-Viovo at 14.1 Tesla*. in *The International Society for Magnetic Resonance in Medicine*. 2011. Montreal, Quebec, Canada.
228. Beatty, C.J., et al. *Practical pathology for thermal tissue applications*. in *SPIE*. 2015. San Franciaco, CA.
229. Fedorov, A., et al., *3D Slicer as an image computing platform for the Quantitative Imaging Network.* Magn Reson Imaging, 2012. **30**(9): p. 1323-41.
230. Tofts, P.S. and A.G. Kermode, *Measurement of the Blood-Brain-Barrier Permeability and Leakage Space Using Dynamic Mr Imaging .1. Fundamental-Concepts.* Magnet Reson Med, 1991. **17**(2): p. 357-367.
231. Pickup, S., R. Zhou, and J. Glickson, *MRI estimation of the arterial input function in mice.* Acad Radiol, 2003. **10**(9): p. 963-8.
232. *R: A language and environment for statistical computing*, 2015, R Foundation for Statistical Computing: Vienna, Austria.
233. Buckley, D.L. and G.J.M. Parker, *Measuring Contrast Agent Concentration in T1-Weighted Dynamic Contrast-Enhanced MRI*, in *Dynamic Contrast-Enhanced Magnetic Resonance Imaging in Oncology*. 2005, Springer Berlin Heidelberg. p. 69-79.
234. Chen, Y.J., et al., *Washout gradient in dynamic contrast-enhanced MRI is associated with tumor aggressiveness of prostate cancer.* J Magn Reson Imaging, 2012. **36**(4): p. 912-9.
235. Kim, J.K., et al., *Wash-in rate on the basis of dynamic contrast-enhanced MRI: usefulness for prostate cancer detection and localization.* J Magn Reson Imaging, 2005. **22**(5): p. 639-46.
236. Cheng, H.L.M., et al., *Prediction of subtle thermal histopathological change using a novel analysis of Gd-DTPA kinetics.* J Magn Reson Imaging, 2003. **18**(5): p. 585-598.
237. Furusawa, H., et al., *Magnetic resonance-guided focused ultrasound surgery of breast cancer: reliability and effectiveness.* J Am Coll Surg, 2006. **203**(1): p. 54-63.
238. Hectors, S.J., et al., *Multiparametric MRI analysis for the evaluation of MR-guided high intensity focused ultrasound tumor treatment.* NMR Biomed, 2015. **28**(9): p. 1125-40.
239. Kim, K.W., Lee, J.Y., Lee, J.M., Jeon, Y.S., Choi, Y.S., Park, J., Kim, H., Han, J.K., Choi, B.I., *High-intensity Focused Ultrasound Ablation of Soft-tissue Tumors and Assessment of Treatment Response with Multiparametric Magnetic Resonance Imaging: Preliminary Study Using Rabbit VX2 Tumor Model.* J Med Ultrasound, 2014. **22**(2): p. 99-105.
240. Day, S.E., et al., *Detecting tumor response to treatment using hyperpolarized 13C magnetic resonance imaging and spectroscopy.* Nat Med, 2007. **13**(11): p. 1382-7.
241. Day, S.E., et al., *Detecting response of rat C6 glioma tumors to radiotherapy using hyperpolarized [1- 13C]pyruvate and 13C magnetic resonance spectroscopic imaging.* Magn Reson Med, 2011. **65**(2): p. 557-63.
242. Witney, T.H., et al., *Detecting treatment response in a model of human breast adenocarcinoma using hyperpolarised [1-13C]pyruvate and [1,4-13C2]fumarate.* Br J Cancer, 2010. **103**(9): p. 1400-6.
243. Golman, K., et al., *Metabolic imaging by hyperpolarized 13C magnetic resonance imaging for in vivo tumor diagnosis.* Cancer Res, 2006. **66**(22): p. 10855-60.

244. Hijnen, N.M., et al., *Tumour hyperthermia and ablation in rats using a clinical MR-HIFU system equipped with a dedicated small animal set-up.* Int J Hyperthermia, 2012. **28**(2): p. 141-55.
245. Hijnen, N.M., A. Elevelt, and H. Grull, *Stability and trapping of magnetic resonance imaging contrast agents during high-intensity focused ultrasound ablation therapy.* Invest Radiol, 2013. **48**(7): p. 517-24.
246. Hijnen, N.M., et al., *The magnetic susceptibility effect of gadolinium-based contrast agents on PRFS-based MR thermometry during thermal interventions.* J Ther Ultrasound, 2013. **1**: p. 8.
247. Staruch, R.M., et al., *Assessment of acute thermal damage volumes in muscle using magnetization-prepared 3D T2 -weighted imaging following MRI-guided high-intensity focused ultrasound therapy.* J Magn Reson Imaging, 2017. **46**(2): p. 354-364.
248. Yasuda, H., *Solid tumor physiology and hypoxia-induced chemo/radio-resistance: Novel strategy for cancer therapy: Nitric oxide donor as a therapeutic enhancer.* Nitric Oxide-Biology and Chemistry, 2008. **19**(2): p. 205-216.
249. Wilson, D.M. and J. Kurhanewicz, *Hyperpolarized 13C MR for molecular imaging of prostate cancer.* J Nucl Med, 2014. **55**(10): p. 1567-72.
250. Matsuo, M., et al., *Magnetic resonance imaging of the tumor microenvironment in radiotherapy: perfusion, hypoxia, and metabolism.* Semin Radiat Oncol, 2014. **24**(3): p. 210-7.
251. Amadori, D., et al., *Cell proliferation as a predictor of response to chemotherapy in metastatic breast cancer: a prospective study.* Breast Cancer Res Treat, 1997. **43**(1): p. 7-14.
252. Fowler, J.F. and M.A. Ritter, *A rationale for fractionation for slowly proliferating tumors such as prostatic adenocarcinoma.* Int J Radiat Oncol Biol Phys, 1995. **32**(2): p. 521-9.
253. Hegemann, N.S., et al., *Hypofractionated radiotherapy for prostate cancer.* Radiat Oncol, 2014. **9**: p. 275.
254. Chaplin, D.J., P.L. Olive, and R.E. Durand, *Intermittent blood flow in a murine tumor: radiobiological effects.* Cancer Res, 1987. **47**(2): p. 597-601.
255. Hazle, J.D., et al., *MRI-guided thermal therapy of transplanted tumors in the canine prostate using a directional transurethral ultrasound applicator.* J Magn Reson Imaging, 2002. **15**(4): p. 409-17.
256. Van Vulpen, M., et al., *Radiotherapy and hyperthermia in the treatment of patients with locally advanced prostate cancer: preliminary results.* BJU Int, 2004. **93**(1): p. 36-41.
257. Chu, W., et al., *Magnetic Resonance-Guided High-Intensity Focused Ultrasound Hyperthermia for Recurrent Rectal Cancer: MR Thermometry Evaluation and Preclinical Validation.* Int J Radiat Oncol Biol Phys, 2016. **95**(4): p. 1259-67.
258. Kossatz, S., et al., *Efficient treatment of breast cancer xenografts with multifunctionalized iron oxide nanoparticles combining magnetic hyperthermia and anti-cancer drug delivery.* Breast Cancer Res, 2015. **17**: p. 66.
259. Wu, S.K., et al., *Pulsed-wave low-dose ultrasound hyperthermia selectively enhances nanodrug delivery and improves antitumor efficacy for brain metastasis of breast cancer.* Ultrason Sonochem, 2017. **36**: p. 198-205.

260. Hersh, D.S., et al., *Emerging Applications of Therapeutic Ultrasound in Neuro-oncology: Moving Beyond Tumor Ablation.* Neurosurgery, 2016. **79**(5): p. 643-654.
261. Servadio, C. and Z. Leib, *Hyperthermia in the treatment of prostate cancer.* Prostate, 1984. **5**(2): p. 205-11.
262. Kok, H.P., et al., *Current state of the art of regional hyperthermia treatment planning: a review.* Radiat Oncol, 2015. **10**: p. 196.
263. Dewhirst, M.W., C.T. Lee, and K.A. Ashcraft, *The future of biology in driving the field of hyperthermia.* Int J Hyperthermia, 2016. **32**(1): p. 4-13.
264. van den Tempel, N., et al., *The effect of thermal dose on hyperthermia-mediated inhibition of DNA repair through homologous recombination.* Oncotarget, 2017. **8**(27): p. 44593-44604.
265. Oto, A., et al., *MR imaging-guided focal laser ablation for prostate cancer: phase I trial.* Radiology, 2013. **267**(3): p. 932-40.
266. Paulides, M.M., et al., *Feasibility of MRI-guided Hyperthermia Treatment of Head and Neck Cancer.* 2014 8th European Conference on Antennas and Propagation (Eucap), 2014: p. 1474-1477.
267. Marshall, D.F., *Visualization of Real Time MR Guided Hyperthermia.* 16th Nordic-Baltic Conference on Biomedical Engineering, 2015. **48**: p. 88-91.
268. Witney, T.H. and K.M. Brindle, *Imaging tumour cell metabolism using hyperpolarized 13C magnetic resonance spectroscopy.* Biochem Soc Trans, 2010. **38**(5): p. 1220-4.
269. Serrao, E.M. and K.M. Brindle, *Potential Clinical Roles for Metabolic Imaging with Hyperpolarized [1-(13)C]Pyruvate.* Front Oncol, 2016. **6**: p. 59.
270. von Morze, C., et al., *Investigating tumor perfusion and metabolism using multiple hyperpolarized (13)C compounds: HP001, pyruvate and urea.* Magn Reson Imaging, 2012. **30**(3): p. 305-11.
271. Lau, A.Z., et al., *Simultaneous assessment of cardiac metabolism and perfusion using copolarized [1-(13) C]pyruvate and (13) C-urea.* Magn Reson Med, 2017. **77**(1): p. 151-158.
272. Song, C.W., et al., *Tumour oxygenation is increased by hyperthermia at mild temperatures. 1996.* Int J Hyperthermia, 2009. **25**(2): p. 91-5.
273. Corr, S.J., et al., *A New Imaging Platform for Visualizing Biological Effects of Non-Invasive Radiofrequency Electric-Field Cancer Hyperthermia.* PLoS One, 2015. **10**(8): p. e0136382.
274. Winslow, T.B., et al., *A pilot study of the effects of mild systemic heating on human head and neck tumour xenografts: Analysis of tumour perfusion, interstitial fluid pressure, hypoxia and efficacy of radiation therapy.* Int J Hyperthermia, 2015. **31**(6): p. 693-701.
275. King, R.L., et al., *Development and characterization of a tissue-mimicking material for high-intensity focused ultrasound.* IEEE Trans Ultrason Ferroelectr Freq Control, 2011. **58**(7): p. 1397-405.
276. Eddy, H.A., *Alterations in tumor microvasculature during hyperthermia.* Radiology, 1980. **137**(2): p. 515-21.
277. Poorman, M.E., et al., *Open-source, small-animal magnetic resonance-guided focused ultrasound system.* J Ther Ultrasound, 2016. **4**(1): p. 22.
278. Lefor, A.T., S. Makohon, and N.B. Ackerman, *The effects of hyperthermia on vascular permeability in experimental liver metastasis.* J Surg Oncol, 1985. **28**(4): p. 297-300.

279. Gaber, M.H., et al., *Thermosensitive liposomes: extravasation and release of contents in tumor microvascular networks.* Int J Radiat Oncol Biol Phys, 1996. **36**(5): p. 1177-87.
280. Lai, C.Y., B.Z. Fite, and K.W. Ferrara, *Ultrasonic enhancement of drug penetration in solid tumors.* Front Oncol, 2013. **3**: p. 204.

Publishing Agreement

It is the policy of the University to encourage the distribution of all theses, dissertations, and manuscripts. Copies of all UCSF theses, dissertations, and manuscripts will be routed to the library via the Graduate Division. The library will make all theses, dissertations, and manuscripts accessible to the public and will preserve these to the best of their abilities, in perpetuity.

Please sign the following statement:

I hereby grant permission to the Graduate Division of the University of California, San Francisco to release copies of my thesis, dissertation, or manuscript to the Campus Library to provide access and preservation, in whole or in part, in perpetuity.

Author Signature Jessie Eileen Lee Date March 28, 2018